Z-Pinning to Improve Strength of 3D Printed Liquid Crystal Polymer Parts

Master Thesis

Lorenzo Onorato

Delft University of Technology

TU Delft

This page has been intentionally left blank.

Z-Pinning to Improve Strength of 3D Printed Liquid Crystal Polymer Parts

Master of Science Thesis

by

Lorenzo Onorato

in partial fulfilment of the requirements for the degree of

Master of Science
in Aerospace Engineering

at the Delft University of Technology

To be defended on 16/06/2025 at 14:00

Student number:	4816455	
Date:	June 16, 2025	
Assessment committee:	Dr. K. (Kunal) Masania	Delft University of Technology
	Dr.ir. J.A. (John-Alan) Pascoe	Delft University of Technology
	Dr. B. (Baris) Caglar	Delft University of Technology
Daily supervisor:	Dr. S. (Sourav) Patranabish	Delft University of Technology

This thesis is confidential and cannot be made public until 16 June 2026.

Preface

This thesis marks the conclusion of my academic journey at TU Delft, which began in 2019 as a BSc student. There, I discovered my passion for aerospace materials and design, a passion I continued to cultivate throughout my MSc, shaping both my academic and professional identity. As the Delft chapter of my life comes to a close with this graduation, I acknowledge that the most valuable and enriching part of this time has been the people I had the chance to share it with.

I wish to first thank Dr. Kunal Masania for creating the technical and human environment that made this work possible, and for providing the resources to carry it out. It was through Kunal that I came into contact with NematX, and thanks to his support, I embarked on an internship experience that proved pivotal in my development.

My sincere thanks go to the entire NematX team for nurturing my 3D printing engineer soul from the ground up. I owe them the solid technical foundations that enabled me to pursue this thesis, from formulating a research proposal to recognizing the potential of an idea and following it through with perseverance. The decision to explore LCP 3D printing with this project was directly inspired by my time in Förrlibuckstrasse. I am especially grateful to Silvan Gantenbein, whose technical insight, pragmatic mindset, and mentorship were instrumental throughout this project. Every moment of every meeting with Silvan contributed critically to the thesis. Beyond guidance, he taught me how to approach research in a way that complements the academic rigor of TU Delft with an iterative, experiment-driven mindset. I deeply valued the mutual understanding we shared, so much so that even complex ideas often needed no words, as he could catch my thoughts from the glint in my eyes. I also wish to thank Lorenzo Cascone for his tireless patience in answering my many (according to him) questions, and Chiara Mascolo for her always generous and timely support.

To Dr. Sourav Patranaship, my daily supervisor, thank you for your distinctively optimistic and supportive approach. I greatly appreciated your flexibility, constructive feedback, and tolerance of the quirks of my night owl lifestyle. Your guidance in scientific writing was essential to the quality of this thesis. To the entire Shaping Matter Lab, thank you for the feedback, cakes, smiles, and that slow road trip to Frankfurt. Special thanks to Mark for the time and care he invested in both my technical progress and emotional balance. I also thank Harold, Wouter, Silvan, Stefan, David, Matas, and Aster for filling the lab with energy. Extra gratitude to Caroline for opening to me the door to 3D-printed LCPs and for the inspiration her work provided.

I extend my deepest appreciation to TU Delft and the Faculty of Aerospace Engineering for cultivating an environment where learning and experimentation truly thrive. Here, I have grown into an engineer, an adult, and a citizen, and I will carry the Delft Engineer mindset proudly into my next adventures. I am grateful for the high level of education, the international outlook, and the opportunity to work hands-on with cutting-edge infrastructure and bright minds. My thanks go to all lecturers and staff, from those who addressed packed lecture halls six years ago to those who will now sit on my thesis committee.

Finally, to my family and friends, thank you. Words fall short of conveying your importance on this journey, but I'll try. My parents and sister have been the compass of my ambitions, and my brother, Giuseppe, has been the example I was lucky enough to follow up to this point. If my family has been the yin of support, my friends have been the yang of joy. To Pizza, the Cucarachas, the Study Group, Mikel, Georgi, Levin, and Sergio, thank you for giving meaning to the day-to-day grind. You made this thesis, and this entire journey, infinitely better.

Lorenzo Onorato
Delft, 03/06/2025

Abstract

Fused filament fabrication (FFF) of thermotropic liquid crystal polymers (LCPs) presents an attractive route toward lightweight components with excellent in-plane mechanical properties, enabled by molecular alignment during extrusion. However, the layer-by-layer nature of FFF leads to weak interlayer adhesion, which severely compromises mechanical performance in the build direction (Z-axis). This anisotropy limits the structural reliability of printed LCP parts under demanding conditions. Inspired by through-thickness reinforcement methods used in laminated fiber-reinforced composites, this thesis investigates the potential of z-pinning to enhance interlayer strength and damage tolerance in FFF-printed LCPs.

This work focuses on adapting the z-pinning concept, previously applied in PLA systems, to the challenges of anisotropic, shear-aligning LCPs. A z-pinning methodology is developed around the commercial filament Vectra® A950, utilizing a bottom-up insertion process enabled by custom G-code routines. Vertical pins are extruded into pre-formed voids during the print, allowing control over pin shape, height, and placement. The approach leverages standard FFF hardware, requiring only a narrow-tip nozzle and careful synchronization of extrusion timing to ensure consistent pin deposition.

Mechanical testing was conducted on both pinned and unpinned tensile specimens printed in the Z-direction. The results demonstrate that z-pinning significantly enhances performance when properly implemented. The best configuration, tall pins arranged in an ABA staggering pattern, achieved a 40% increase in peak load and a tenfold increase in energy absorption before reaching peak load. Fracture analysis revealed more distributed fracture patterns, with signs of crack deflection and arrest, indicating a transition from brittle delamination to more progressive failure modes.

These findings validate the feasibility of z-pinning for improving the mechanical properties of 3D-printed LCP components. However, the benefits are highly sensitive to process execution, as poor pin deposition may negate reinforcement or introduce stress concentrators. The study underscores the importance of concurrent design and manufacturing development, showing that even in single-material systems, structural performance can be engineered through localized deposition strategies. This opens a path toward more robust, anisotropy-mitigated 3D-printed parts using high-performance polymers.

Keywords Z-pinning, liquid crystal polymer (LCP), fused filament fabrication (FFF), interlayer strength, toughening mechanism

This page has been intentionally left blank.

Table of Contents

This page has been intentionally left blank.

List of Figures

List of Tables

This page has been intentionally left blank.

Nomenclature

Acronyms and Abbreviations

3D	Three Dimensional
ABS	Acrylonitrile Butadiene Styrene
AM	Additive Manufacturing
ASTM	American Society for Testing and Materials
CAD	Computer-Aided Design
CF	Carbon Fiber
CFRP	Carbon Fiber Reinforced Polymer
DNA	Deoxyribonucleic Acid
FFF	Fused Filament Deposition
FRP	Fiber Reinforced Polymer
G-code	Geometric Code
HBA	4-Hydroxybenzoic Acid
HNA	2-Hydroxy-6-naphthoic Acid
IQR	Inter Qurtile Range
ISO	International Organization for Standardization
LCP	Liquid Crystal Polymer
PEEK	Polyetheretherketone
PEI	Polyetherimide
PETG	Polyethylene Terephthalate Glycol
PLA	Poly-lactic Acid
SML	Shaping Matter Lab
STD	Standard Deviation

Greek Symbols

ΔL	Change in clamp span
λ_{A}	Thickness of skin aligned towards the air
λ_{H}	Thickness of skin aligned towards the substrate

Latin Symbols

A_{n}	Nominal cross-sectional area
d_{n}	Nozzle diameter
F_{crack}	Load at which a crack nucleates
F_{max}	Maximum load
F_{recovery}	First peak in load after F_{max}
h	Layer height
h_{cone}	Height of pin cone section
h_{cylinder}	Height of pin cylindrical section
h_{pin}	Total pin height
L_{n}	Nominal length / clamp span
T_{RT}	Ambient or room temperature
T_{B}	Temperature of the heated bed
T_{n}	Nozzle temperature
v_{e}	Velocity of filament extrusion
V_{p}	Nozzle velocity on bed
W	Work applied onto a test specimen
w	Line width

1

Introduction

This chapter starts by outlining the motivations behind exploring fused filament fabrication using liquid crystal polymers. It then delves into the core aim of this study, which is to develop and evaluate a z-pinning concept. Finally, it highlights the research objectives and summarizes the thesis's structure.

1.1. 3D printed liquid crystal polymers

Fused filament fabrication (FFF) is a form of extrusion-based additive manufacturing known for its geometric versatility and ease of use. It is commonly employed to produce polymer parts with customized shapes, ranging from household tools to functional prototypes. However, most thermoplastics used in FFF such as Polylactic Acid (PLA), Acrylonitrile Butadiene Styrene (ABS), or Polyethylene Terephthalate Glycol (PETG) provide limited mechanical strength, constraining their use in performance-driven applications [1, 2].

In recent years, thermotropic liquid crystal polymers (LCPs) have emerged as promising candidates for producing stronger printed parts. LCPs exhibit a mesophase in the molten state, characterized by the alignment of molecular chains into nematic domains. When subjected to shear and elongational flow during extrusion, these domains orient along the flow direction and retain part of this alignment after cooling. This results in highly anisotropic extrusions with high stiffness and strength along the print path [3, 4]. Among thermotropic LCPs, the copolymer HBA:HNA (4-Hydroxybenzoic Acid: 2-Hydroxy-6-naphthoic Acid), commercialized as Vectra®A950, has shown particular potential due to its printability, high modulus, and low moisture uptake [5, 6]. A key feature of this material is its inherent anisotropy arising from molecular alignment during extrusion. This directional dependence of properties parallels that seen in traditional fiber-reinforced composites (FRPs), where strength and stiffness are also highly anisotropic due to fiber orientation. In both cases, this anisotropy introduces complexity in design and manufacturing but, if properly harnessed, enables exceptional mechanical performance. However, unlike FRPs, composed of discrete fibers embedded in a separate matrix, 3D-printed LCPs achieve this behavior using a single, self-aligning feedstock. This distinction simplifies recycling and processing, offering a monolithic alternative to conventional multi-phase composites. Today, LCP as a material is already found in demanding applications, including electronics and woven aerospace fabrics [4].

1.2. Z-pinning: 3D printing on 2.5D printers

Despite the potential of LCPs to deliver high in-plane properties through extrusion alignment, their layer-by-layer deposition in FFF inherently produces anisotropic structures. The strength and stiffness along the filament direction are significantly higher than across the layers, where weak adhesion and the presence of voids often lead to premature failure [1, 7]. The rapid cooling that locks molecular orientation also restricts interlayer diffusion, compromising z-direction integrity [8, 9]. This behavior parallels conventional composite laminates, where weak interlaminar strength is often tackled using through-thickness reinforcement strategies such as z-pinning [10]. In traditional composites, z-pins are inserted through the laminate to bridge plies and arrest crack propagation across layers. Inspired by this approach, researchers have proposed adapting z-pinning to extrusion-based additive manufacturing (AM). By depositing vertical pins during the print process, it becomes possible to introduce structural elements that bridge layers and improve mechanical cohesion in the z-direction [11, 12].

Initial demonstrations of this technique using PLA and carbon fiber-filled PLA (CF-PLA) have shown promising results, with significant increases in z-strength and altered fracture behavior [13, 14]. However, the use of z-pinning in shear-aligning LCPs remains largely unexplored. The anisotropic nature of LCPs, while beneficial in-plane, may interfere with pin performance and interfacial strength in complex ways [15].

1.3. Research definition

This research investigates the application of z-pinning to improve the mechanical performance in the z-direction of 3D-printed LCP components. While the benefits of LCP alignment during printing are well established, the potential of vertical pinning to improve interlayer properties in such systems has not been assessed with confidence. Early applications of z-pinning in fiber-filled PLA demonstrated clear mechanical improvements; however, the extension to shear-aligning polymers, such as LCPs, raises new questions regarding interface design, pin geometry, and failure mechanisms.

The central research question addressed in this work is:

Can the strength in the z-direction of 3D printed LCP parts be improved through z-pinning?

To answer this, the thesis sets out the following objectives:

- To develop a z-pinning concept for 3D printed LCP parts designed to improve their tensile strength in the direction perpendicular to the deposition plane;
- To manufacture and test pinned and reference LCP specimens to assess tensile properties in the z-direction;

The research is initiated by a literature review, as outlined in Chapter 2. The following work is organized into two main phases. The first focuses on developing the pinning method, including designing pin geometries and integrating pin deposition into the FFF workflow. Chapter 3 is dedicated to establishing the pinning concept and outlines the changes implemented to the previous printing hardware. Chapter 4 elaborates on the details of the pinning design and the manufacturing considerations. The second phase, detailed in Chapter 5, addresses the experimental characterization of printed samples, analyzing mechanical performance and benchmarking against unpinned controls. Chapter 6 concludes the thesis by reflecting on the key findings, evaluating the feasibility and limitations of the proposed approach, and offering recommendations for future research directions.

The trinity of structural design, which unites material, geometry, and manufacturing, serves as a guiding principle throughout this study. The interaction between these three aspects is especially critical in extrusion-based processes, where geometric decisions and print parameters must be tuned to exploit the anisotropic material response of LCPs. By navigating these interdependencies, this thesis aims to formulate practical design rules for mechanically robust, pinned LCP structures.

2

Background

This chapter provides the relevant notions researched to establish the foundations for this study, focusing on materials, processes, and design considerations. To contextualize the development of the pinning concept and its integration within FFF, the chapter progresses from general principles to specific phenomena associated with the studied material and process. The chapter begins in Section 2.1 by situating FFF within the broader AM landscape. The operating principles of FFF are introduced alongside a discussion of its strengths, limitations, and evolving role in structural applications. Section Section 2.2 introduces thermotropic LCPs, focusing on differences that processing methods impart to the mechanical properties. Section Section 2.3 then explores the implications of manufacturing LCP parts via FFF. This process enables the exploitation of flow alignment to develop high mechanical properties. However, the same mechanism that enhances in-plane properties limits interlayer bonding, leading to a highly anisotropic performance envelope. Finally, section Section 2.4 reviews prior efforts to overcome mechanical anisotropy in FFF through z-pinning.

2.1. Fused Filament Fabrication

AM is a production method that involves laying material where desired in a layer-by-layer fashion, unlike traditional subtractive processes, such as machining, which remove material to achieve the desired shape. This layer-wise construction enables the fabrication of complex geometries, reduces material waste, and allows for rapid prototyping and customization. However, commercial success has varied across sectors. While AM has become a staple in consumer products, medical implants, and tooling, its penetration into high-performance structural applications, such as aerospace primary structures, remains limited due to low mechanical properties, poor repeatability, and part certification constraints. AM refers to various technologies developed to manufacture materials from metals to ceramics and polymers. Fused filament fabrication (FFF, often synonymous with FDM®) is an AM technique that concerns the extrusion of thermoplastic filament. [1, 16–21].

In FFF, a solid thermoplastic filament is fed into a heated liquefier and extruded through a nozzle, depositing material onto a substrate in successive layers. Commonly used polymers include PLA, ABS, PETG, and high-performance materials such as Polyether ether ketone (PEEK) and Polyetherimide (PEI), each requiring distinct temperature profiles and print environments. The process relies on the semi-liquid state of the polymer to facilitate the adhesion between layers. Continuous strands are placed within a layer, yet there are intermittent contact locations between layers along the build direction. [11] Factors such as layer infill pattern, layer thickness, nozzle temperature, and infill strategy play crucial roles in tuning mechanical performance [2, 16, 22]. Figure 2.1 illustrates the main aspects of the layer deposition during FFF. Figure 2.1a shows the main hardware components, while Figure 2.1b illustrates the difference in layer interface width between parts printed with different layer heights. The print line's geometry and contact dynamics with the underlying layer are key to achieving mechanical continuity across layers. Cooling rates, layer printing time, nozzle temperature, and bed temperature must be finely tuned to avoid defects such as voids, warping, and delamination [1, 23].

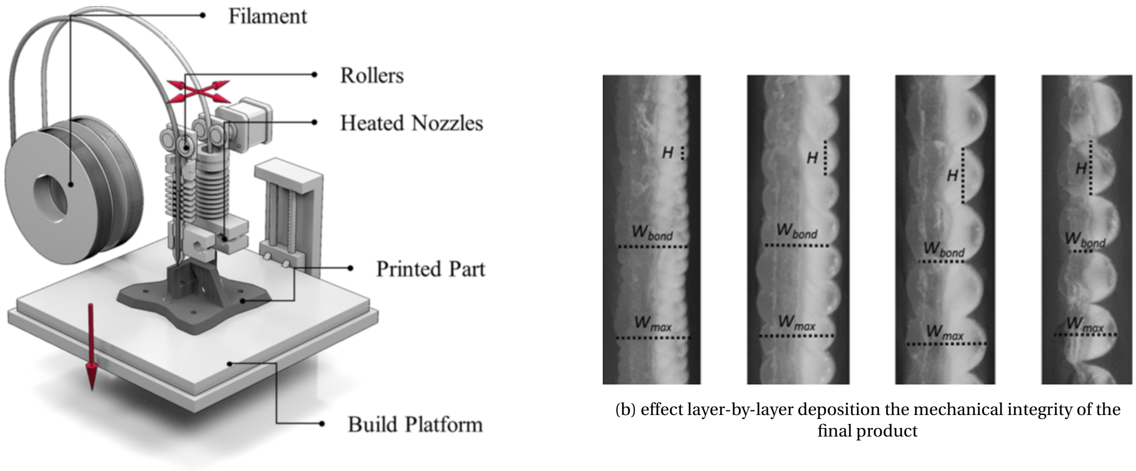

(b) effect layer-by-layer deposition the mechanical integrity of the final product

(a) Diagram of the FFF process

Figure 2.1: Key elements of the Fused Filament Fabrication (FFF) process. (a) Displays the fundamental hardware components of an FFF printer [1], while (b) depicts cross-sections of printed parts with varying layer height parameters, highlighting the interphase differences between successive layers [8].

2.2. Thermotropic Liquid Crystal Polymers

LCPs are a category of macromolecules that combine characteristics of both crystalline solids and viscous liquids. Their defining feature is the ability to form a liquid crystalline phase, or mesophase, in which polymer chains exhibit orientational order while retaining the capacity to flow. The first study of liquid crystallinity dates back to the late 19th century. Since then, a wide range of structures, from small organic molecules and surfactants to biological entities like DNA, have been found to exhibit similar behavior. LCPs are a distinct subset of liquid crystalline materials, distinguished by their high molecular weight compared to the smaller molecules used in display technology [4].

LCPs are further classified into lyotropic LCPs, which exhibit mesophases in solution, and thermotropic LCPs, which develop liquid crystallinity upon heating. Early LCPs depended on lyotropic conditions and needed an acidic environment for processing. Aramid fibers, such as Kevlar, are an example of engineering materials in this category. To address the drawback of using solvents in fiber spinning, thermotropic LCPs were introduced. Over the years, improved molecular formulations have raised the attainable service temperature. As a result of these efforts, the LCP investigated in this study was developed and patented in 1979. It is called HBA:HNA when referring to its copolymer nature, combining hydroxy-naphthoic acid (HNA) and hydroxy-benzoic acid (HBA) in the 73:27 ratio, and it is commercialised with the name Vectra® A950. In the molten state, HBA:HNA exhibits nematic order, meaning that the chains align preferentially along a common axis called the nematic director. During processing, this alignment can be induced by shear and elongational flow. The alignment of the oriented domains derived from the extrusion is partially preserved during solidification and is responsible for the pronounced anisotropy observed in the fabricated parts [4].

Thermotropic liquid crystal polymers, including HBA:HNA copolymers, have been adopted across various structural and functional applications due to their high stiffness, low moisture uptake, and thermal stability. Traditional processing routes consist of injection molding and fiber spinning. Injection molding yields good dimensional stability and strength, albeit with limited control over local orientation and anisotropy. Melt spinning is used to manufacture high-performance fibers such as Vectran®. These fibers exhibit excellent fatigue resistance and are commonly used in ropes, sailcloth, protective layers, and inflatable space structures. For applications requiring barrier properties, thin films can be produced by stacking extruded sheets and heat-pressing them just below the melting point to enable solid-state polycondensation. Extrusion processing, such as FFF, allows for direct control over molecular orientation and local anisotropy within a part by exploiting flow-induced alignment during printing. The mechanical properties of HBA:HNA vary significantly depending on the processing method and parameters. Spun fibers exhibit tensile moduli exceeding 100 GPa, whereas injection-molded parts typically reach 15–20 GPa. FFF-printed parts show a wide modulus range between 3 and 30 GPa, primarily dictated by the degree of alignment achieved during deposition. The diverse applications emerging from the different manufacturing processes of LCPs are illustrated in Figure 2.2. Figure 2.2a demonstrates how various manufacturing approaches lead to distinct mechanical characteristics. Figure 2.2b illustrates an electrical connector, a typical use of injection-molded LCP in the electronics sector, mainly due to its chemical resilience and minimal moisture absorption. Figure 2.2c shows the Mars Pathfinder mission's landing airbags, crafted from fabric woven with LCP fiber for its stiffness and impact resistance. Adjusting the anisotropy of LCPs through processing parameters establishes the connection between manufacturing and application. [4]

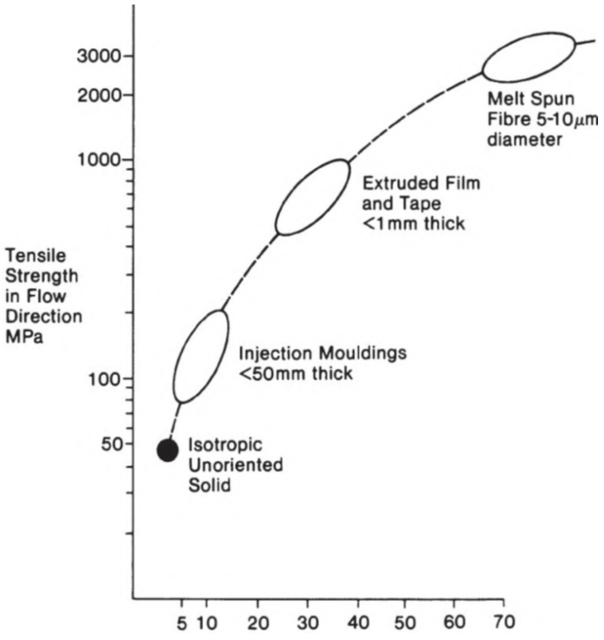

(a) Tensile strength versus stiffness of LCP components manufactured with different processes

(b) Injection molded LCP

(c) Melt spun LCP

Figure 2.2: Change in mechanical properties and application of thermotropic LCPs resulting from different manufacturing processes. (a) Illustrates the variation in strength and stiffness of LCP components depending on the manufacturing methods adopted [5]. Subfigures (b) and (c) provide examples of applications: injection molded LCP for electrical connectors and melt spun LCP for Mars landing airbags utilized by NASA. [1]

2.3. Liquid Crystal Polymers in Fused Filament Fabrication

Vectra® A950 can be extruded into a filament and used to manufacture parts using FFF. 3D printing of LCPs is still in its infancy compared to injection molding and fiber spinning, and it has yet to achieve commercial viability. The nature of 3D printing can potentially deliver high mechanical properties, characteristic of spun LCP, to small 3D components, which are the domain of injection molding. The mechanism that allows thin extrusions to develop high mechanical properties relies on the liquid crystalline nature of the polymer. Figure 2.3 demonstrates the molecular alignment occurring during the extrusion process of Vectra® A950 through a 3D printing nozzle. The mesophase in the polymer melt at rest consists of randomly oriented nematic domains. Within each domain, the polymer chains primarily orient themselves along one particular direction to minimize the elastic free energy. Nevertheless, the random orientation of these directions results in the material having isotropic bulk properties. During extrusion, the molten polymer undergoes shear and extensional flow, aligning the nematic directors along the extrusion direction. When the material leaves the nozzle, the shear forces stop, and the domains begin rearranging randomly. Having left the nozzle, the material begins to cool from the outside. The outer layers cool down rapidly, locking the alignment of the nematic directors in place, while the inner material has time to reorder. This cooling mechanism produces a core–shell filament structure, with a highly aligned outer skin and a less ordered core. The extent of the molecular alignment locked by the rapid cooling of the material determines the degree of anisotropy of an extrusion line [24].

---

[1] Subfigure (b) is taken from `https://www.asaclean.com/blog/designing-parts-with-liquid-crystal-polymer` while subfigure (c) is taken from `https://www.space.com/33483-mars-landing-technology-viking-curiosity-rover.html`.

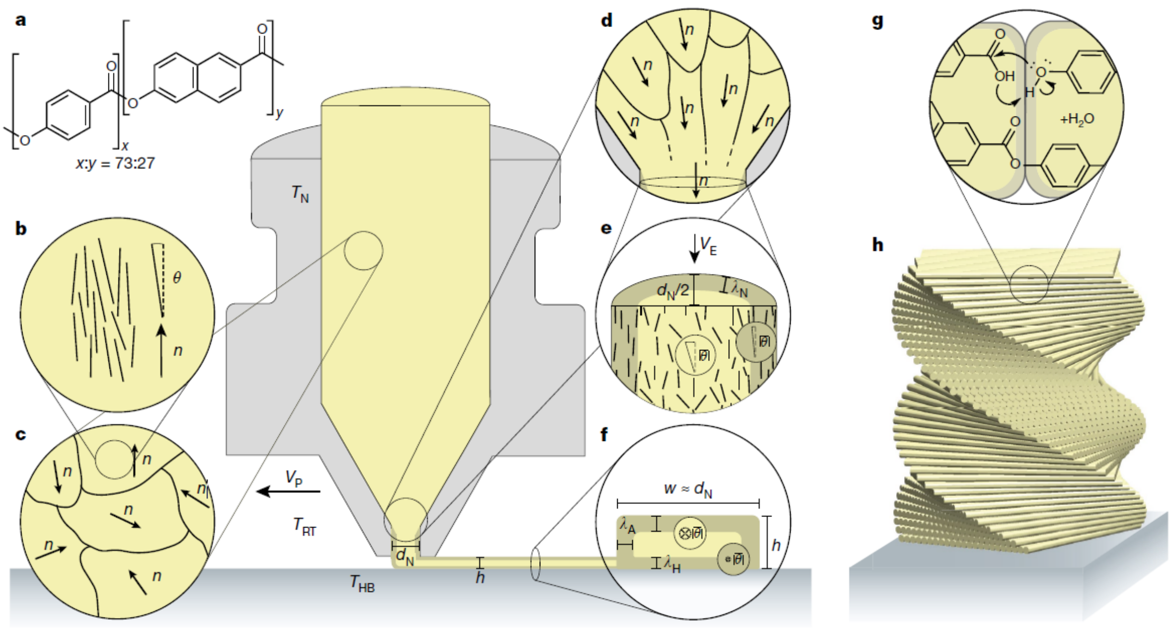

Figure 2.3: Fused Filament Fabrication of hierarchical, thermotropic LCPs. Subfigure a shows the molecular structure of the random LCP HBA:HNA commercialized as Vectra® A950. Subfigure b shows the polymer chains in the nematic state, generally arranged along a director n. Subfigure c shows how locally aligned molecules form randomly oriented domains in the static melt. Subfigure d shows how the orientation of the domains aligns with the extrusion direction due to shear forces in the nozzle. In subfigures e and f, the extruded material solidifies from the outside. The domains in the outer section maintain the alignment, while those on the inside regain their random orientation before cooling down, resulting in a core-shell structure. Subfigure g illustrates how annealing induces crosslinking, which enhances the transfer of loads across print lines. Subfigure h depicts the formation of a 3D part through the deposition of multiple layers. T_N, nozzle temperature; d_N, nozzle diameter. "T_B, temperature of the heated bed or substrate; T_{RT}, temperature of the environment (room temperature); V_E, velocity of extrusion; V_P printing velocity; w, print width; λ_A, thickness of skin aligned towards air; λ_H, thickness of skin aligned towards the heated bed or substrate" [3].

High degrees of molecular alignment in the print line result in high strength and stiffness in the extrusion direction. The manufacturing conditions determine the extent of the molecular alignment by impacting the proportion between skin and core. All the printing parameters that affect cooling impact the proportion between skin and core and can therefore be used to influence the mechanical properties. Such parameters include nozzle temperature, nozzle diameter, layer height, and linewidth. Figure 2.4 shows how modifying the linewidth of print lines results in a change in strength, stiffness, and failure mechanism. Narrower print lines are stronger, stiffer, and fail in a brittle manner, while wider ones are more flexible, weaker, and fail in a ductile manner. Adjusting these printing parameters during the printing process enables fine-tuning the material's mechanical behavior within a print line, between print lines, and throughout layers [6].

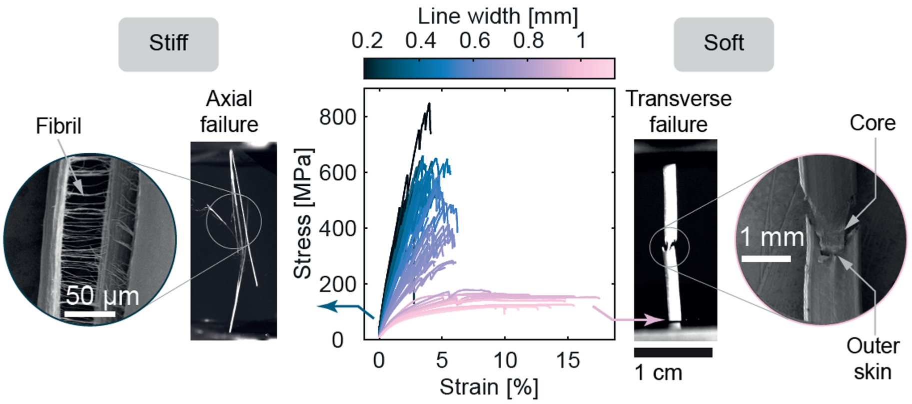

Figure 2.4: Change in line width affects the mechanical behavior of LCP print lines. Print lines characterized by a narrow linewidth exhibit steeper stress-strain curves, culminating in brittle failure at elevated stress levels. Conversely, print lines with a wider line width display a reduced peak stress and demonstrate ductile failure, which is attributed to the presence of a ductile core [4].

The mechanical performance of printed LCP parts results from their highly anisotropic nature, which arises from flow-induced molecular alignment during extrusion. This anisotropy manifests within individual filaments (in-line), within layers (in-plane), and across the part (out-of-plane), leading to properties that strongly depend on the orientation of the applied load. As described by classical laminate theory, stiffness and strength are maximized when the loading direction aligns with the print path and decline sharply as the angle increases. While this directional reinforcement is advantageous for in-plane properties, it inherently compromises interlayer bonding [25]. The same rapid solidification that preserves molecular orientation also limits chain diffusion across layers, resulting in poor adhesion in the build direction. Consequently, printing parameters such as layer height, nozzle temperature, and print speed are crucial in achieving a balance between alignment and interfacial strength. The high anisotropy has demonstrated significant potential when using customized path planning: stress-aligned toolpaths developed in [26–28] yielded strength improvements exceeding 150% compared to traditional layer-by-layer deposition patterns. Furthermore, [4, 9] demonstrated that deposition path strategies can enhance interlayer load transfer without requiring thermal annealing, which would undermine recyclability, and without forfeiting directional alignment. Analogous to conventional FRPs, the deliberate deposition of material creates the opportunity to tailor the material properties across the three dimensions.

2.4. State of the art of z-pinning in FFF

The concept of z-pinning has been applied to fused-filament-fabricated parts, taking inspiration from traditional fiber-reinforced polymer manufacturing [12]. Just like in fiber-reinforced polymer manufacturing, the purpose of z-pinning in FFF is to mitigate the mechanical anisotropy that results from the layering of the material. While traditional FFF is constrained to the sequential deposition of material in the horizontal plane, z-pinning enables material deposition along the Z axis, effectively adding a new printing direction. The further deposition axis is achieved by introducing continuous vertical extrusions that bridge multiple horizontal layers. Since the pinning takes place within the same manufacturing workflow, the process does not require post-processing, additional hardware, or different materials [10]. This section discusses the pinning strategies documented in the literature. It begins with a broad overview of the concept, then highlights the findings from research on z-pinning of PLA components relevant for this study in Subsection 2.4.1, and concludes with prior efforts to implement pinning in the FFF of LCP filament as detailed in Subsection 2.4.2.

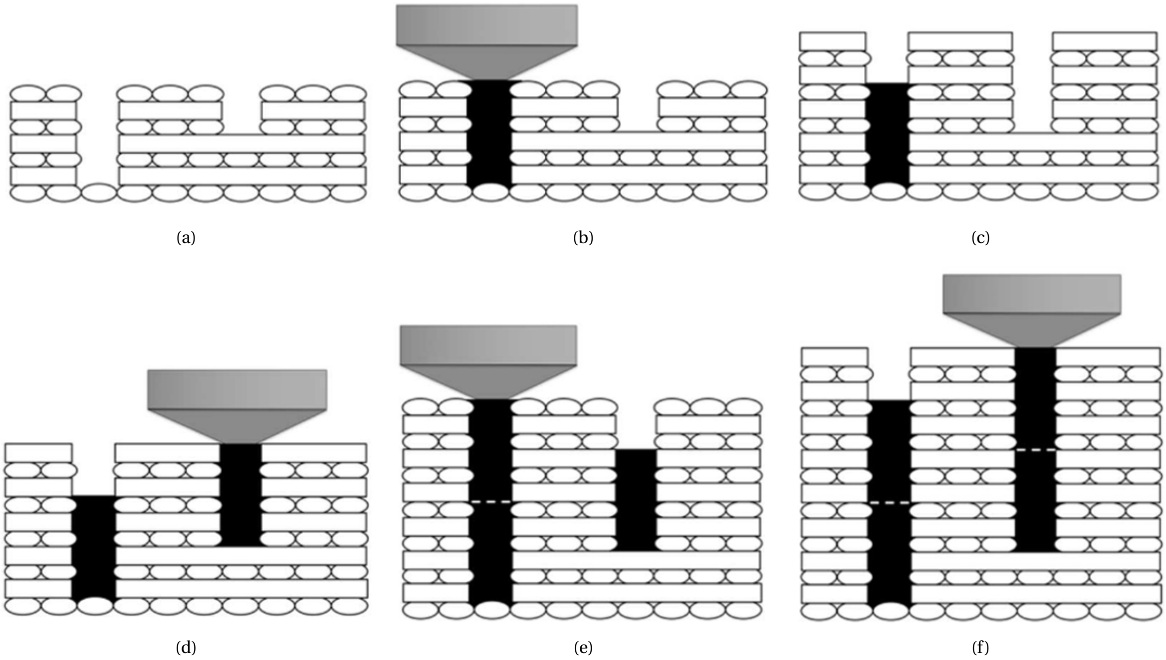

Figure 2.5: Illustration of the different stages of z-pinning in FFF. (a) The print path is modified so that conventional layer-by-layer deposition leaves intentional vertical cavities; (b) once a cavity reaches the predetermined depth, the nozzle deposits material in a single extrusion to form a pin; (c) printing resumes, leaving new cavities above the filled ones; (d) pinning is staggered across different columns to prevent aligned weak points; (e) seam lines remain at the interface between successive pin segments due to discrete extrusion; (f) this alternating sequence of conventional printing and pinning continues until the part is completed [12].

The foundation of z-pinning consists of intentionally leaving unfilled cavities during printing. Filling these cavities with a single extrusion allows them to extend through successive layers [10, 29]. The step-by-step process is illustrated in Figure 2.5. The printing begins with traditional layer-by-layer extrusion, leaving cavities aligned in the vertical direction (Figure 2.5a). Once these cavities reach a predefined depth, the standard layer-by-layer deposition is momentarily paused. The print head moves over the voids and extrudes material, forming a continuous pin that reinforces the structure in the vertical direction (Figure 2.5b and Figure 2.5c). These voids span the entire height designated for reinforcement, ensuring that the pins interlock multiple layers. However, since the extruded filament can only retroactively fill a finite depth, the interface between consecutive pin segments interrupts the load path Figure 2.5d. To mitigate this discontinuity and maintain effective bridging, the pinning layers must be staggered across different pin columns, ensuring that no single layer becomes a weak point in the structure (Figure 2.5e and Figure 2.5f).

2.4.1. Development of z-pinning with 3D printed PLA

The development of z-pinning processes tailored to FFF has been primarily explored using PLA filament so far. Existing research has been carried out by a single collaborative group affiliated with a national laboratory and academic institutions [10–14, 29–31], which have also filed related patents [32, 33]. As the body of literature originates from one research team, the scope of the studies remains narrow, and the diversity of experimental data is limited. Providing a clear overview of the practical implementation of the z-pinning process is therefore crucial to properly contextualize the findings.

Hardware setup and materials

The printing setup used in the latest studies aligns with the standard FFF hardware configurations. Z-pin research has been conducted consistently using an off-the-shelf tabletop FFF printer (MakerGear M2). The hardware parameter that changed over time is the diameter of the nozzle, which has decreased over the years, ultimately settling at 0.4 mm, the most widely used size in FFF. As a result, the latest studies align with standard FFF hardware configurations. The materials used include PLA and CF-PLA filaments. Tensile test samples were initially printed as individual parts; however, the problems encountered led to the adoption of a different approach. The solution consisted of printing a large part and cutting it into the shape of the dogbone specimen. The G-code for printing is manually modified to implement the path-planning adjustments required for pinning. The key advantage of the general implementation is that it does not require modifications to existing FFF hardware, since pin extrusion is achieved only by slicing and deposition strategies [11, 30].

G-code implementation of pin parameters

The pinning G-code was obtained by slicing the part with a rectilinear infill pattern featuring alternating 0/90-degree layer lines and a low infill density (30-55%). This infill structure yields a porous inner volume comprising vertical voids with a square cross-section. These voids are filled with material using custom G-code, resulting in the creation of Z-pins. The infill-pin structure resulting is shown in Figure 2.6 where the orange print lines are part of the infill scaffolding, while the two black homogeneous areas are pin sections eight layers deep. Throughout this thesis, the term "layer infill" refers to the material deposited regularly within each layer, as opposed to the pins, which are considered a form of "cross-layer infill" since they span multiple layers in the Z-direction. According to the literature approach, the dimensions of the voids are controlled by tuning the infill parameters. The pin extrusion is arranged in a checkerboard pattern, with empty vertical sections separating the pins. This checkerboard pattern is also used to create the pin staggering pattern. The volume of the pin and the depth of the hole are regulated by the pin extrusion schedule [30]. Together with the geometrical aspects, the material choice has a significant impact on the efficacy of pinning."

Material-related success of z-pinning

Z-pinning was more effective in naturally anisotropic materials. In the case of CF-PLA, the short fibers align with the direction of extrusion during printing. The use of z-pinning with this material resulted in a three-fold increase in strength [11], while unreinforced PLA saw only an improvement of 20% [10]. With both materials, the pinned samples exhibited a more intricate fracture path, suggesting crack deflection across multiple layers. However, not all instances of pinning resulted in stronger parts than conventionally printed ones when the mechanical properties were normalized by weight [12]. It is necessary to tune the geometrical and extrusion parameters that define a pin to improve the weight-specific mechanical performance.

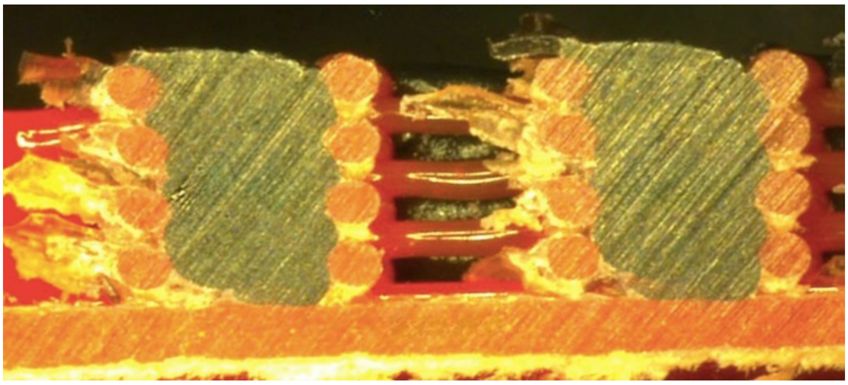

Figure 2.6: Section view of FFF PLA part with sparse infill and z-pins spanning eight layers. The pins were extruded with CF-PLA (hence the dark colour) while the infill structure was printed with orange PLA (lighter colour). Adapted from [10]. [2]

Extrusion volume and cavity filling

Improper extrusion volume settings can result in underfilling or overextrusion. The theoretical pin volume, determined geometrically based on the available hole dimensions, does not match the volume that can be deposited. The walls of the cavity exhibit wavy contours as a result of the layered nature of extrusion-based printing, and due to its viscous flow behavior, the molten material does not fully conform to the void during pin extrusion [30]. Therefore, the actual fill volume is always lower than the geometrically obtained limit. In general, the adhesion between the hot pin and the surrounding layer infill is not directly controlled; filling imperfections are inevitable, and thus remelting is unlikely. The strengthening of parts is therefore related to a different mechanism than molecular interactions [10].

Mechanical interlocking as primary strengthening mechanism

The main strengthening mechanism is the mechanical interlocking between the pins and the infill scaffolding. When the extrusion volume of the pin increases in the same pin void, the material expands beyond the vertical square section, infiltrating the gaps between the layer infill. This interlocking effect occurs independently of molecular bonding. Figure 2.7 shows a series of pin cross sections that were extruded with increasing volume. It is possible to see how cavities are present in both Figure 2.7a and Figure 2.7b that were obtained by extruding respectively 80% and 100% of the geometrical void volume. In Figure 2.7c instead, the pin extrusion flowed past the scaffolding. Tensile testing and FEM simulations consistently showed a significant increase in the strength of parts as the volume of the extruded pin increases and the section of the pin cavity remains constant [10–12, 14, 29, 31]. This effect reaches a point of diminishing returns. Beyond a certain threshold, additional material contributes more to mass gain than strength enhancement. Furthermore, the optimal pin volume for maximizing toughness is not always found to coincide with the volume that maximizes strength [13]. The extrusion volume is a function of the void section and depth.

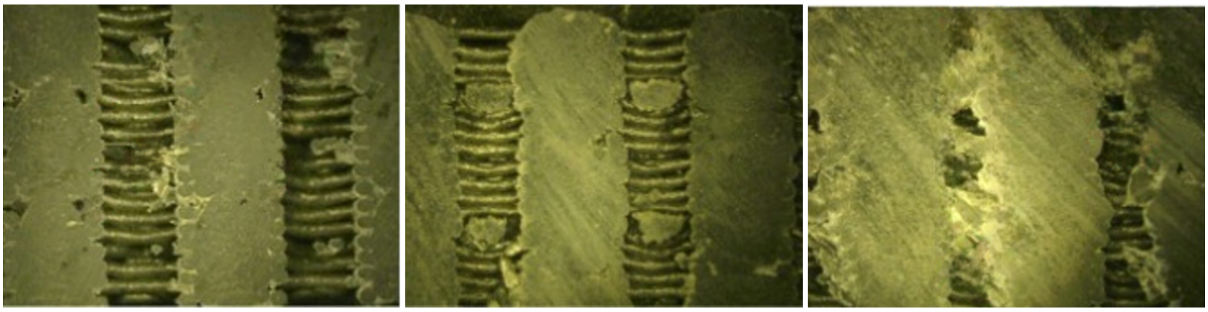

(a) 80% extrusion parameter

(b) 100% extrusion parameter

(c) 120% extrusion parameter

Figure 2.7: Change in pin quality resulting from different extrusion flow parameters. (a) Shows filling imperfections in the form of voids (extrusion volume 80% of geometrical volume); (b) is the result of matching the extrusion volume to the theoretical volume, few imperfections are still present (extrusion volume 100% of geometrical volume); in (c) pins are barely recognizable due to their pronounced overflow (extrusion volume 120% of geometrical volume). Adapted from [13]. [3]

---

[2] The text of the original picture was erased using the online tool `https://cleanup.pictures/`

Impact of pin section and depth on mechanical properties

Pin width and depth have a key impact on the mechanical properties. The length of a pin relative to the overall structure determines the number of seams, which are weak points in the structure [12]. To minimize these discontinuities, slender pins are preferred, as they reduce the number of seam interfaces. Tensile tests confirm that deeper pins significantly enhance fracture toughness, demonstrating the structural benefits of increasing penetration depth. However, deeper cavities present challenges in deposition, as the extruded material tends to deviate and contact the sidewall before reaching the bottom. Such a tendency can lead to bridging effects, where the material accumulates prematurely, creating voids at the base of the pin and overfill at the top [12, 13, 30, 32]. Figure 2.8 allows to compare an ideal pin penetration (Figure 2.8a) with an example of incomplete interlocking caused by poor penetration (Figure 2.8b) and a failed penetration of several layers (Figure 2.8c). To facilitate deeper pin penetration, the hole size can be increased. Although it allows deeper penetration, widening the hole itself does not inherently improve ultimate strength or toughness. Experimental results show that samples with wider holes do not exhibit greater strength or toughness compared to those with narrower holes of the same pin length. Wider pins would theoretically require greater force to break, but fractures rarely occur at the pins themselves. Instead, failure typically occurs at pin-pin seams, where the bonding is weakest. This failure mechanism suggests that the effectiveness of z-pinning is governed by the pin mechanical engagement with the surrounding structure rather than by pin width [13, 30].

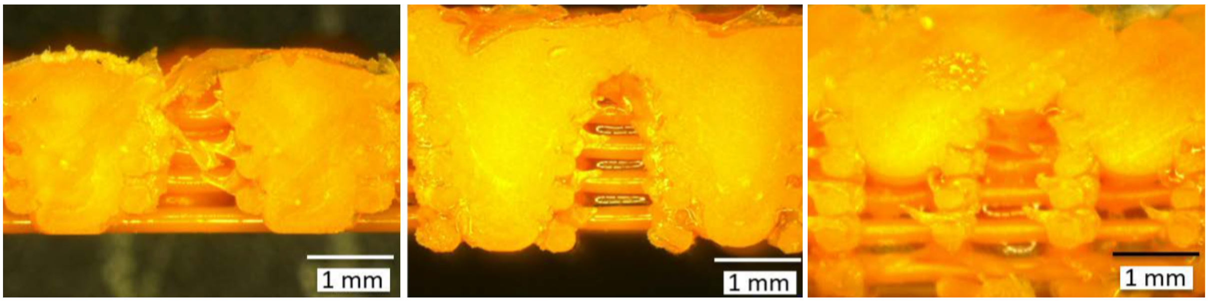

(a) complete pin (b) incomplete pin base (c) mostly incomplete pin

Figure 2.8: Comparison of penetration depth for pins with the same cross section and different depth. a) shows a complete fill including full reaching of the bottom; in b) the fill seems complete, but the pin does not interlock the deepest print lines; c) the penetration depth is much lower than the void depth. Incomplete penetration creates discontinuities in the load path [30].

2.4.2. Application of z-pinning to 3D printed LCP

The incorporation of z-pinning into LCP 3D printing has been examined in a single study [15]. This study investigated the impact of z-pinning, along with other methods, on enhancing the fracture properties of components printed with Vectra® A950 filament. This pinning technique builds on research outlined in the previous subsection, although certain modifications have been applied in its use. Research on 3D-printed LCP pins has focused on assessing their toughening potential, measured in terms of the Mode I strain energy release rate. These characteristics are indirectly linked to tensile strength through strengthening mechanisms. Nevertheless, it is unlikely that enhancements in toughness directly lead to increases in tensile strength, as suggested by pinning research on PLA [30]. The impact of z-pinning on both toughness and tensile strength is shown in Figure 2.9. While the research found the toughening approaches other than pinning to be promising paths, the application of z-pinning did not lead to any significant enhancement in the properties examined. The mechanical test carried out to assess the crack propagation behavior used compact-tension specimens (ASTM D5045). The "initiation strain energy release rate" results are illustrated in Figure 2.9a and suggest no conclusive trends. The study also conducted tensile strength tests on tensile specimens (ASTM D3039). Figure 2.9b reports the performance of the pinned specimens compared to a reference. The reduction in tensile strength caused by pins in the cross-section is by a factor of two. It is essential to note that positioning the pins perpendicular to the testing plane is expected to decrease performance. This observation should not diminish the expectation that pins can enhance strength in the Z-direction. The key takeaway is that pins should be used deliberately, as they imply a tradeoff in the properties of the different planes.

The design options selected in the study influenced the mechanical interaction between the LCP pins and the conventionally printed structure, primarily due to the choices related to infill type, cavity configuration, and infill application. As visible in Figure 2.10, the samples were printed with solid infill. The pin sections are

---

[3] The annotations of the original picture were erased using the online tool `https://cleanup.pictures/`

square and only a few layers deep (4 to 6). The shallow depth of the pin implies few bridging layers, while the cavity's cross-section impairs interlocking between the cavity's "flat" walls and the pin.

Further inspection of Figure 2.10 suggests that the extrusion duration for the pins was likely insufficient for the entire volume to exit the nozzle. This deduction is drawn from the appearance of the pins in Figure 2.10a. The contrast in color between the layer lines (darker) and the pins (lighter) emphasizes the distinction between the two extrusion modes. The lighter top sections of the pins seem to be smeared along the pinning layer, suggesting a premature retraction from the cavity. Figure 2.10b provides further evidence of poor pin quality. This poor quality manifests as incomplete penetration, leading to substantial voids and weakened interlocking.

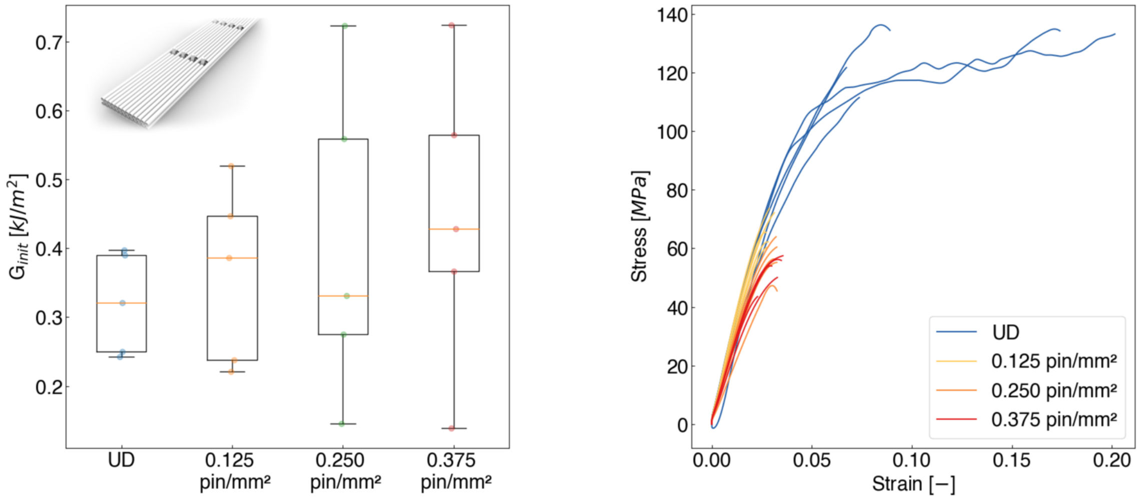

(a) initiation strain energy release rate

(b) stress-strain curve

Figure 2.9: Mechanical test results for state-of-the-art LCP z-pinned specimens. The graphs display the test results of the tested pin configurations, along with reference samples. a) Summarizing strain energy release rates results while b) shows stress-strain curves from tensile testing [15].

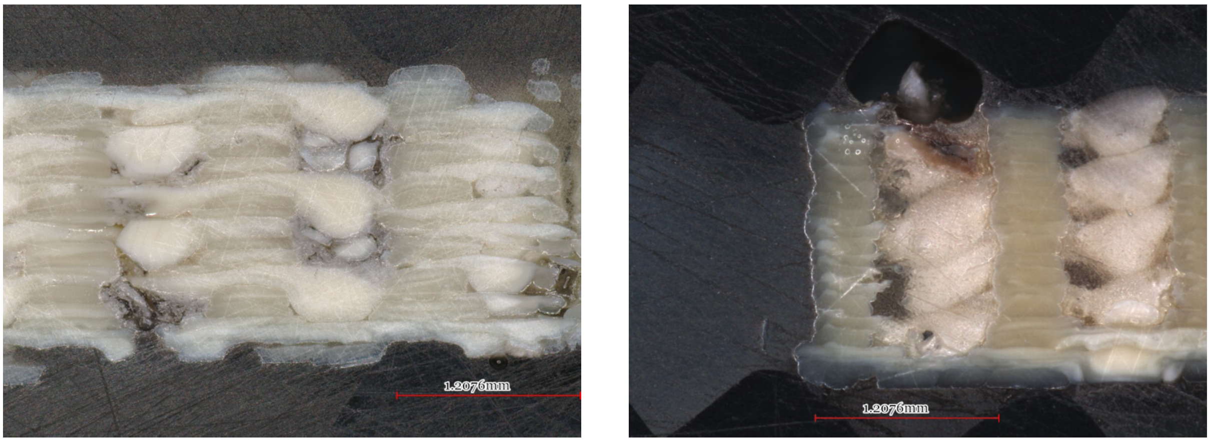

(a) stacking of pins

(b) vertical continuity of pins

Figure 2.10: Cross section of z-pinned 3D printed LCP parts. The pins shown failed to provide the expected toughening due to the poor pin penetration. a) shows pin cavities spanning six layers, while b) shows pin cavities spanning four layers. In both pictures, the pin extrusion material is in a lighter color than the surrounding layer infill [15].

3

Pinning concept and printing setup

This chapter addresses the initial phase of the research process, focusing on establishing the pin concept, drawing from existing literature, and arranging the printing setup to implement the chosen pin concept. In the context of this thesis, the term pin concept is specifically defined to incorporate the general characteristics of the pin's geometry, the mechanism of mechanical interlocking, and its manufacturing process. Developing the setup involves familiarizing oneself with the configurations discussed in the literature and modifying aspects that need to be adjusted for the research on pinning. The chapter begins with Section 3.1, which explains the traditional FFF manufacturing process and modifications needed to accommodate the creation of z-pins. Section 3.2 outlines the pin concept, and Section 3.3 details the adjustments made to the printing setup.

3.1. Integrating pinning in FFF

Z-pinning is a fabrication technique that has yet to gain extensive use in FFF. Due to the novelty of this approach, existing programs lack slicing options for z-pinning. Slicing is the process of converting a 3D model into a set of coordinates that a 3D printer can interpret. Earlier research has explored the practical applications of z-pinning; however, to address the shortcomings of these methods, this study developed a new pin concept. Subsection 3.1.1 discusses the typical manufacturing process in FFF, Subsection 3.1.2 describes the hardware and software components in the initial FFF setup used in the research, and Subsection 3.1.3 outlines the conceptual adjustments to the typical workflow.

3.1.1. Standard FFF manufacturing workflow

The FFF production process can be broken down into three main stages: digital design, slicing, and 3D printing. Although the term FFF typically refers to the final stage, it is advantageous for this study to encompass both design and slicing phases, as these specifically impact the quality of the final print. Figure 3.1 illustrates these three stages of the manufacturing process. Figure 3.1a depicts the design phase, Figure 3.1b illustrates the slicing step with slicing software and Figure 3.1c illustrates the printing using an Ultimaker 2+. The slicing step is typically performed using dedicated software developed in conjunction with advancements in the FFF field. Such slicing software is optimized for standard printing approaches, resulting in academic research often prioritizing the use of alternative slicing programs. During slicing, a wide array of settings must be chosen based on the material, printer specifications, and desired print characteristics. The printing hardware consists of the extrusion filament, the physical printing equipment (including an assembly of electronic motors, axes, heaters, and various sensors), and the firmware that operates this hardware. After designing with CAD software, the file (in .stl or .step format) is processed by a slicer, which translates it into a .gcode file compatible with the printer's firmware. This process involves the use of three separate software programs.

3.1.2. Initial hardware and software setup

Modifications to the conventional FFF manufacturing workflow are a central part of this research. Therefore, it is essential to outline the initial configuration, which is determined by the available hardware and insights from prior research. This research does not primarily focus on the CAD process and, as a result, it will not be elaborated upon extensively. The software used is 3D Experience (3DX). This section focuses instead on the FFF filament used, the printing hardware, and the slicer software employed in the research.

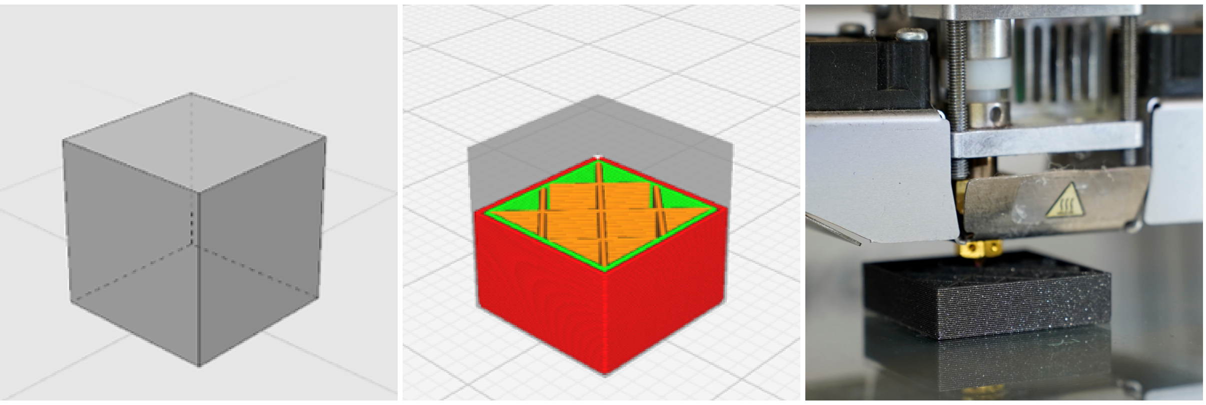

(a) CAD (b) slicing (c) 3D printing

Figure 3.1: Three phases of the FFF manufacturing workflow. Initially, the digital design of a component is depicted in (a). The next step involves slicing, which is illustrated in (b). Lastly, in (c), the process concludes with 3D printing.[1]

Material

The material used in the study is an LCP filament produced by NematX AG. The spools are manufactured by converting Vectra® A950 pellets into filament. An example of a spool is shown in Figure 3.2a. The material is a "thermotropic random copolyester HBA:HNA (4-hydroxy-benzoic acid and 6-hydroxynaphthalene-2-carboxylic acid) with a proportion of 73:27" [4]. HBA:HNA is the same material employed in all investigations on LCP FFF conducted at the Shaping Matter Lab[2] [4, 6, 9, 15, 23, 26, 27, 34–36] and is comparable to that used in earlier pertinent studies [3, 23–25, 28, 37]. This thesis focuses on material processing rather than material science. For a comprehensive overview on molecular morphology, microstructure, and physical properties, the reader is recommended to refer to Chapter 2 of [4].

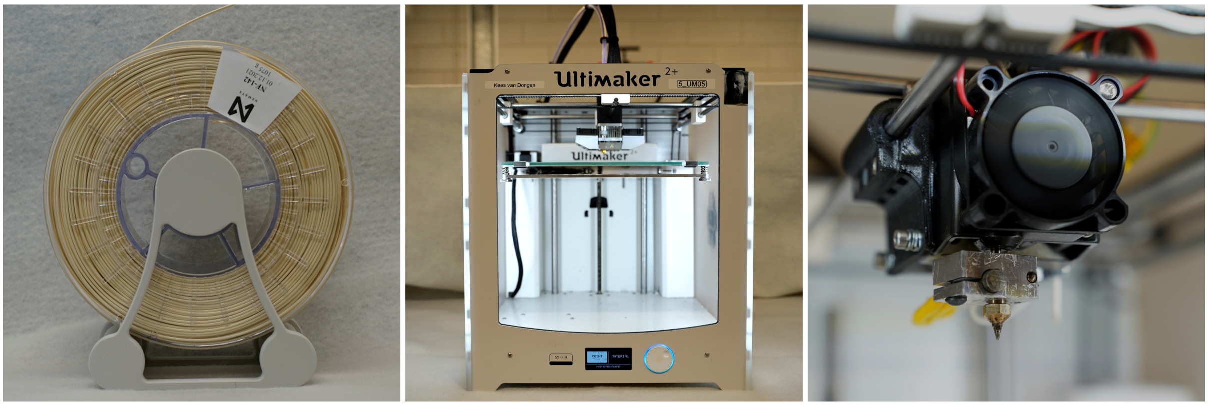

(a) LCP filament (b) Standard Ultimaker 2+ (c) Hemera extruder

Figure 3.2: Printing hardware used in the study. (a) shows a filament of Vectra® A950 filament from NematX, (b) is an example of Ultimaker 2+ without any modification, and (c) portrays the Hemera extruder mounted on the Ultimaker 2+ used in the study.

Printing Hardware

The printer model used throughout the study is the Ultimaker 2+ 3D printer shown in Figure 3.2b. Before this research, modifications were made to the printers, where the standard Ultimaker 2+ Bowden extruder was replaced with a direct-drive E3D Hemera extruder system. Figure 3.2c shows the Hemera extruder mounted on the Ultimaker 2+ with a V6 hotend. Such an extruder allows for improved control over the extrusion volume, and its metal body is necessary to operate at the high printing temperatures required for LCP (above 275°). This modified printing setup closely resembles the configurations used in previous research [3, 4, 9, 23–26, 36]. The choice of the Ultimaker 2+ over other hardware options, such as the Prusa i3 MK3S+ mentioned in other studies [6, 15, 34–36], was driven by the need for a dedicated printing platform. This platform would be

---

[1] Subfigure (a) was obtained using 3DX, subfigure (b) was obtained using the slicer Cura, subfigure (c) is a picture of an Ultimaker 2+.

[2] Shaping Matter Lab (SML) is a research group within the Department of Structures and Materials of Faculty of Aerospace Engineering at the Delft University of Technology

available for custom software and hardware adjustments without interfering with concurrent research on FFF of LCP that is also occurring in the same lab. Opting for an FFF printer like an Ultimaker 2+ has its downsides, the most notable being the absence of bed leveling features and inconsistent z-axis homing. [3]

Slicer

A slicer is a software that converts a CAD model into G-code. Several open-source slicers are both user-friendly and feature-rich. Figure 3.3 serves to demonstrate the level of customization possible in the manufacturing process by altering the infill parameters. Starting from a single design (Figure 3.3a), diverse infill ratios and patterns result in variations in mechanical performance and cost.(Figure 3.3b, Figure 3.3c and Figure 3.3d). The slicer Cura was utilized in previous research with the Ultimaker 2+ printer alongside Vectra® A950 filament, making it the initial choice for this study.

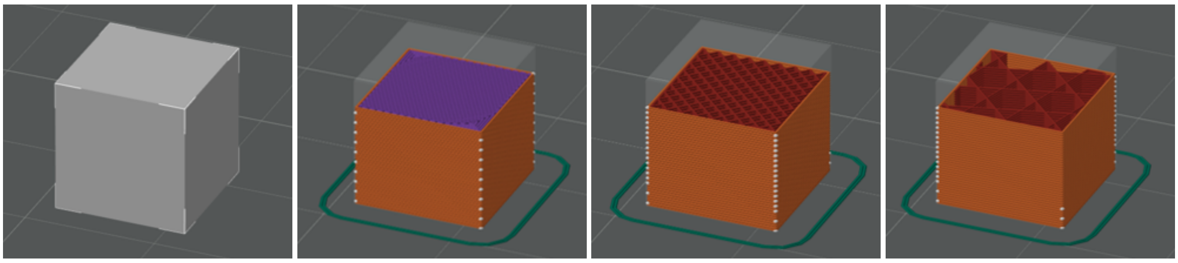

(a) part before slicing (b) solid infill (c) 50% rectangular infill (d) 25% cubic infill

Figure 3.3: Tunability of printing infill in a regular slicer. (a) displays the geometry of the part before slicing, while (b), (c), and (d) depict the G-codes that result from using various infill settings. These diverse infill configurations lead to distinct internal geometries within the same part. The violet color indicates solid infill, the red indicates sparse infill, and the orange stands for perimeter lines. [4]

3.1.3. Updating manufacturing workflow for pinning

Current slicers offer a broad range of functionalities, but pinning is not among them. The conventional FFF manufacturing process must be adjusted to include the printing of pin cavities and to execute the extrusion of the pins. Previous research utilized infill patterns to craft spaces for pins in a printed part and relied on custom G-code for pin extrusion [10–14, 30]. This study, however, aspires to have greater flexibility regarding cavity geometry to maximize pin mechanical interlocking in a part with solid infill. The specific considerations behind this choice are discussed in Subsection 3.2.3. Since cavities within infill lines cannot be utilized, pin cavities must be created through alternative methods. Other research reports designing custom slicer using Rhino Grasshopper [15], yet this method is considered overly time-intensive.

Embedding pin cavities in part geometry

The strategy selected for this research involves embedding cavities directly into the part design. The benefit of this approach is its simplicity, as it doesn't imply slicer code modification. The benefit of this approach is its simplicity, as it doesn't require slicer code modification. However, by bypassing the slicer's automation, this method introduces additional manual steps, which increases the likelihood of human error and complicates the workflow when testing different pin geometries. The altered manufacturing process to include pin cavities is illustrated in Figure 3.4. Figure 3.4a and Figure 3.4b demonstrate the creation of pin cavities within CAD. In Figure 3.4c, the slicer interprets the hole as an external surface and prints a perimeter around it. This is advantageous because having a dedicated perimeter line helps maintain the cavity profile's tolerances. In Figure 3.4d, the part is printed without issues.

Formulating pinning G-code

In literature, material was extruded in the pin cavity using custom G-code [10, 15, 38]. Since those pinning G-code programs were not made publicly available, it was necessary to formulate our own method. Initial tests used handwritten G-code with Excel for calculations, then manually inserted into the slicer-generated G-code.

---

[3] The Ultimaker 2+ is an old 3D printer. Ultimaker announced discontinuing the Ultimaker 2+ product `https://support.ultimaker.com/s/article/1667411067304`.

[4] The figures are obtained using OrcaSlicer.

Simple top-down pinning requires basic commands: positioning the nozzle above the cavity and extruding, achievable with as few as two G-code lines. A Python program was developed to automate the G-code post-processing, improving reliability and increasing the achievable complexity.

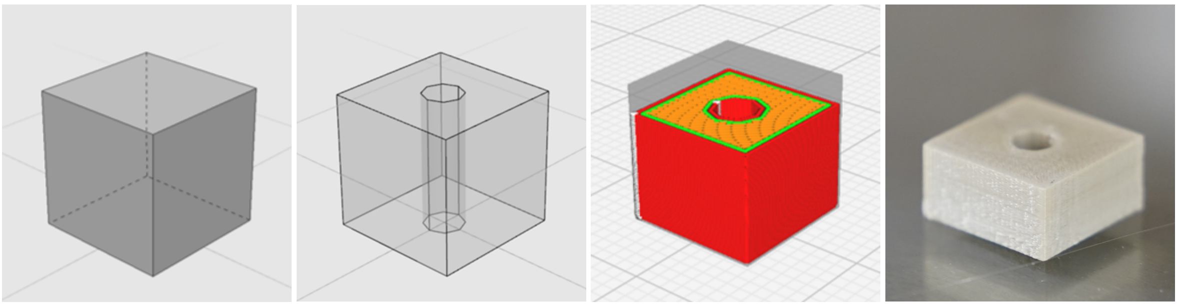

(a) standard CAD part (b) part with integrated cavity (c) sliced part with cavity (d) printing of part with cavity

Figure 3.4: 3D printing workflow to manufacture parts with pin cavities. (a) illustrates the CAD component intended for pinning, (b) depicts the component with the cavity included, (c) presents the sliced view of the part with the cavity, and (d) displays the successful print of the cavity for the pin. [5]

The program performs three main tasks: positioning pins in the selected cross-section, generating G-code commands, and modifying slicer G-code. First, it processes input about part dimensions and pin cavity sizes to output x and y cavity coordinates and assess feasibility. The second phase takes input from the prior phase and includes additional data on essential slicing parameters, such as layer height. It also incorporates specifics regarding the pin configuration, including pin height, as well as details concerning the extrusion process of the pins, such as extrusion speed. The data is utilized to produce both the G-code commands and instructions for the third step. In the third phase, the G-code output by the slicer is analyzed, and, according to the instructions from the previous step, the pinning G-code commands are integrated into the slicer's G-code. The pinning G-code injection procedure is depicted in Figure 3.5. Figure 3.5a presents a sample of G-code from a slicer, where the program identifies layer transitions. After the identification, the script inserts the pin extrusion G-code, as demonstrated in Figure 3.5b. In Figure 3.5c, the nozzle is depicted completing the three steps from Figure 3.5b. The nozzle first completes a layer, extrudes the pin, and then continues with printing the next layer. Leveraging Python for task automation enables pinning for numerous large parts, handling more intricate pin geometries and arrangements, and generating highly customizable pinning G-codes.

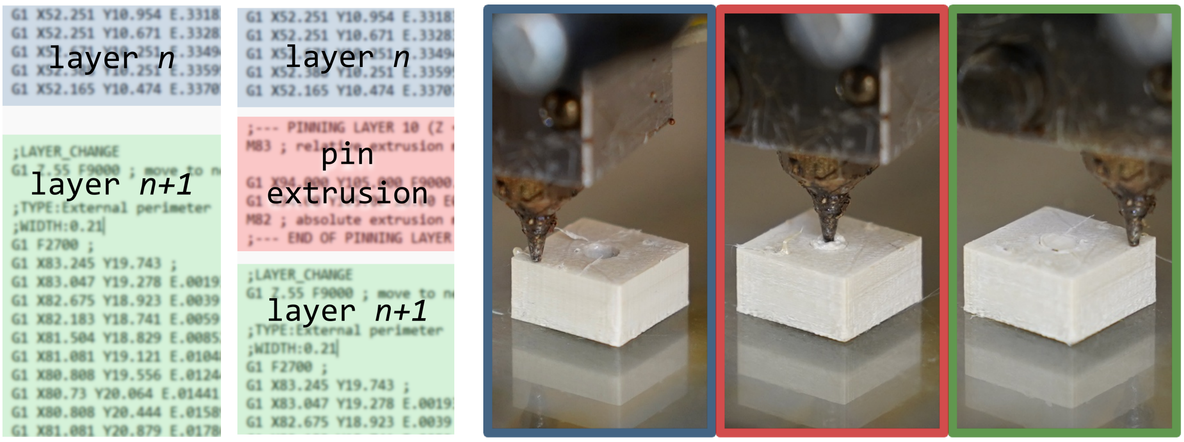

(a) slicer gcode (b) post-processed gcode (c) pinnig sequence

Figure 3.5: Enhancement of standard sliced G-code through post-processing to incorporate pinning directives. (a) And (d) illustrate the process by which the Python script examines standard G-code, initially identifying layer transitions and subsequently inserting G-code for pinning at predetermined points. (c) Displays the nozzle extruding material during the three phases of G-code from (b).

The segments of G-code commands inserted during post-processing and repeated across a pinning G-code are referred to as the pinning routine due to their similarity. In this study, the pinning routines are divided into

---

[5] Subfigures (a) and (b) are images obtained using 3DX. Subfigure (c) is obtained using the slicer Cura.

three stages: placing the nozzle at the desired location, executing the extrusion, and performing a wipe. [6] The nozzle positioning step aligns the nozzle with the pin's location and encompasses all pre-extrusion actions. Once the nozzle is accurately positioned, the extrusion phase begins. The collection of commands during this phase is termed the extrusion routine, which will undergo significant development in Section 4.2. Finally, after completing the extrusion, a wiping motion is performed to clear any surplus material from the print layer. Unexpected over-extrusions could result in flaws that might propagate throughout the part's height like ripples. The pinning routine was iteratively developed and incorporated in the test specimen manufacturing reported in Chapter 5.

The Python program developed is available at `https://github.com/LorenzoOnorato/z_pinning_fff_research` or alternatively at `https://github.com/LorenzoOnorato`

3.2. Pin concept

Initial attempts at pin extrusion indicated that the pinning method documented in the literature is not suitable for Vectra® A950 printing. Top-down pinning struggles to produce consistent pins that can bear loads with this material, whereas, although not experimentally tested in literature, bottom-up pinning promises improved pin quality and enables exploration of more intricate pin geometries. Subsection 3.2.1 addresses the challenges of top-down printing, Subsection 3.2.2 covers bottom-up pinning, and Subsection 3.2.3 focuses on the design of pin cavity concepts.

3.2.1. Top-down pinning

Most of the experimental studies on z-pinning employed a method that can be defined as top-down pin extrusion. In this method, the nozzle aligns with the pin cavity, lowers to touch the previously deposited layer, creating a "seal", and then extrudes the molten filament into the cavity. This approach's main benefit is that it doesn't require specialized equipment. However, literature highlights its drawbacks, such as limited penetration depth and inadequate control over the pin's shape [13, 30]. Although studies on 3D printed Vectra® A950 do not explicitly mention penetration issues, the reported pin configurations are relatively shallow, which limits the pin effectiveness [15].

The potential of employing a top-down pinning method was examined using the own setup. Figure 3.6 illustrates two instances of failures in pin extrusion. Figure 3.6a depicts a scenario where top-down pinning is attempted on a cavity that exceeded the nozzle's diameter, resulting in a pin with a non-uniform structure that not only fails to fill the cavity homogeneously but also does not adhere to its walls [29]. In contrast, Figure 3.6c presents pinning in a cavity with dimensions equal to the nozzle diameter. Here, although the resulting pin appears to have a uniform structure, it does not reach the cavity's bottom. This shortcoming is attributed to the material cooling prematurely, obstructing the cavity and leading to over-extrusion [29]. Figure 3.6b and Figure 3.6d show sections of failed pin extrusions from our early pinning attempts. Despite differences in the materials used, the two pin extrusion failure types described in the literature closely align with the results of our own experiments. To address the difficulties in obtaining homogeneous pins of controlled depth, literature recommends the use of penetrating nozzles [29, 33].

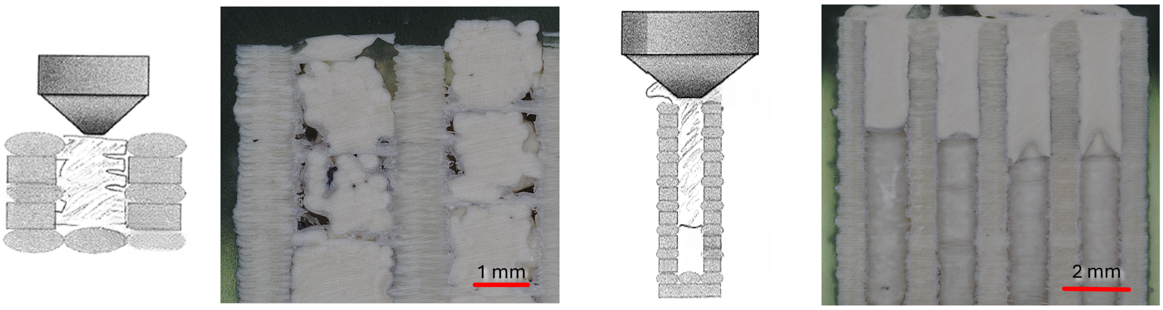

(a) wide cavity (b) own experiment on wide cavity (c) deep cavity (d) own experiment on deep cavity

Figure 3.6: Extrusion defects occurring using top-down pinning extrusion approaches. (a) Illustrates incorrect pin formation, where the cavity width surpasses the nozzle's diameter, while (b) depicts a pin extrusion issue where the material does not extend to the pin's base, resulting in over-extrusion. Subfigures (a) and (c) are adaptations of Figures 1 and 2 from [33]. [7]

---

[6] In slicing terminology, G-code commands concerning movement are classified into extrusion and travel moves. Travel moves do not entail filament extrusion. A wipe command is a type of travel move intended to clean the nozzle of any unwanted material adhering to it.

3.2.2. Bottom-up pinning

The utilization of pin penetrating nozzles in experimental z-pinning research has not been documented. Existing literature references to penetrating nozzles are confined to a thermal simulation evaluating their feasibility [29]. Additional references to this method are found within 3D printing community forums and patents [33], although there exists no scientific research in this domain. Figure 3.7 demonstrates the idea of bottom-up extrusion for a cylinder-shaped cross section Figure 3.7a and a wedged pin section Figure 3.7b. It's important to consider that this method requires the nozzle to have a sufficiently slender design to fit within a pin cavity. In addition to potentially enhancing pin extrusion quality, a notable benefit of this technique is its ability to facilitate extrusion of mechanically interlocking pin sections in solid infills, as illustrated by the example in Figure 3.7b. The bottom-up pinning approach was adopted for this research due to its theoretical benefits.

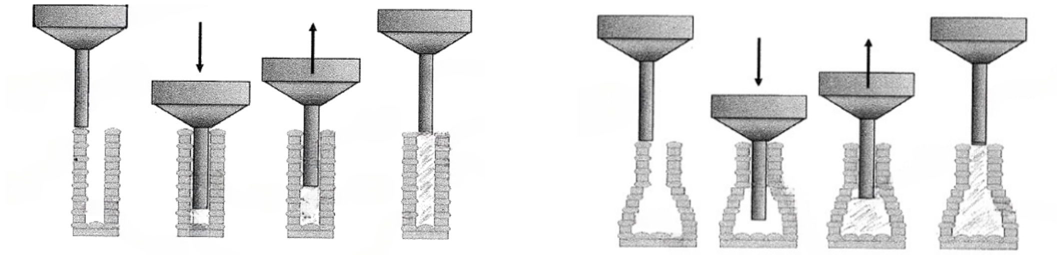

(a) cylindrical pin cavity

(b) wedging pin cavity

Figure 3.7: Visualization of bottom-up pin extrusion for different types of pin cavity. Two subfigures illustrate a unique nozzle configuration featuring a slender, extended tip that descends into a pin cavity and extrudes while lifting to fill the cavity. (a) presents a cylindrical pin cavity, whereas (b) displays a wedged pin cavity. The images are adaptations of Figures 3 and 4 from [33]. [8]

3.2.3. Pin design for mechanical interlocking

Literature on z-pinning focused on pins extruded in the voids resulting from a rectangular infill pattern [10–14, 30, 31]. As introduced in Subsection 2.4.1, these voids do not constitute discrete cavities of a specific volume; rather, they are open sections partially restricted by the alternating scaffolding of infill lines. This method benefits from simplicity in its implementation and inherently facilitates mechanical interlocking between pins and layer infill. Nevertheless, this approach exhibits limitations, including the inability to regulate the precise geometry of the pins, the confinement to a singular cavity design, and the prevention of direct alterations to pin dimensions such as height and width. These aspects are determined indirectly by printing parameters, notably layer height and infill density. This interdependence of pin geometry, printing parameters, and infill density complicates the isolation of pin parameters for examination through parametric studies.

The alternative approach selected for this study involves printing a solid part that incorporates pins, where the layer infill is specifically designed to accommodate pin cavities [15, 38]. Unlike the previously discussed method, which results in infill voids from a rectangular pattern, this strategy ensures that the overall macroscopic result is a solid part, regardless of the number of pins. Transitioning to a solid infill presents the challenge of ensuring mechanical interlocking due to the cavities being bounded by flat surfaces. As established in Subsection 2.4.1, z-pinning cannot depend on molecular interactions for load transfer. Achieving mechanical interlocking mandates the creation of a pin with a varying cross-sectional area, which becomes wedged between layers because of its shape.

Crafting a pin with a more complex geometry poses manufacturing challenges. The main limitations of printable geometries are the maximum overhang angles for the cavity and narrow spaces that the extrusion of a viscoelastic polymer may inadequately fill. In Figure 3.8, the evolution from the basic pin section commonly seen in literature to the one implemented in this research is illustrated across four stages. The basic cylindrical shape depicted in Figure 3.8a lacks mechanical interlocking capabilities, which is why grooves are added to the flat surfaces in Figure 3.8b. These grooves are intended to facilitate the gradual transfer of loads; however, the sharp overhang created by a groove poses challenges for reliable printing and obstructs the penetration of the cooling extruded material. Decreasing the angle of the overhang brings to the design illustrated in Figure 3.8c. A single wide groove, in the design in Figure 3.8d, allows tapered nozzles to execute bottom-up pinning, which would otherwise necessitate the use of custom-made narrow nozzles. The chosen pin cross-section consists of a cylindrical core and two truncated conical sections at the ends to facilitate load transfer.

---

[8] The annotations of the original figure were erased using the online tool `https://cleanup.pictures/`

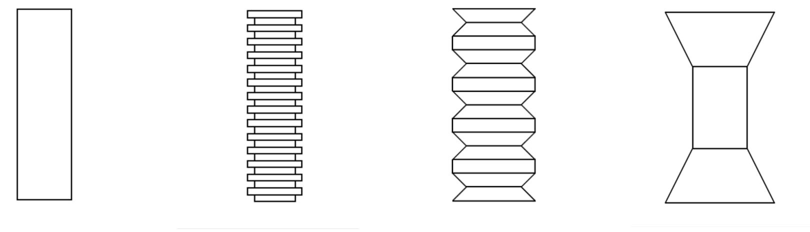

(a) cylinder

(b) cylinder with undercutting layers

(c) cylinder with undercutting sections

(d) wedging pin

Figure 3.8: Pin cavities with varied profiles and different potential for mechanical interlocking. (a) illustrates a cylindrical pin cavity, (b) depicts a pin cavity with grooves for load transfer, (c) represents a section with grooves requiring lower overhang angles, (d) displays a section of a pin with cylindrical core and two truncated conical sections.

Once the section of the pin cavity is determined, the concept's definition progresses to manufacturing the individual pin and arranging pins in the cross-section. The concurrent design of the pin and the bottom-up pinning strategy is crucial to ensure the nozzle can perform bottom-up extrusion and that the pin geometry is compatible with the material. Figure 3.9a demonstrates how a tapered nozzle may be limited in the penetration of the pin cavity, potentially leaving narrow sections unfilled. Pin arrangement requires optimization, and deliberate configurations should be developed. The use of wedging pins adds complexity by varying the ratio between pin infill and layer infill throughout the part's height, as illustrated in Figure 3.9b. For simplicity, pins will be vertically aligned in columns that are staggered relative to each other, following existing literature [12]. Earlier studies employed pins with a square vertical section; however, this study opted for a circular section, as it better accommodates the radial flow from a nozzle. The detailed design of pin geometry and the extrusion process to produce it are covered in Chapter 4, while the staggering of pin columns is discussed in Chapter 5.

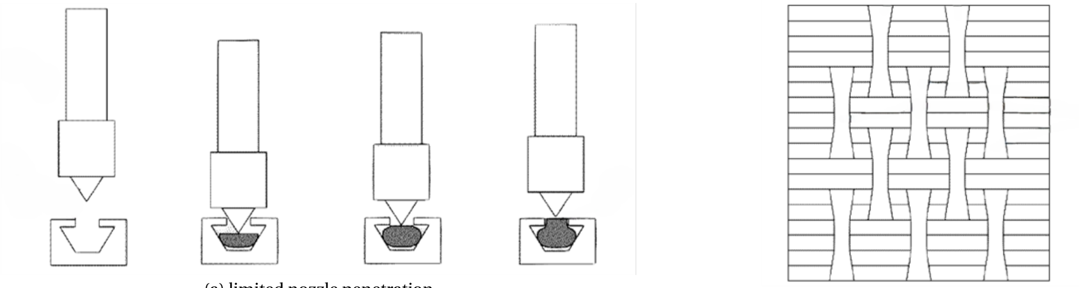

(a) limited nozzle penetration

(b) wedging pin arrangement

Figure 3.9: Complexity of wedging pin designs. (a) illustrates the difficulty of filling undercuts in a wedging pin design, even with a bottom-up pinning method. (b) demonstrates the necessity of arranging wedging pins in patterns that result in a variable cross-section through the part's height. The images are adaptations of Figures 5 and 8 from [39]. [9]

3.3. Updates to the printing setup

After conducting initial pinning trials and formulating the pinning strategy for this study, it became essential to update the original printing setup. Hardware changes consisted of choosing a nozzle suitable for bottom-up pinning. The nozzle is the sole alteration to the physical printer that sets this research apart from previous Vectra® A950 printing studies. On the software side, the printer was updated with cutting-edge firmware, and an optimized slicer replaced the outdated Cura. Subsection 3.3.1 discusses the nozzle selection, Subsection 3.3.2 briefly presents the benefits of the new firmware, and Subsection 3.3.3 demonstrates the noticeable enhancement in hole printing quality achieved with the updated slicer.

3.3.1. Nozzle diameter and taper angle

Selecting a suitable nozzle is crucial for bottom-up pinning. Previous studies on FFF of LCP mechanical components predominantly used standard V6 nozzles with a diameter of 0.4 mm [4, 6, 26–28, 35]. Research concerning FFF of LCP focuses on smaller nozzle diameters exclusively for research on extruded fiber [3, 4, 23, 25]

---

[9] The annotations of the original figure were erased using the online tool `https://cleanup.pictures/`

or print quality improvements [37]. Several reasons guide the choice of nozzle for this study toward smaller diameters than the widely adopted 0.4 mm. Printing with smaller nozzles accentuates the anisotropy between in-plane and out-of-plane properties. While poor layer adhesion is usually considered detrimental, it is the exact weakness that z-pinning aims to mitigate. This way, printing pinned parts with smaller nozzles allows obtaining high in-plane properties [3, 4, 24] while leveraging the pins for load transfer between layers. Printing slender pins is more desirable than stout ones. The reason is twofold: slender pins lead to larger improvements in mechanical properties [12, 13, 30] and require a smaller test-specimen cross-section, and minimizing part size decreases required printing time and material. Thin pins and, in general, the small geometrical features demanded by industrial applications require small nozzle diameters despite the higher process complexity. Overall, using a nozzle diameter that is lower than the standard 0.4 mm better reflects real-world applications.

The nozzle diameter chosen for the study is 0.2 mm. Narrower nozzle diameters are made inaccessible due to poor market availability. Figure 3.10 shows a collection of nozzles to illustrate the selection of the preferred design. Nozzles A, B, and C are common brass nozzles for FFF. Nozzle D consists of a brass airbrush nozzle with a steel tip. In contrast, nozzle E is a steel Tecdia Arque nozzle with an extra narrow tip section. [10] Besides the material, the primary distinction in the nozzle designs lies in the tip taper angle, highlighted in white in the image. Narrow taper angles allow plunging deeper in slender pin cavities. Consequently, Nozzles D and E are favored. The airbrush nozzle design (D) demonstrated more consistent print quality during testing and was selected for the continuation of the study.

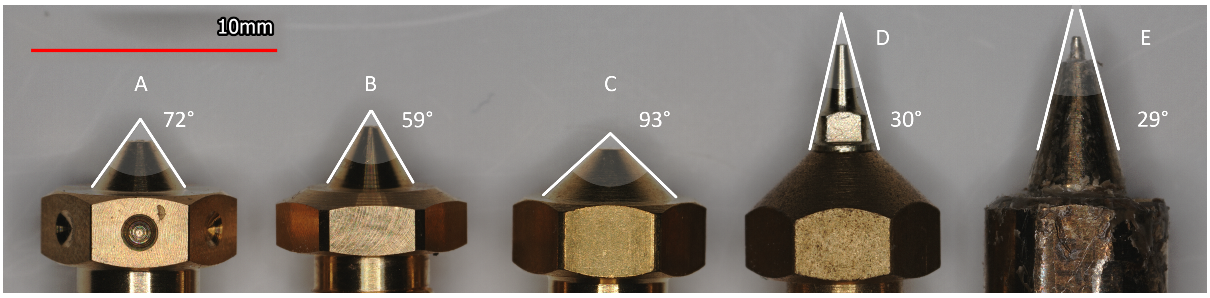

Figure 3.10: Nozzle designs considered for research on z-pinning. Nozzle A represents a typical FFF nozzle, made of brass with a 0.4 mm diameter. Nozzles B and C are also made of brass but have diameters of 0.2 mm and different taper angles. Nozzle D is an airbrush nozzle with a brass body and a narrow steel tip. Nozzle F is a custom Tecdia Arque, featuring a sharp profile, a steel body, and an extra-thin tip. The taper angles of the nozzles are indicated in white.

3.3.2. 3D Printer firmware

The original firmware running the Ultimaker printer was replaced with Klipper. [11]. Using the original Ultimaker software rendered the exact operation of the printer obscure, whereas both the documentation and user interface of Klipper give insight into how the G-code commands are effectively executed. Transparency in the executions of the commands has been particularly valuable for the development described in Section 4.2. Klipper also enabled several additional practical enhancements. In summary, these improvements are: the option for mid-print z-offset adjustments, remote monitoring, and increased maximum bed temperature. All of these features mitigate the issue of inconsistent distance between the nozzle and the print bed that affects the Ultimaker 2+ printer. The quality of the initial printed layer is crucial to avoid the premature detaching of slender parts. The configuration files used in the Klipper software setup are attached in **??**. Enhanced software usability reduced material waste and facilitated troubleshooting at various stages of the development.

3.3.3. Slicing Software

The slicer initially adopted, Cura, was quickly replaced by NematX Slicer (v2.7.61.0). [12] The new slicer was chosen over other available slicers (Cura, PrusaSlicer, OrcaSlicer, Superslicer), due to its better implementation of two specific slicing features: "avoid crossing perimeters" and "XY hole compensation". When fabricating com-

---

[10] The Tecdia Arque is a line of high-quality nozzles with a characteristic inner cavity geometry. It was borrowed from the filament manufacturer NematX. The link to the nozzle official website is `https://us.tecdia.com/products/hf/detail/precision/arque/`.

[11] Klipper is an open-source 3D printer firmware designed to improve performance and flexibility of FFF printers by offloading computational tasks from the printer's microcontroller to a more powerful external computer `https://www.klipper3d.org/`.

[12] NematX Slicer was developed and recommended by the filament supplier.

ponents with internal voids, such as pin cavities, it becomes necessary to prevent crossing perimeters during travel movements to prevent cavity occlusion. The "avoid crossing perimeters" feature is especially crucial for 3D printed Vectra® A950, as its oozing tendency is more pronounced than that of standard 3D printing materials. XY hole compensation is an option found in slicers as a single offset parameter to address the tendency of FFF to undersize small holes. For research on z-pinning, the accurate hole size is highly relevant, as it impacts the mechanical interaction between pins and the traditionally deposited material. The mismatch between void volume and extruded pin volume can result in low mechanical interlocking, over-extrusion, and print failure [11, 13, 14, 14, 30, 31]. When having a single XY hole compensation offset value, this is optimized for a single hole diameter. NematX slicer extends this functionality by allowing the creation of an offset curve, enabling the variation of the offset across a range of hole sizes. This extension is beneficial for components with cavities that vary in diameter across the layers. Parameter fine-tuning is sensitive to slicing parameters and hardware combinations, so improvements in the print quality followed an iterative tuning process.

Transitioning from OrcaSlicer to a tuned NematX Slicer yielded the enhancements in printing quality visible in Figure 3.11. In Figure 3.11a, stringing lines are obstructing the tuning stencil's holes, while in Figure 3.11b there are no stringing lines. The improvement is due to the better implementation of the *avoid crossing perimeters* feature in NematX Slicer. The subtle difference between Figure 3.11b and Figure 3.11c lies in the holes' dimensions. The holes in Figure 3.11b are undersized compared to those in Figure 3.11c, where their diameters exhibit an average deviation of 2.5% thanks to the tuning of the XY hole compensation curve. Details on the parameters used and iteration progress are documented in Appendix A. Employing a slicer with enhanced features and adjusting its settings yields better print dimensional accuracy, which is crucial for more precisely controlled pin extrusion.

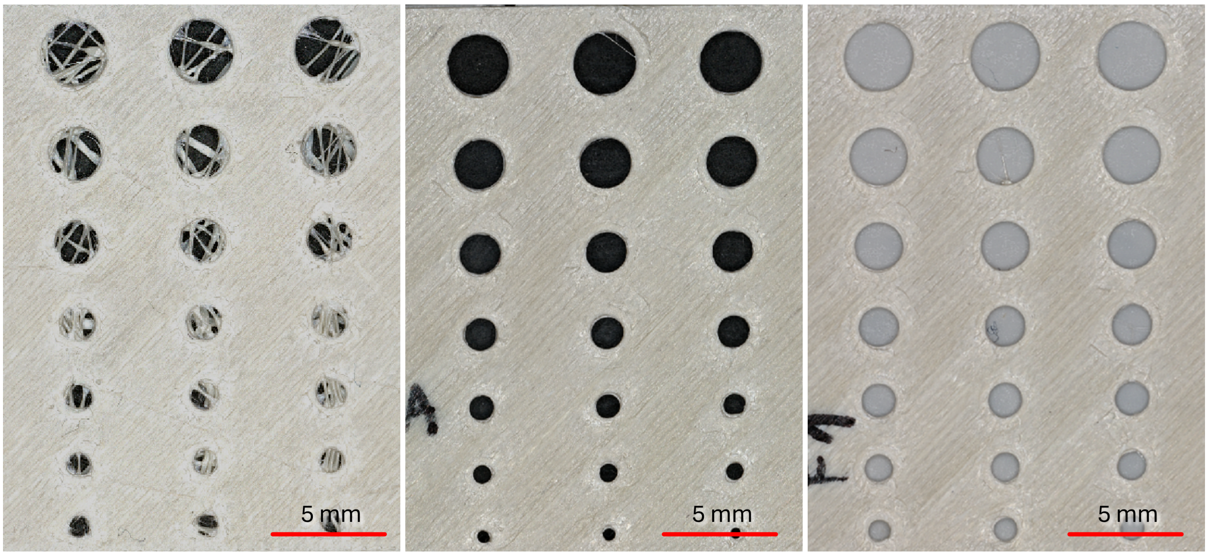

(a) Orca Slicer (b) untuned NematX slicer (c) tuned NematX Slicer

Figure 3.11: Improvement in printing quality of the holes through adoption and tuning of NematX Slicer. Switching from OrcaSlicer, in (a), to NematX Slicer, in (b), greatly enhances printing quality by preventing stringing across holes. In (b), holes are undersized, but iterative tuning reduced the average hole diameter error to below 2.5% as shown in (c).

3.4. Chapter summary

This chapter presented the conceptual framework, workflow integration, and hardware modifications required to implement z-pinning in FFF manufacturing using Vectra® A950. The objective was to adapt each stage of the process (pinning method, slicing workflow, and printer configuration) to support controlled insertion of vertical pins, which are not natively supported by existing software or hardware. The result is a complete workflow capable of producing discrete pins with repeatable geometry and positioning.

The chapter began by describing the integration of pinning within the fused filament fabrication workflow. The standard FFF process, which comprises digital design, slicing, and printing, does not accommodate non-standard vertical insertions. As a result, the slicing process was conceptually separated into two stages: base geometry slicing and pin-specific G-code generation. The new workflow requires the insertion of custom G-code commands for the pin extrusion events into the G-code for the base geometry generated by a conventional slicer.

Following the workflow design, the pinning method was defined. Conventional top-down pinning approaches, which deposit filament vertically into preformed cavities, were found to produce inconsistent and shallow pins, especially when applied to Vectra® A950 filament. Typical defects included incomplete filling and irregular pin formation due to limited control over extrusion within the cavity. In response, a bottom-up pinning strategy was proposed. This approach inverts the process by building up the pin from the base of the cavity. It also enables the manufacturing of more complex pin geometries. The design of the pin cavities was established by introducing geometric features that promote better mechanical interlocking.

The final part of the chapter focused on updates to the hardware and software that were necessary to enable the proposed pinning process. A small-diameter nozzle was selected to allow higher spatial resolution and improved pin shape accuracy, deviating from prior work on Vectra® A950 printing. Firmware on the printer was upgraded to support customization and provide greater control over extrusion timing. Additionally, the slicing software was replaced to improve print quality. These changes were implemented to accommodate the requirements of bottom-up pinning while maintaining compatibility with the rest of the FFF process.

4

Design of pins and pinning routine

This chapter focuses on transitioning the concept from the prior chapter into a tangible set of geometrically defined, manufacturable pin variations. It outlines the possible pin sizes and their quantities for the test specimen discussed in Section 4.1. Section Section 4.2 addresses the development of an extrusion routine that manages extrusion timing delays, ensuring the production of load-bearing pins.

4.1. Pin design

This section provides an elaboration on the definition of the pin geometries that will be analyzed in the next chapter. While the conceptual pin geometry was introduced in the preceding chapter, this section emphasizes specifying the precise geometrical dimensions. These dimensions are determined by considerations on the manufacturing processes, the concept definition, and the pin infill. Pin infill is identified as a crucial parameter due to its significant impact on both cost and mechanical characteristics. The section is structured in three parts: Subsection 4.1.1, which defines pin infill; Subsection 4.1.2, which outlines the design space, enabling selection of design points based on pin number and diameter; and finally, Subsection 4.1.3, where the variations in pin height are established.

4.1.1. Pin infill parameter

Infill density in 3D printing and fiber volume fraction in FRPs play a comparable role in governing overall part performance. Both parameters balance mechanical properties against material usage and cost. In FFF, increasing infill density results in greater material consumption and longer printing times, but also enhances part stiffness and strength. Similarly, in FRPs, fibers bear most of the structural load, and, within limits, higher fiber content leads to improved mechanical properties, although at increased cost. Introducing pins into the infill adds complexity to the 3D-printed part. While a standard print is typically seen as a combination of filament and air, pinned parts are better described as composites composed of layer infill and vertical pins. This analogy is visually supported by Figure 4.1, which compares sections of pinned parts (Figure 4.1b, Figure 4.1d) with those of CFRPs (Figure 4.1a, Figure 4.1c), highlighting the structural similarity between pins and fibers in both perpendicular and parallel orientations. By analogy to infill density, which defines the ratio of printed material to voids, we define pin infill as the volume fraction allocated to vertically extruded pins, representing a discrete reinforcement phase within the structure.

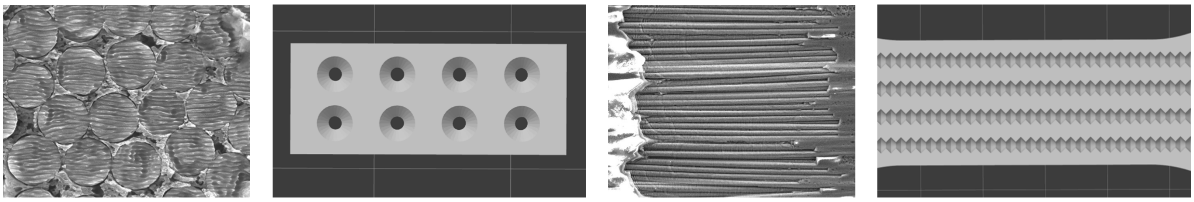
(a) Section of CFRP perpendicular to the fiber direction

(b) Section of a pinned part perpendicular to pinning direction

(c) Section of CFRP parallel to the fiber direction

(d) Section of a pinned part parallel to pinning direction

Figure 4.1: Comparison between sections of CFRPs and parts intended for pinning. (a) and (b) illustrate the similarity in the sections, while (c) and (d) highlight the oriented nature of the reinforcement. Subfigures (a) and (c) are adapted from [40].

Determining the appropriate value for the pin infill parameter in a given configuration poses several challenges. In FRPs, mechanical properties are typically proportional to the relative cross-sectional area of the reinforcement, assuming optimal impregnation. In 3D-printed LCPs, anisotropy arises not only from the alignment of molecules within individual extruded lines, but also from the directional nature of the deposited layers and their interfacial bonds [4]. Introducing pins into this system influences more than just the volume they occupy. Each pin alters the surrounding infill path, displacing deposition lines and disrupting local material flow beyond the cavity itself. These geometric interruptions influence the adhesion between neighboring lines. The time interval between adjacent depositions has been identified as a critical factor in determining bond strength, with increased delay leading to weaker adhesion [8]. For these reasons, it may be necessary to reconsider whether the pin infill metric should reflect only the pin volume or also encompass the additional influence zone around each pin.

The investigation into the actual extent of a pin's influence on a solid section, here referred to as the cavity-induced deviation, is carried out through a case study involving a rectangular section with a single round cavity. Figure 4.2 illustrates how different levels of manufacturing detail affect this deviation. Each of the three subfigures compares a top section without a cavity to a corresponding bottom section that includes one. Figure 4.2a focuses on the CAD model, where the cavity-induced deviation directly reflects the area ratio between the circular void and the entire section. In Figure 4.2b, a sliced view reveals printline characteristics through color-coding of perimeter and infill regions. Here, the presence of the cavity leads to an added inner perimeter, resulting in a broader cavity-induced deviation. Notably, this inner perimeter differs slightly from the CAD model in Figure 4.2a due to slicer corrections, as explained in Subsection 3.3.3, further accentuating the discrepancy. Finally, Figure 4.2c shows a predicted nozzle speed map using Klipper data, where a color gradient highlights how acceleration and deceleration influence effective print speed. The results indicate that while regions far from the cavity remain unaffected, areas closer to it show progressively more deviation, resembling a localized flow field.

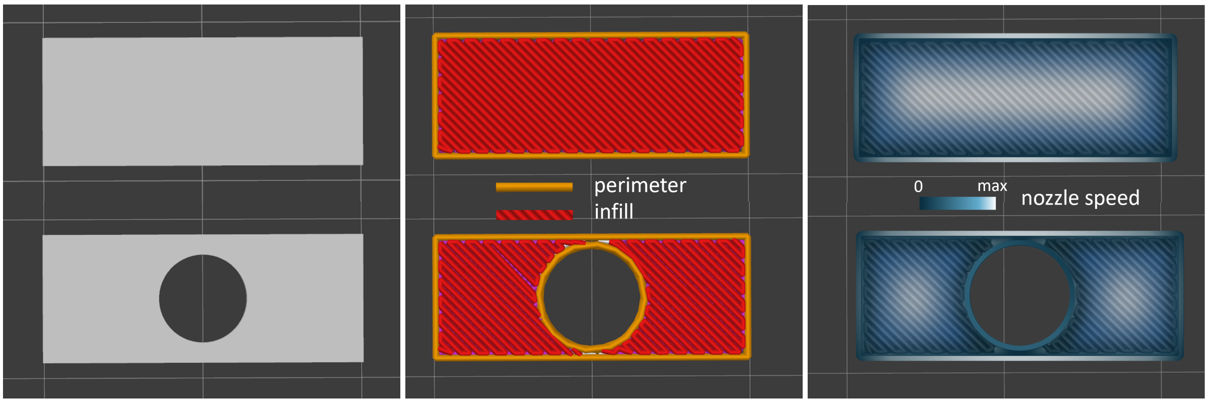

(a) Design geometry (b) Printing path (c) Printing speed

Figure 4.2: Influence of a pin cavity on the printing of a solid section. (a) CAD design showing a circular cavity in the lower half, (b) sliced layer highlighting perimeter and infill regions, (c) nozzle speed prediction based on Klipper simulation, showing local acceleration and deceleration around the cavity. [1]

The integration of these three perspectives on layer manufacturing highlights how the perceived impact of a pin cavity depends on the level of analysis. While the nozzle speed simulation provides the most detail, it also introduces additional complexity and requires interpretative assumptions. The sliced view provides insight beyond basic CAD geometry, but it still does not fully capture the cavity's influence. For this reason, the simplified geometric comparison (Figure 4.2a) will be used to define the pin infill parameter, whereas the deviations observed in Figure 4.2c will be taken into account during data interpretation.

4.1.2. Available design space

The determination of the number and size of pins to be placed within a cross-section must adhere to several criteria. These criteria pertain to the feasibility of manufacturing and the implications of the chosen z-pinning concept. To address the diverse nature of these criteria, a design space study, as illustrated in Figure 4.3, was conducted. This study is represented in four subfigures, each displaying an identical design space with the maximum pin diameter plotted on the horizontal axis and the number of pins on the vertical axis. The initial

---

[1] The figures were obtained using NematX slicer. The colour scheme in Figure 4.2c is a prediction based on own work.

three graphs (Figure 4.3a, Figure 4.3b, Figure 4.3c) delineate various constraints on the design space, whereas the fourth graph (Figure 4.3d) integrates all the preceding constraints. To facilitate analysis in two dimensions, we use the term "pin area fraction", the 2D analog of pin infill, which defines the fraction of the cross-sectional area occupied by pins. The complete 3D treatment of pin infill is addressed in Section 5.1. The section under consideration is a 4 mm x 10 mm rectangle. The origin of such constraint is explained in Section 5.1.

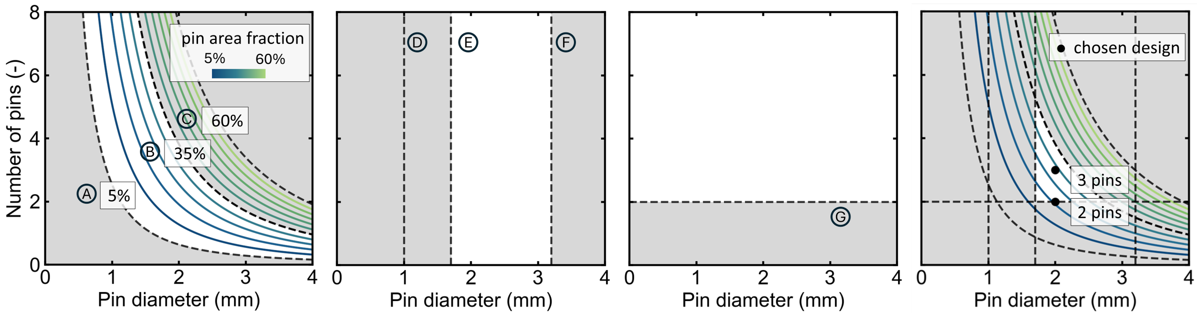

(a) Pin area fraction (b) Pin diameter (c) Pin column number (d) Intersection

Figure 4.3: Progressive restriction of the design space concerning pin number and diameter, culminating in the selection of two feasible pinning configurations. Each subfigure displays the same design space, with the pin diameter on the horizontal axis and the number of pins on the vertical axis. (a) Constraint from pin area fraction: A = minimum effective value (5%), B = maximum printable (35%), C = theoretical maximum (60%). (b) Constraint from nozzle geometry: D = nozzle tip diameter (1.0 mm), E = nozzle diameter at 2 mm depth (1.7 mm), F = max printable diameter (3.2 mm). (c) Constraint from minimum pin count: G = two-pin minimum required for staggered layout. (d) Final feasible region: intersection of all constraints; black dots indicate selected designs with 2 and 3 pins at 2 mm diameter.

The first step is to determine the range of feasible pin area fractions to consider. Figure 4.3a in Figure 4.3 plots curves of constant pin area fraction as a function of pin diameter and number of pins. Dashed black lines indicate feasible boundaries within the design space. A lower limit of 5% pin area fraction (point A in Figure 4.3a) is set based on prior work on 3D-printed Vectra® A950 [36], which showed that mechanical improvements below this level may be indistinguishable from noise. The upper bound requires more nuance. While a single circle inscribed in a rectangle can, in theory, occupy up to 80% of the area, practical limitations such as perimeter generation reduce this to approximately 60% (point C in Figure 4.3a). Furthermore, a minimum spacing between print lines, equivalent to at least one line width, is necessary to ensure proper load transfer between pins. This constraint reduces the maximum printable pin area fraction to roughly 35% (point B in Figure 4.3a). These curves assume consistent pin diameters across the cross-section. In practice, configurations involving wedging pins and staggering introduce varying pin heights and potentially lower area fractions (see Subsection 5.1.2). This assumption facilitates the process of defining the design space and, by being conservative, is deemed suitable for this analysis.

The diameter of the pin cavity is constrained by both the part cross-section and the nozzle geometry. The maximum circular cavity must fit within the 4 mm side while allowing sufficient clearance for both internal and external perimeters. This clearance depends on the selected linewidth and the slicer's "XY hole compensation parameter" (see Subsection 3.3.3). With a linewidth of 0.2 mm and the tuned compensation value (Appendix A), the maximum printable pin diameter is 3.2 mm (point F in Figure 4.3b). The minimum pin diameter is defined by the nozzle's external taper (see Subsection 3.3.1), which must enter the cavity to extrude pins from the bottom up. At the tip, the nozzle's outer diameter is 1.0 mm (point D), but at a depth of 2 mm, it increases to 1.7 mm (point E), placing a geometric limit on cavity width. A cavity depth of 2 mm was chosen based on design space iterations: deeper cavities would restrict feasible pin configurations due to the nozzle's expanding taper, making it difficult to fit more than two pins within the cross-section.

In a cross-section, there should be at least two pins because of their discrete nature. A single column of pins might fail to enhance mechanical performance or could even decrease it, as pins don't transfer loads through the interface with those above or below. A minimum of two pin columns allows for staggered placement (G in Figure 4.3c). The overlapping feasible design spaces outlined form a range of numbers and diameters. This interval is depicted in Figure 4.3d. While this design space stretches vertically, the number of pins must be a whole number. Among the possible diameters, selecting round numbers is preferable for simplicity. The black dots highlight the design points considered most promising for future research stages. Choosing a design with four pins would offer the most significant potential quantity of pins. However, initial pinning trials indicated a frequency of nozzle collisions with the part that was too high for reliable prints. The selected design points are three-pin and two-pin configurations, each with a maximum pin diameter of 2 mm. Utilizing the same diameter allows for easier comparative analysis of the designs based on pin count, and indirectly, the pin area fraction. The pin's maximum diameter defines the height limit used in the following design phase.

4.1.3. Pin geometry

The specifications of the pin geometry are contingent upon the general pin profile and the maximum permissible dimensions. The fundamental concept of the pin shape is analyzed in Subsection 3.2.3, whereas the explicit maximum dimensions are established in Subsection 4.1.2. Consequently, the precise dimensions of the pins can be delineated. The four key dimensions that characterize the morphology of the wedging pin are depicted in Figure 4.4a, which include the pin's maximum diameter, minimum diameter, cone height (h_{cone}), and the height of the cylindrical body ($h_{cylinder}$). The overall pin height ($h_{pin} = 2h_{cone} + h_{cylinder}$) is the most pertinent parameter for investigation due to its association with strength enhancements [30, 38].

To study the influence of a single geometric parameter through parametric analysis, at least three pin designs were created. Either the cone segment height (h_{cone}) or the cylindrical segment height ($h_{cylinder}$) could be varied, with the latter chosen for one key reason: increasing $h_{cylinder}$ produces longer pins associated with lower pin volume. Since preliminary tests indicated that failure did not occur within the pin itself, the chosen diameters were deemed sufficient. Reducing pin volume also minimizes the cavity-induced deviation, as demonstrated in Figure 4.4. Notably, the requirement for a relatively large top diameter stems from nozzle geometry, not from a mechanical preference. Once the cone is wide enough to allow full nozzle submersion, reducing the material below it becomes desirable. While an asymmetric pin, narrower at the base, could further reduce volume, such designs introduce additional complexity and are left for future work. The final design variations differ only in $h_{cylinder}$, shown in Figure 4.4b, Figure 4.4c, and Figure 4.4d for the short, medium, and tall pins, respectively.

The height of the cone sections was established through iterative testing to assess the manufacturability limits imposed by the overhang of the lower cone. These trials resulted in a viable h_{cone} of 0.4 mm. Once fixed, this value defined the portion of the pin that could be allocated to the cylindrical section. To obtain a meaningful parametric variation while remaining within the total height constraint, this remaining height was evenly divided into increments of 0.6 mm, yielding three configurations: a short pin with no cylindrical segment, a medium pin with $h_{cylinder}$ = 0.6 mm, and a tall pin with $h_{cylinder}$ = 1.2 mm. The selected step size strikes a balance between producing distinguishable pin geometries and maintaining feasible printability. The minimum diameter was set to 1.4 mm, as this was the smallest dimension that allowed the nozzle to reach the base of the tallest pin reliably. A summary of the common geometric features is presented in Figure 4.4a. With the pin designs finalized, the following step focuses on their manufacturability.

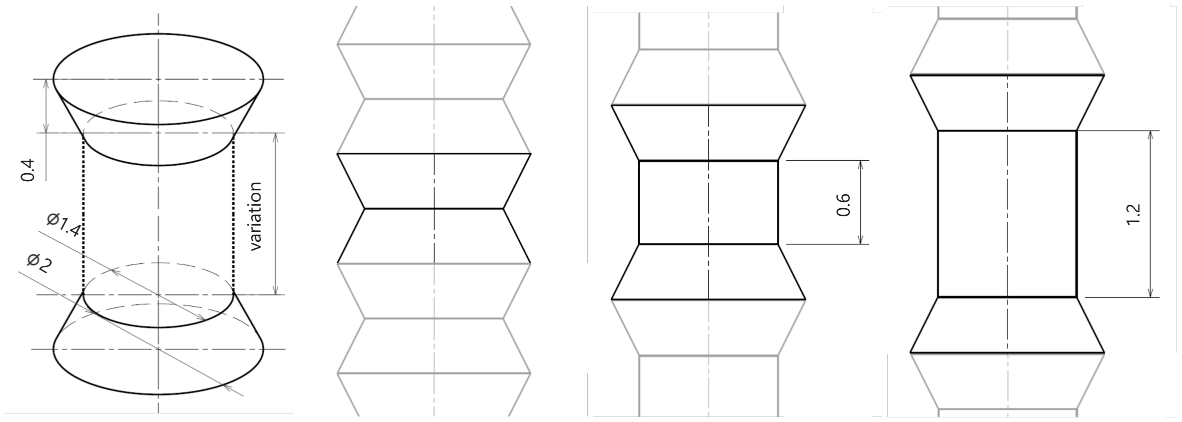

(a) Shared dimensions (b) Short pin (c) Medium pin (d) Tall pin

Figure 4.4: Geometrical definition of the three pin designs. (a) Isometric view showing the shared dimensions across all samples. (b) Short pin with no cylindrical section. (c) Medium pin with a 0.6 mm cylindrical segment. (d) Tall pin with a 1.2 mm cylindrical segment.

4.2. Extrusion routine

An extrusion routine comprises the set of G-code commands responsible for executing the extrusion of a pin. In the existing literature, all pinning methodologies are top-down, and the extrusion routines have not been sufficiently complex to warrant interest [2, 10–15, 30, 31]. When employing a bottom-up pinning strategy and geometries more complex than cylinders, it becomes imperative to accurately control the material extrusion at specific locations along the pin height by developing an extrusion routine. The subsection is divided into three parts. begins by explaining why creating a pinning routine is important and discusses the issue of print delay. Next, clarifies how incrementally adding extrusion modifiers can enhance control over extrusion, ultimately achieving the target pinning quality. Finally, examines the extrusion routine used, highlighting its drawbacks and the impact of the G-code commands on the phases of pin extrusion.

4.2.1. Relevance of an extrusion routine

The importance of investing in a complex extrusion process became clear after the initial mechanical assessments. Simple extrusion routines were not sufficient to ensure the desired pin quality. Pin quality is characterized by the degree to which the printed material conforms to the specified design geometry. Figure 4.5 showcases three examples of incomplete pin formation. Poorly formed pins result in reduced mechanical performance, as indicated by the presence of smooth fracture surfaces. When a fracture surface aligns with the boundary between two layers, it suggests a lack of toughening mechanisms, like layer bridging [10]. In Figure 4.5a, there is a noticeable looseness in the cylindrical section, along with an incomplete cone formation. Figure 4.5b highlights the failure of the pin's cylindrical part, revealing again incomplete filling of the cylindrical section. Lastly, Figure 4.5c shows cones with irregular shapes, deviating from the theoretical design and leading to pullout failure. Forming both pin cones in their entirety is vital, as they are the only pin feature responsible for load transfer.

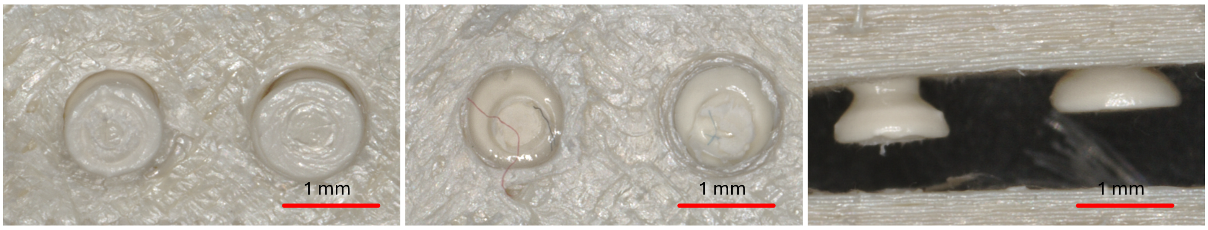

(a) Loose pin (b) Incomplete cylindrical section (c) Incomplete cone section

Figure 4.5: Examples of incomplete pin formation from preliminary testing. (a) Shows a fracture surface with a loose pin due to insufficient filling of the cavity. (b) Highlights the incomplete formation of the pin cylindrical section, causing fastener failure. (c) Displays irregular cone sections, deviating from the intended geometry; the compromised mechanical interlocking results in pullout failure.

The failure of simple extrusion routines to deposit material at the pin's base revealed that extrusion was not occurring from the intended starting point. To improve pin quality, the extrusion process was refined through empirical testing. These issues are rooted in a well-known phenomenon in fused filament fabrication (FFF) [2, 8] and it is known to affect Vectra® A950 [34, 37]. Due to the filament's viscoelastic nature, pressure buildup and relaxation inside the nozzle lag behind changes in commanded extrusion rate. This mismatch between nozzle motion and actual material flow, known as extrusion delay, can severely affect print quality. In response, a feature called pressure advance was introduced in slicers and firmware to compensate for this delay. Figure 4.6 illustrates the concept: Figure 4.6a compares ideal and real extrusion profiles, showing how acceleration and deceleration result in a trapezoidal extrusion pattern, even when G-code commands specify instant speed changes. Figure 4.6b shows how pressure advance corrects for this, briefly overshooting the target rate to stabilize the extrusion more rapidly. [2] Since extrusion delay is highly sensitive to print parameters such as temperature, speed, nozzle diameter, line width, and layer height, it remains difficult to model analytically. As a result, pressure advance must be tuned experimentally for each printer setup. In this work, the Klipper firmware was used to compensate for pressure lag. While Klipper's default tuning effectively improved the consistency of regular print lines, pin extrusion, due to its higher flow rates, fell outside the optimal tuning envelope. To address this, a new strategy was developed: combining custom extrusion modifiers to create a tailored pinning routine. This approach mimics the function of slicer-integrated pressure advance, but with fine-tuned control specific to the pin geometry. The resulting method successfully overcame the delay and enabled reliable extrusion at the base of the pin.

---

[2] `https://www.klipper3d.org/Pressure_Advance.html`

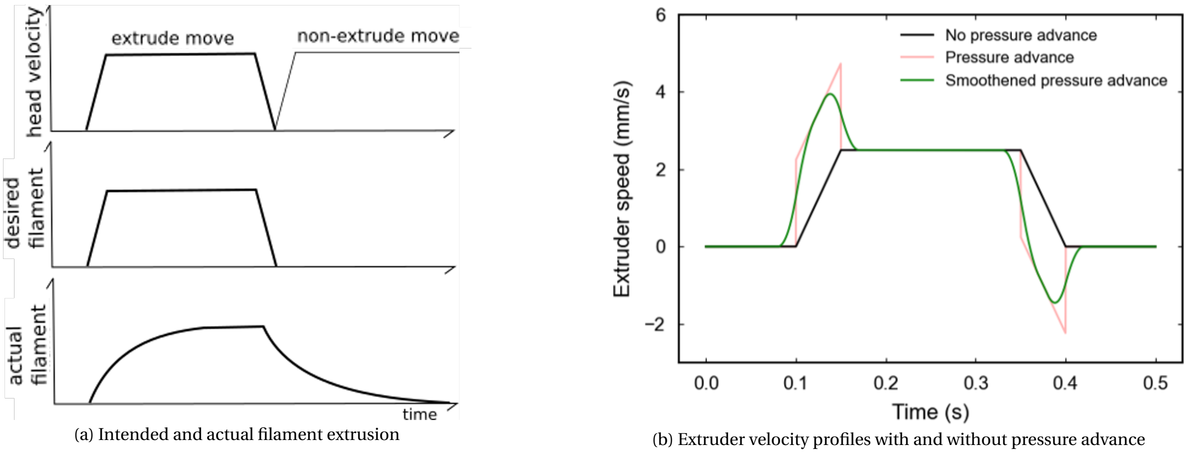

(a) Intended and actual filament extrusion

(b) Extruder velocity profiles with and without pressure advance

Figure 4.6: Illustration of extrusion delay in FFF printing and its compensation through Klipper's pressure advance feature. (a) Comparison between intended and actual filament extrusion profiles during acceleration and deceleration, highlighting the lag caused by pressure buildup and relaxation. (b) Extruder velocity profiles with and without pressure advance, showing how Klipper adjusts the extrusion rate to synchronize material flow with nozzle motion. [3]

4.2.2. Contribution of the extrusion modifiers

A set of six extrusion modifiers was developed to refine the extrusion profile for improved pin quality: volume-normalized extrusion, front-loading, extrusion multiplier, nozzle pre-depression, localized speeding, and pre-pressure. The first five were combined in the final extrusion routine; the sixth was tested during development but ultimately excluded from the final product. This subsection focuses on the cumulative effect of the adopted modifiers. For a parameter-by-parameter breakdown, see Appendix B. Figure 4.7 illustrates the transition from constant extrusion to the implementation of the first two modifiers. Each subplot shows identical data: Figure 4.7a plots individual extrusion commands versus pin height, while Figure 4.7b shows cumulative extrusion. In parallel, Figure A.3 presents microscope images of pin cross-sections corresponding to each modifier step. Notably, the simplest extrusion routine in Figure 4.8a closely resembles LCP pins reported in literature (see Figure 2.10). All modifier values reflect those used in the final adopted routine, demonstrating progressive improvement across the extrusion strategy.

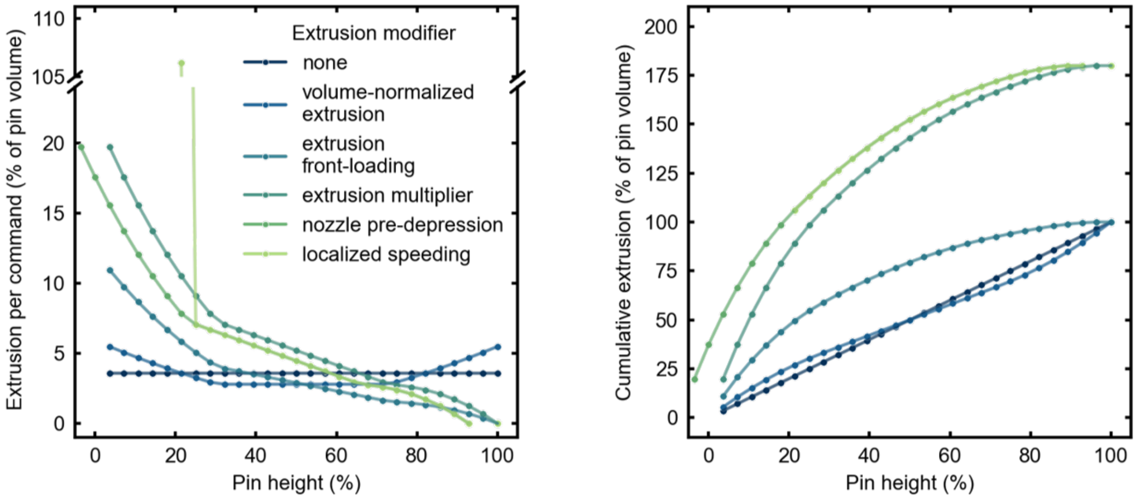

(a) Individual extrusion commands

(b) Cumulative extrusion

Figure 4.7: Effect of extrusion modifiers on extrusion profile shaping. Both subplots show the same data for a single pin: (a) plots the extrusion per command as a function of pin height; (b) shows the corresponding cumulative extrusion. The routines compared include a baseline with no modifiers and two modified versions incorporating volume-normalized extrusion and front-loading. The legend is the same for both subplots

---

[3] Subfigure (a) is taken from `https://www.klipper3d.org/Kinematics.html` while subfigure (b) was produced using code from `https://github.com/Klipper3d/klipper/blob/master/scripts/graph_extruder.py`

The first modifier, volume-normalized extrusion, scales extrusion by the volume of the cavity section traversed at each step. As shown in Figure 4.7a, this introduces an oscillating profile that mirrors the pin's geometry (Figure 4.4), but it has minimal impact on forming the cylindrical segment or the bottom cone, as seen in the transition from Figure 4.8a to Figure 4.8b. To compensate for extrusion delay, front-loading shifts material deposition to an earlier stage of the move. This shift visibly improves pin quality (Figure 4.8c), though the bottom cone remains underfilled. As shown in Figure 4.7b, this strategy anticipates the ramp-up delay in extrusion speed (see Figure 4.6). However, since the extruder is still accelerating during most of the pin formation, the actual output lags. To counter this, the extrusion multiplier increases total extruded volume relative to the cavity volume. This increased volume improves deposition rate, but yields only modest results (Figure 4.8d). At the base of the pin, extrusion speed remains nearly zero, so pressure doesn't build up in time. The nozzle pre-depression modifier addresses this by lowering the nozzle to contact the cavity bottom before starting extrusion, allowing time for pressure to ramp up. The effect is visible in Figure 4.8e. The final improvement, localized speeding, targets the bottom cone region. By locally increasing the feed rate, this modifier boosts extrusion just as the nozzle exits the critical cone section. Its effectiveness depends on the pressure buildup achieved via nozzle pre-depression, ultimately resulting in complete pin formation, as shown in Figure 4.8f.

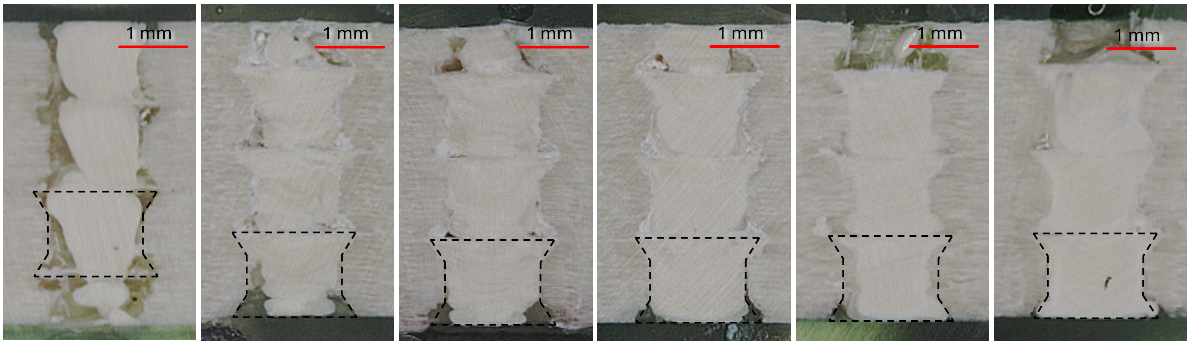

(a) none (b) geo. distribution (c) height-based skew (d) increased volume (e) shift height (f) cone blob

Figure 4.8: Progressive improvement of pin formation through extrusion modifiers. The section views of printed pins show the effect of sequentially introducing extrusion modifiers. Each subfigure (a–f) corresponds to the final modifier introduced at that stage, as labeled below each image.

Observation of Figure A.3 confirms that the main challenge in pin formation lies in achieving complete extrusion of the bottom cone. The quality attained in the final extrusion routine is mainly due to carefully shaping the extrusion rate throughout the print. A deeper understanding of the printhead's effective kinematics would enable plotting the extrusion rate as a function of time rather than height. This shift in perspective, from spatial to temporal, would help the direct application of literature models and experimental data for pressure buildup, allowing modifier values to be tuned analytically rather than through iterative trial and error.

4.2.3. Structure of the extrusion routine adopted

The extrusion procedure used in this study ensures the formation of pins capable of mechanically interlocking with the surrounding infill. Figure 4.9 shows the final extrusion profile derived from the modifier-based development described earlier. This routine was used for the pinning of all parts referenced in Chapter 5, and the exact modifier values are detailed in Appendix B. This subsection explores the pinning routine by analyzing: the extrusion sequence (Figure 4.9) and the progression of pin formation (Figure 4.10). Across all figures, the main geometric sections of the pin, bottom cone, cylinder, and top cone are marked as stages 1, 2, and 3, respectively. Stage 0 refers to the pre-extrusion state (Figure 4.10a, while stage 4 represents the post-extrusion wipe and its effect in Figure 4.10e.

Extruding more material than the cavity can contain inevitably leads to overflow. This surplus causes various issues: it can block adjacent cavities, trap material between layers (reducing adhesion), deform geometry, and lead to material accumulating on the nozzle. Such buildup increases the risk of print failure due to part detachment and results in material waste that must be removed through post-processing. Moreover, even when the nominal extrusion volume matches the cavity volume, overflow may still occur due to geometric deviations in the printed cavity. Attempts to minimize overflow by fine-tuning modifier values proved ineffective. As wiping is already integrated into each pinning cycle (Figure 4.10e), the use of a slightly overfilled cavity is accepted as a trade-off to ensure full pin formation, despite the resulting material loss.

The extrusion profile begins with a strong command and gradually decreases until reaching zero as the nozzle ascends. In Figure 4.9a, the first command, coinciding with the nozzle reaching the base of the cavity (stage 1), already specifies more volume than the cavity can contain. This large command leads to a slight overflow, visible in Figure 4.10b. Consequently, the bottom cone appears fully formed at this point, with some material visibly displaced around the nozzle. During stage 2, the cylindrical section is formed through a series of steadily decreasing commands. Overflow continues during this stage, as evident in Figure 4.10c. Finally, in stage 3, the top cone is printed. Even though extrusion commands fall to zero before reaching the final height, the top cone is visibly formed (Figure 4.10c), and further material accumulation is seen above the cavity (Figure 4.10d).

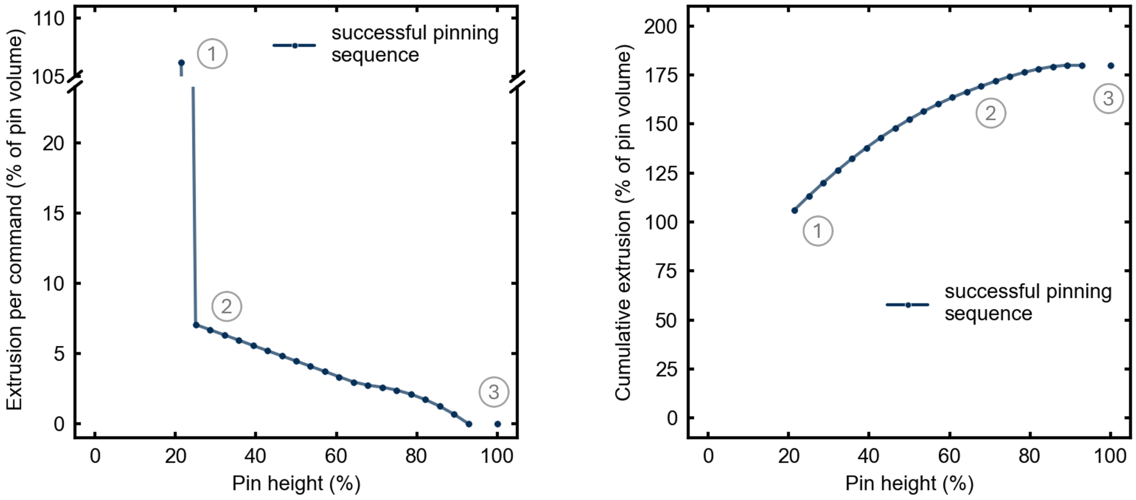

(a) Individual extrusion commands

(b) Cumulative extrusion

Figure 4.9: Extrusion profile used for successful pinning. Both plots represent the same data from the adopted routine: (a) shows individual extrusion commands as a function of normalized pin height; (b) presents the corresponding cumulative extrusion. The extrusion sequence is annotated with numbers 1–3, indicating the formation of the pin's bottom cone, cylindrical section, and top cone, respectively.

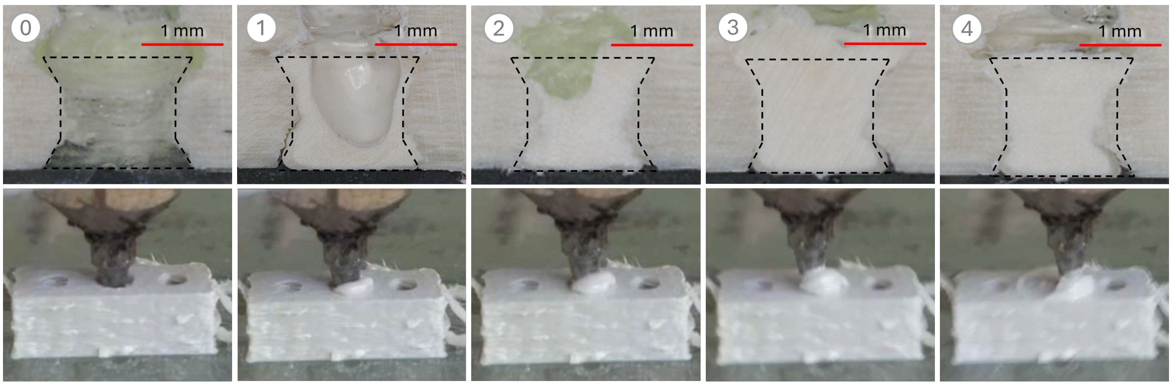

(a) Pre-extrusion

(b) Bottom cone

(c) Cylinder

(d) Top cone

(e) Wipe

Figure 4.10: Progressive extrusion stages of a pin using the adopted extrusion routine. Each column shows both the cross-sectional view (top) and nozzle perspective (bottom) at key stages of the process: (a) pre-extrusion, (b) bottom cone formation, (c) cylinder formation, (d) top cone formation, and (e) post-extrusion wipe. The images highlight how the pin geometry is progressively formed and how material overflow evolves throughout the routine.

The extrusion modifiers comprise a combination of constants and shape- or configuration-dependent functions. All routine development and microscopy imaging presented in this section were performed using the medium pin design shown in Figure 4.4. Once optimized, the same routine was applied to the short and tall pin designs to assess its generalizability. Figure 4.11 compares pin quality across all three designs: short pins (Figure 4.11a), the baseline medium pins (Figure 4.11b), and tall pins (Figure 4.11c). This extrusion routine produced the highest overall quality observed. Defects, such as trapped air bubbles, appear in both Figure 4.11b and Figure 4.11c, but further fine-tuning to eliminate them was deferred in favor of evaluating the mechanical performance of the pins. Although improvements are still possible, only mechanical testing will determine whether these imperfections have a significant influence on failure behavior. Notably, the cone sections are consistently well-formed across all designs, which is the primary target of the extrusion routine optimization.

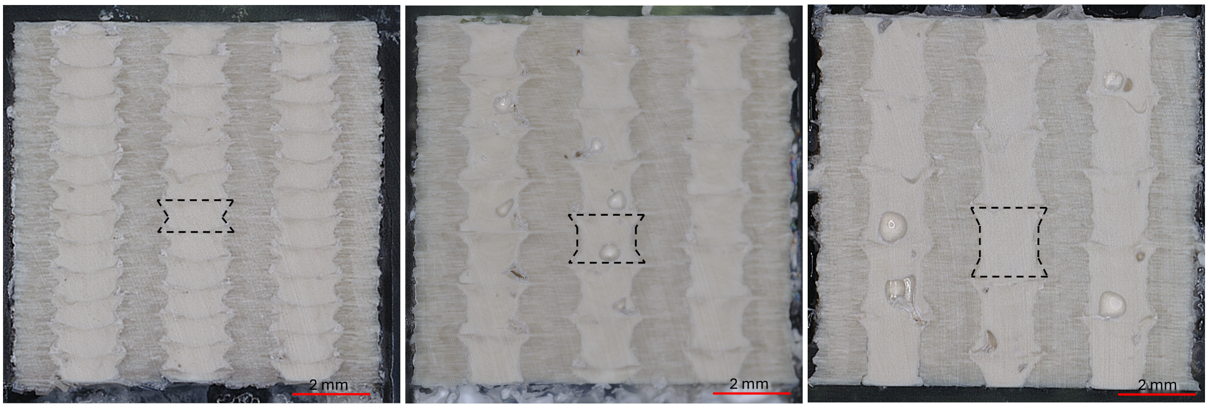

(a) Short pin (b) Medium pin (c) Tall pin

Figure 4.11: Pinning quality comparison across three pin geometries using the adopted extrusion routine. (a) Section printed with short pins, (b) section optimized with medium pins, and (c) section using tall pins. Each image includes a black overlay of the intended pin geometry for visual reference.

4.3. Chapter summary

This chapter describes the determination of three pin geometries and the extrusion routine required to ensure the desired pin formation despite the challenges posed by 3D printing Vectra® A950 filament. The objective was to define the design parameters of the pins and to implement a corresponding extrusion process capable of producing them within dimensional tolerances.

The first section focused on specifying the three-pin geometries. The pin infill was introduced as the ratio between the volume occupied by pins and the total solid volume of the part, in analogy to fiber volume fraction in composite materials. This parameter was identified as one of the main design variables due to its expected influence on mechanical properties and material usage. The design space was created by determining various combinations of pin diameter and pin count, limited by the specimen's cross-sectional area, the requirement for a minimum of two pin columns, and manufacturing constraints. The analysis on the design space allowed a structured selection of pin layouts suitable for mechanical testing. Pin height was introduced as a design variable. Heights were discretized into short, medium, and tall categories to assess the influence of vertical extent on mechanical interlocking and stress transfer between layers. The combination of these parameters defined a set of discrete pin configurations for subsequent evaluation.

The second section addressed the generation of G-code commands to extrude the pin geometries introduced in the previous section. Initial attempts using basic routines resulted in inconsistent pin formation and geometric defects. Irregular deposition and voids compromised the correspondence between designed and printed geometry. To address this, extrusion modifiers were added sequentially. The final extrusion process utilizes the simultaneous application of six extrusion modifiers, yielding a pin quality suitable for mechanical interlocking. While this approach increased the complexity of the G-code, it improved control over material placement. The impact of the routine was evaluated qualitatively based on dimensional accuracy and observed consistency during printing.

5

Printing parts and evaluating their mechanical performance

Tensile testing was employed to assess the effectiveness of pinning in enhancing the strength of 3D-printed components. The previous chapter defined the pin geometries and established a consistent G-code routine for their deposition within cavities. This chapter is divided into two sections: Section 5.1 outlines the procedures used to manufacture the test specimens. In contrast, Section 5.2 presents the mechanical test results and identifies which pin configurations yielded the most significant performance gains. Tensile dogbone specimens are widely adopted in the literature to assess interlaminar reinforcement in 3D printing [22, 41–44]. Although some studies investigate properties such as fracture toughness, shear, bending, or compression strength [7, 15, 22], this work focuses on tensile strength due to its lower execution complexity. Notable fracture behaviors are also considered. Future studies may extend to toughness characterization, provided that improvements in tensile strength are confirmed.

5.1. Printing pinned parts for mechanical testing

This section outlines the process used to manufacture test specimens with various pin configurations in preparation for mechanical testing. Producing full-scale specimens adds complexity to the development of Chapter 4. Pin column alignment becomes critical at this scale, and printing slender parts from LCP introduces additional challenges due to poor layer and bed adhesion. To address these issues, Subsection 5.1.1 describes the selected test geometry and the rationale behind it. The choice of pin staggering order and its implications are presented in Subsection 5.1.2. All tested specimen configurations are reviewed in Subsection 5.1.3, highlighting the differences in pin layouts. Finally, Subsection 5.1.4 discusses the manufacturing process, including print-related challenges, and concludes with a brief cost analysis.

5.1.1. Test specimen design and pin cavity placement

The tensile specimen used in this study is based on the geometry employed in prior work investigating the interlayer strength of Vectra® A950 [36]. The key dimensions of the dogbone specimen are shown in Figure 5.1a, while Figure 5.1b illustrates the location of the pin cavities. The whole pin layout is discussed later in Subsection 5.1.3. This specimen was selected due to its demonstrated printability with LCP on a different printer platform. Printability is a critical consideration, as Vectra® A950 is known for its sensitivity to process conditions. Compared to ISO-standard geometries [45], the selected design has a lower aspect ratio, simplifies the printing, and reduces material use. However, since the results in [36] were obtained with a different printer and slicing setup, direct comparison is not viable. For this reason, unpinned control specimens were reprinted to serve as a baseline. As described in Subsection 4.1.2, the gauge cross-sectional area (black rectangle in the A-A view of Figure 5.1a) dictated the choice of number and diameter of pins.

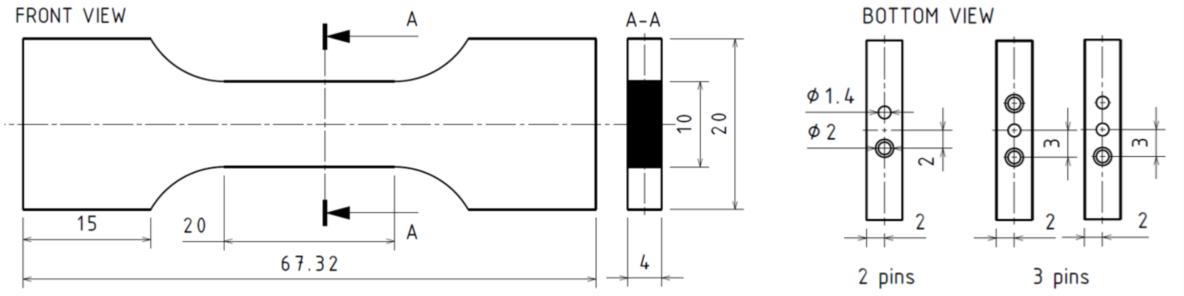

(a) Test specimen dimensions

(b) Pin cavity placement

Figure 5.1: Tensile specimen geometry and pin cavity location. (a) shows the main dimensions of the dogbone specimen, (b) highlights the placement of the pin cavities within the cross-section. [1]

5.1.2. Staggering orders of pin columns

The spatial arrangement of multiple pins within a part offers design flexibility and opportunities for mechanical optimization. Some constraints originate from the z-pinning concept established in Chapter 4. To simplify manufacturing, pins are stacked into vertical columns, such that each pin aligns directly above and below another. Additional constraints derive from the selected pin geometries, as defined in Figure 4.3, where only two configurations were used: 2 or 3 pins per cross-section, each with equal diameter. The layout of pin cavities was designed to distribute pins homogeneously within the gauge cross-section, as shown in Figure 5.1b. The only remaining degree of freedom was the vertical offset between pin columns, referred to as the staggering order [12].

In the 2-pin configuration, there is only one possible arrangement: a half-length vertical offset between columns, commonly denoted as AB [12]. For the 3-pin configuration, two arrangements are possible: ABA and ABC. In ABA, the outer columns (A) are aligned while half a pin height offsets the center column (B). In ABC, each column is vertically offset by one-third of a pin's length. These configurations are compared in Figure 5.2, with Figure 5.2c specifically illustrating their relative offsets. In both cases, the offset defines the vertical distance between pin-column discontinuities, a parameter expected to influence crack propagation resistance. A larger vertical separation is hypothesized to deflect or arrest advancing cracks more effectively by forcing the crack along a more tortuous crack path.

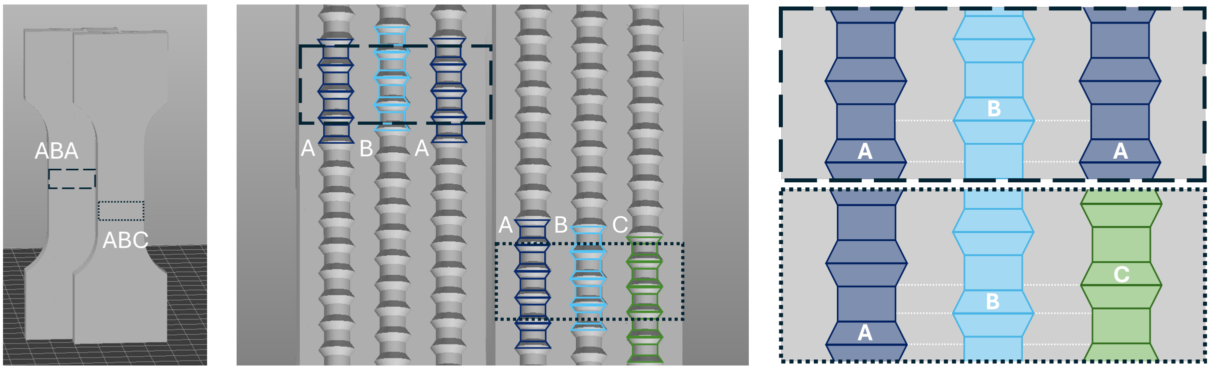

(a) Full specimens

(b) Exposed pin cavities with different staggering orders

(c) ABA and ABC staggering orders

Figure 5.2: Pin staggering orders on full-size parts. (a) shows the full tensile specimens, (b) displays the exposed pin cavities for staggering strategies ABA and ABC, and (c) highlights the interval between the pin-column discontinuities with white dashed lines. [2]

The portion of a specimen's cross-section printed with regular layer infill—referred to as the layer-infill-section—varies in size and shape along the part's height. This variation is inherent to pin designs with changing diameters and is influenced by the vertical staggering order of the pins. Figure 5.3 illustrates this effect using the ABA staggering configuration. Figure 5.3a identifies two cross-sectional planes within the gauge area, and Figure 5.3b

---

[1] The dimensions of the tensile dogbone were provided by NematX. The CAD file of the specimen used can be found at `https://github.com/LorenzoOnorato/z_pinning_fff_research` with the name of "dogbone_virgin". The images were drafted using 3DX

[2] The images in subfigures (a) and (b) were obtained using NematX slicer.

shows how their layer-infill-sections differ due to the local pin geometry at each height. Large variations in the layer-infill-section are undesirable, as they increase stress concentrations. In the ABA staggering order, two columns contain simultaneous vertical gaps. The presence of multiple pin-column discontinuities in the same layer concentrates the load on a smaller area, increasing stress around the pins and favoring crack initiation. While this arrangement may offer benefits in terms of crack propagation resistance, it is less favorable than ABC for preventing crack initiation. Figure 5.3c compares the smallest and largest layer-infill-sections observed in the ABA configuration.

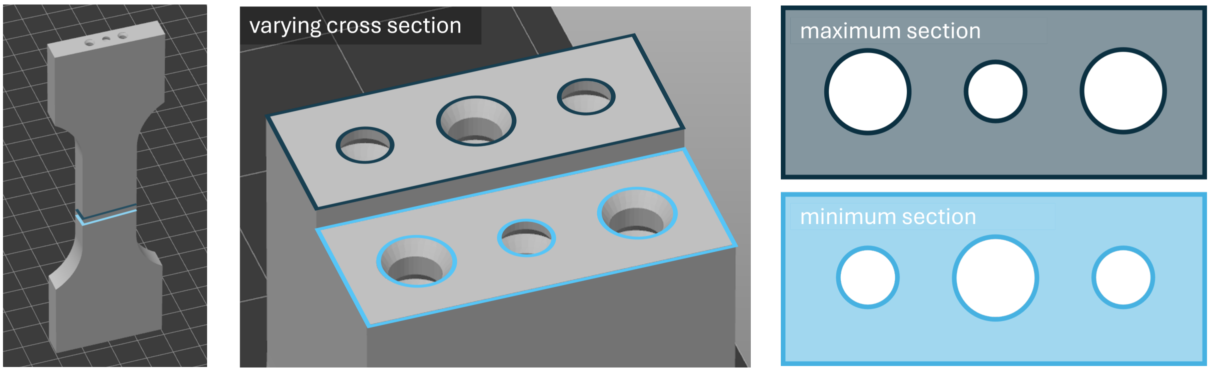

(a) Full specimen

(b) Layer-infill-section varying with height

(c) Maximum and minimum layer-infill-sections

Figure 5.3: Varying layer-infill-section in a specimen with ABA pin staggering order. (a) shows the full-size dogbone and highlights two cross-sectional planes in the gauge area;(b) displays the layer-infill-section at those two heights; (c) compares the maximum and minimum cross-sections. [3]

5.1.3. Overview of pin configurations for testing

The tested pinning configurations result from the combination of two design variables: pin staggering order and pin height. This subsection summarizes all the manufactured and tested configurations, as shown in Figure 5.4. A control specimen with regular solid infill was also printed for reference. An internal reference is necessary, as the mechanical properties of printed Vectra® A950 are susceptible to printing parameters [4].

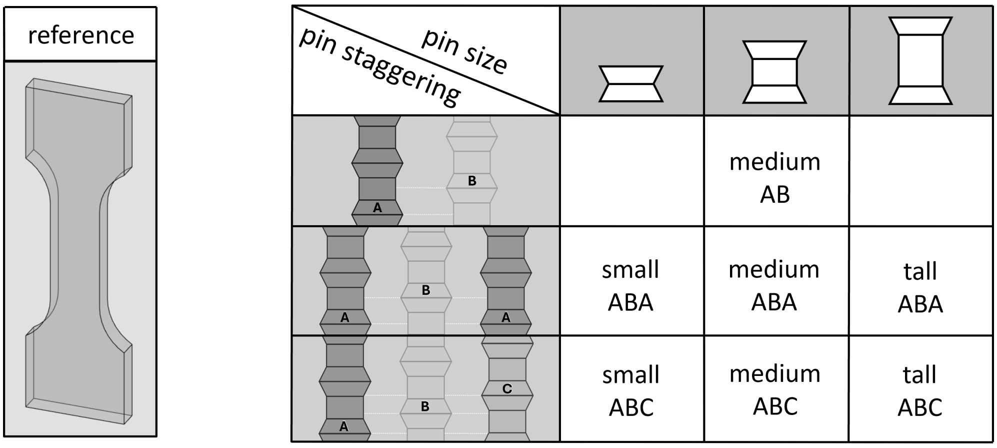

Figure 5.4: Summary of tensile specimens and pin configurations tested. (a) shows the reference specimen, printed with regular solid infill. (b) presents the matrix of pinned specimens, organized by staggering order and pin height. Each cell represents a unique configuration.

The matrix of pin configurations is organized in Figure 5.4, with staggering order along one axis (AB, ABA, ABC, as introduced in Subsection 5.1.2) and pin height along the other (short, medium, tall, described in Subsection 4.1.3). Each row-column intersection represents a unique configuration that was produced and tested. These configurations differ not only in geometry but also in key structural metrics: pin infill, distance between discontinuities, and minimum layer-infill-section. Their values are presented in Table 5.1. Pin infill, introduced in Subsection 4.1.1, quantifies the volume occupied by pins in the gauge section and reflects how much they disrupt the regular infill; lower values are preferable. The distance between discontinuities and the

---

[3] The images in subfigures (a) and (b) were obtained using NematX slicer.

minimum layer-infill-section, previously discussed in Subsection 5.1.2, are indicators of structural continuity: larger values for both are beneficial, as they are associated with delayed crack propagation and reduced risk of crack initiation.

Table 5.1: Pin design analytics for all tested pin configurations. The full definitions of the dimensions are provided in the footnotes.

Pin design	**Staggering order**	**Pin infill** [1] (%)	**Distance between pin-column discontinuities** [2] **(mm)**	**Minimum layer-infill-area** [3] **(%)**
short	ABA	17.2	4.0	78.6
	ABC	17.2	2.7	82.6
medium	AB	9.9	7.0	88.3
	ABA	14.8	7.0	80.4
	ABC	14.8	4.0	84.4
tall	ABA	13.8	10.0	80.4
	ABC	13.8	6.6	84.4

[1] Pin infill is calculated for the gauge section, as this is the region where failure occurs and mechanical properties are evaluated.
[2] Vertical distance between pin-column discontinuities.
[3] Minimum fraction of gauge section cross-sectional area occupied by layer infill.

5.1.4. Manufacturing of test specimens

Manufacturing full-scale tensile specimens posed greater challenges than printing the smaller parts discussed in Figure 4.11. These challenges fell into three categories: completing the print, achieving adequate part quality, and minimizing post-processing effort. Notably, the pinned specimens did not encounter printability issues; all print failures were associated with the reference specimens using standard solid infill. Addressing these issues was critical to ensuring that any observed differences in mechanical performance could be attributed to pinning rather than inconsistencies in print quality. Once optimal parameters for printing the reference specimens were established, the pinned variants were printed using the same settings to allow for a fair comparison.

Definition of printing parameters

Printing tall, slender structures is a well-known challenge for FFF. The pressure applied by the nozzle during deposition introduces a bending moment, which increases as the height-to-base ratio grows. In extreme cases, this can cause parts to detach or fracture during the printing process. The tensile specimen used here has a particularly slender geometry; its height is roughly three times its second largest dimension and 16 times its smallest (see Figure 5.1), making it susceptible to delamination, especially with traditional infill. Previous work with the same Vectra® A950 material recommended printing specimens in 2×2 batches to encourage the formation of connecting stringing lines [36]. These lines serve to mechanically unify the specimens into a single structure with a broader base, improving stability during printing. The printing strategy began with this approach (Figure 5.5a) and evolved through two refinements (Figure 5.5b and Figure 5.5c) as issues arose and were addressed.

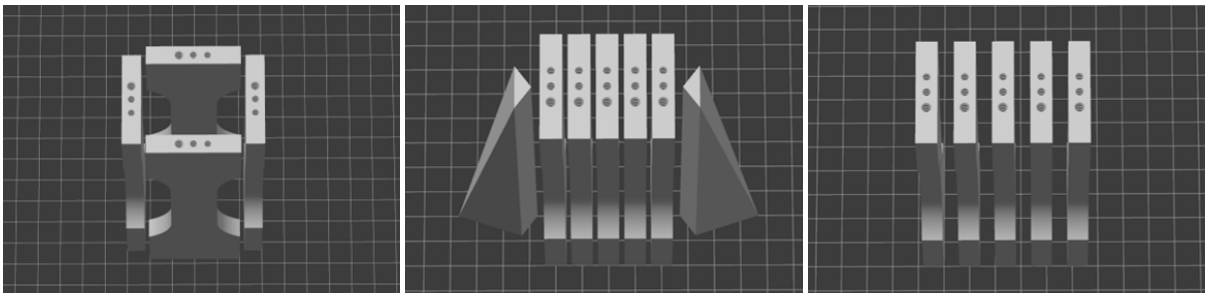
(a) Initial arrangement (b) Improved arrangement (c) Final arrangement

Figure 5.5: Arrangement of test specimens on print bed. (a) shows the initial square configuration, (b) introduces edge supports to reduce detachment risk, and (c) represents the final arrangement with increased spacing, larger brims, and no supports. [4]

---

[4] The images were obtained using NematX Slicer.

Although the initial square configuration allowed full prints, the stringing lines it produced caused issues during part removal, often tearing specimens due to delamination (Figure 5.6a). In some cases, the batch even detached from the build plate. These failures raised concerns about the control of nozzle temperature. Investigation revealed that the nozzle tip cooled significantly, up to 20°C below the heat block temperature, due to its narrow profile. This discovery prompted an increase in nozzle temperature, as well as a higher bed temperature. Further improvements included reducing the layer height to 0.05 mm to enhance adhesion and mitigate delamination, although this increased print time and necessitated manual tuning at the start of printing. [5] The arrangement shown in Figure 5.5b allowed for tighter spacing and incorporated custom disposable supports. However, these supports trapped over-extruded material between specimens, again complicating post-processing. Once extrusion parameters were refined, stringing lines were no longer beneficial and became a post-processing burden. The supports also increased layer time without improving print stability (Figure 5.6b). The final arrangement (Figure 5.5c) removed supports, increased spacing between specimens, enlarged the brim, and introduced seam alignment and increased retraction to reduce stringing. As shown in Figure 5.6c, this setup yielded fewer, sparser stringing lines. Overall, the printing challenges revealed that temperature control and extrusion settings had a much greater impact on print success than batch layout.

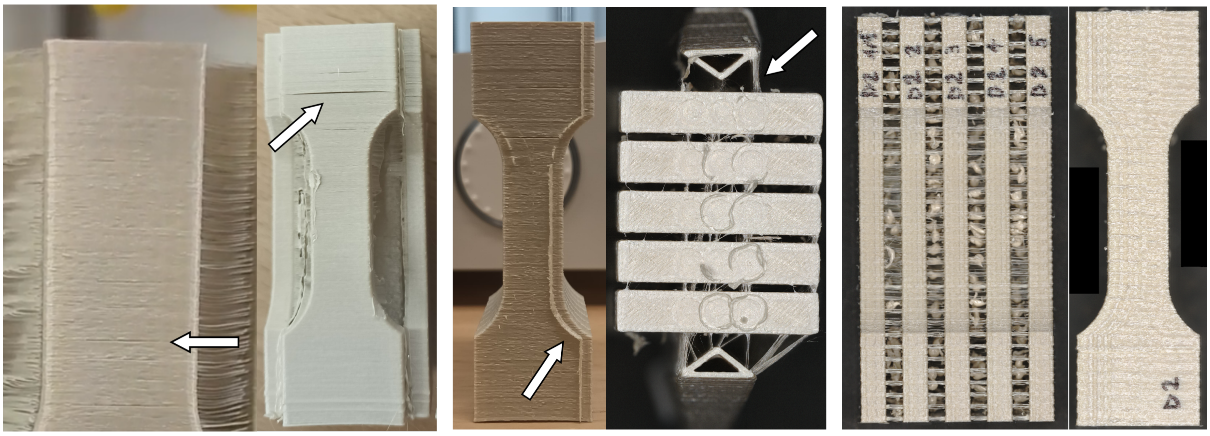

(a) Interlaminar cracks (b) Stringing fibers (c) No artifacts

Figure 5.6: Undesirable features in printed specimen batches. (a) shows interlayer cracks observed in reference specimens during printing; arrows highlight the most prominent failures. (b) shows stringing lines formed between specimens, which made post-processing difficult. (c) Stringing was reduced to a minimum manageable amount.

Batch printing extends the time between subsequent layer depositions. As discussed in Subsection 4.1.1, longer interlayer times can weaken adhesion. When printing with the low speeds reported in previous LCP studies, specimens exhibited pronounced interlayer cracking, as shown in Figure 5.6a. This behavior is reminiscent of warping in materials like ABS, where large temperature gradients across layers cause deformation. However, due to the inherently low interlayer strength of Vectra® A950, the thermal gradient results in cracks between layers rather than warping of the entire part. Increasing the printing temperature and decreasing the layer height helped reduce crack formation, but did not eliminate it. To further mitigate cracking, higher print speeds were explored to shorten the time between layers. However, this introduced new challenges: at elevated speeds, extrusion delay became significant (see Section 4.2), causing visible under-extrusion defects (Figure 5.7a). A speed of 90 mm/s led to poorly bonded layers and inconsistent infill. An iterative tuning process identified an intermediate speed that avoided visible cracks while maintaining proper extrusion. The resulting specimen section, printed at 45 mm/s, is shown in Figure 5.7b, and represents the final optimized print quality.

---

[5] NematX recommended lowering the layer height to improve layer adhesion.

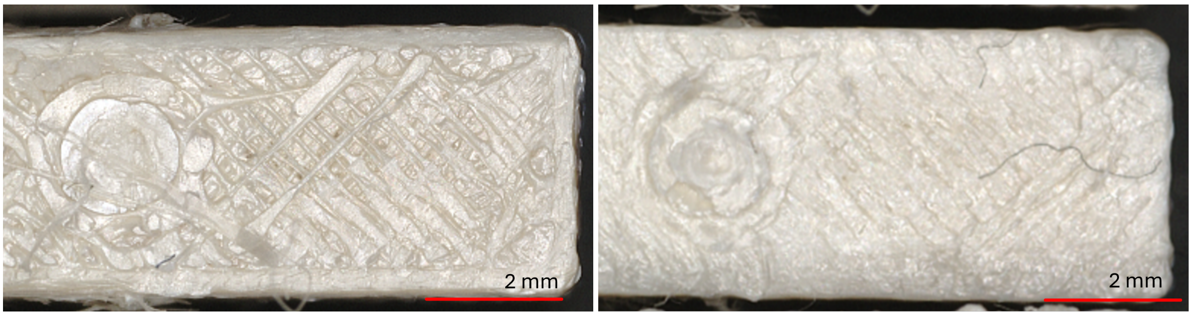

(a) Underextruded infill at high printing speed (b) Correct extrusion at lower printing speed

Figure 5.7: Effect of print speed on extrusion quality. (a) shows under-extrusion in a specimen printed at 90 mm/s, resulting in incomplete infill deposition. (b) shows consistent extrusion and solid infill in a sample printed at 45 mm/s, following speed optimization.

Printing and post processing

The printing parameters for reference and pinned specimens were identical, except for the infill pattern: pinned specimens used rectilinear infill, while reference specimens required concentric infill due to slicer limitations. Full slicer settings are detailed in Appendix C. [6] Each batch included five specimens, exceeding the minimum of four to allow for possible print or test failures. Batches are only comparable when printed with the same number of parts, as this affects inter-layer time and mechanical performance. Figure 5.8 shows the complete printing and post-processing workflow. Figure 5.8a depicts the reference batch, free of over-extrusion, while Figure 5.8b shows a batch of medium pin ABC specimens with visible extrusion at the pin locations. After printing, post-processing differed slightly. Specimens need to be detached from the batch, a step that, for reference specimens, often results in cracking of the specimen, as shown in Figure 5.8c. Cracking occurs accidentally during the handling of the batch due to low interlayer adhesion. Pinned specimens required an additional trimming step to remove the excess material caused by over-extrusion. This step is illustrated in Figure 5.8d and Figure 5.8e, which show a specimen before and after manual cleanup.

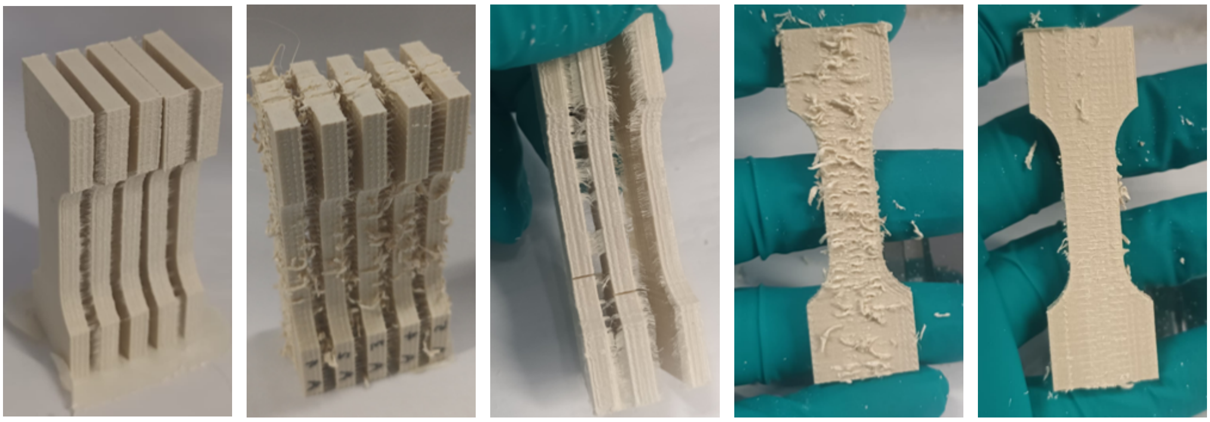

(a) Reference batch (b) Pinned batch (c) Detaching (d) Before removal of excess (e) After removal of excess

Figure 5.8: Printing and post-processing of test specimens. (a) shows a batch of reference specimens without pins. (b) shows a batch of pinned specimens with visible signs of over-extrusion. (c) illustrates specimen detachment, where interlayer cracking can occur. (d) shows a pinned specimen before removing the over-extruded material. (e) displays the same specimen after trimming.

Impact of pins on manufacturing cost

Pin infill directly influences manufacturing cost, as increased infill typically leads to higher print times and filament usage. Table 5.2 summarizes the print duration and filament consumption per specimen for all configurations tested. These values are derived from Klipper logs rather than slicer estimates, since the slicer was found to underestimate the print time by approximately 8% for the reference specimen. As expected, configurations with greater pin infill (see Table 5.1) generally show longer print times. This increase is not primarily due to the pin extrusion itself, but to the slowdown introduced by printing around cavities. The nozzle follows a trapezoidal speed profile (see **??**), and complex cavity shapes reduce travel speeds more than regular quadrilateral patterns. As a result, areas with pin cavities require more time to print, even though they may involve

---

[6] The .3mf files used for slicing are available at `https://github.com/LorenzoOnorato/z_pinning_fff_research`

less extruded volume. Interestingly, the medium ABC configuration with pins and its unpinned counterpart require nearly the same print time, despite a significant difference in filament usage. This further supports the notion that geometry, not just extrusion, drives print duration. One notable exception is the tall ABA configuration, which takes about 20% less time than the tall ABC setup. This is because the printing slowdown in tall ABA is confined to a few particularly slow layers, while the remaining layers are relatively unimpeded. Filament consumption is higher for pinned specimens due to the extrusion modifier exceeding 100% (see Table B.1 in Appendix B). As expected, larger pin infill (shorter pins) correlates with greater material usage. In summary, both print time and filament usage increase with pin infill. However, the overall cost is also influenced by the pin geometry and staggering order, which determine how significantly the cavity geometry interferes with the printing process.

Table 5.2: Printing time and material cost associated with each pin configuration. Values refer to a single specimen and were obtained by dividing Klipper-recorded batch data by the number of specimens. The full definitions of the dimensions are provided in the footnotes.

Pin type	**Staggering order**	**Print time (hh:mm)**	**Increase in print time [1] (%)**	**Filament used [2] (m)**	**Increase in filament [3] (%)**
reference	N\A	3:25	N\A	1.57	N\A
short	ABA, ABC	4:28	30.3	1.62	3.57
medium	AB	4:09	21.2	1.59	1.78
	ABA, ABC	4:24	28.6	1.61	2.68
	ABC (unpinned)	4:13	23.1	1.33	N\A
tall	ABA	3:43	8.6	1.60	2.29
	ABC	4:21	27.4	1.60	2.29

[1] Increase relative to the reference specimen, which required 3 hours and 25 minutes per specimen.
[2] Total filament length as reported by Klipper, averaged per specimen.
[3] Increase in filament used relative to the reference specimen, which required 1.57 m per specimen.

5.2. Mechanical performance from tensile testing

Mechanical testing represents the final phase in assessing the effectiveness of z-pins. The manufactured and post-processed specimens underwent static tensile tests, and this section presents the analysis of the resulting data. An extensive summary of the test result is provided in Appendix D. The discussion in this section is structured in three parts. First, Subsection 5.2.1 demonstrates that increasing pin infill correlates with improved mechanical performance in 3D-printed Vectra® A950. Next, Subsection 5.2.2 investigates how pin geometry and staggering influence strength to identify the most effective configuration. Finally, Subsection 5.2.3 explores the failure behavior of pinned specimens to understand the reinforcement mechanisms. Further insights are available in Appendix E, which includes test setup details (Section E.1) and a comparison of different testing configurations (Section E.2). The suitability of the reference specimen is assessed in Section E.4, and additional analyses on toughness and energy dissipation are presented in Section E.5.

In this section, mechanical performance is evaluated using load (F), displacement (ΔL), and work (W). Tensile load and displacement are recorded directly by the machine. Displacement is measured clamp-to-clamp. While toughness is often defined as the area under a stress–strain curve, its quantification is complicated by the lack of local strain data and definitional ambiguity. Instead, work is used as a proxy for toughness. Three work-based metrics are considered: work to maximum load (W to $F_{\max}$), post-peak work (W after $F_{\max}$), and total work (with the last two being reported in Appendix E). The first represents the material's capacity before damage; the second reflects energy dissipation. [7] To visualize the spread in mechanical performance, box plots are used. These represent the interquartile range (IQR) as the box, with the median as a line inside it. Whiskers extend to the farthest data points within 1.5 times the IQR from the lower and upper quartiles, while data points beyond this range are plotted as outliers . [8]

---

[7] Toughness and energy dissipation are not conventionally measured via tensile testing. Although toughness is generally taken as the area beneath a stress-strain curve, its exact definition can vary among academic references. It can be described as the strain energy before damage sets in (also called modulus of resilience) or as the energy absorbed until fracture, with ambiguity remaining about what constitutes fracture. Furthermore, toughness-related behavior is commonly quantified through the fracture toughness parameter rather than pure energy metrics. Additionally, toughness is computed by normalizing the energy by the gauge volume, but the test data lacks data on gauge strain. The combination of these considerations leads to a preference for using work as the comparative dimension. Work (W), being an energy measure itself, thus aligns with both the modulus of resilience and fracture energy and is simpler to compute as $W = F \cdot \Delta L$. This work isn't normalized over the gauge length and is intended more for insight rather than precise quantification.

[8] The definition of the components of a box plot is based on `https://www.jmp.com/en_us/statistics-knowledge-portal`

5.2.1. Improvement in performance with increasing pin infill

Tensile tests were conducted on specimens with varying pin infill to investigate how pin volume influences mechanical performance. As shown in Table 5.1, the medium AB and medium ABC configurations exhibit pin infills of 9.9% and 14.8%, respectively. These are compared against the reference configuration with 0% pin infill in Figure 5.9. Despite having the same pin volume as medium ABC, pin configuration medium ABA is excluded from the analysis due to its anomalous behavior. The anomaly is discussed in Section E.3. Figure 5.9 presents two metrics: Figure 5.9a displays the maximum tensile load (F_{max}), and Figure 5.9b shows the work done up to that maximum load. Although the dataset is limited, both plots reveal a consistent trend: mechanical performance improves with increasing pin infill. Specifically, both peak load and energy absorption increase over the investigated infill range.

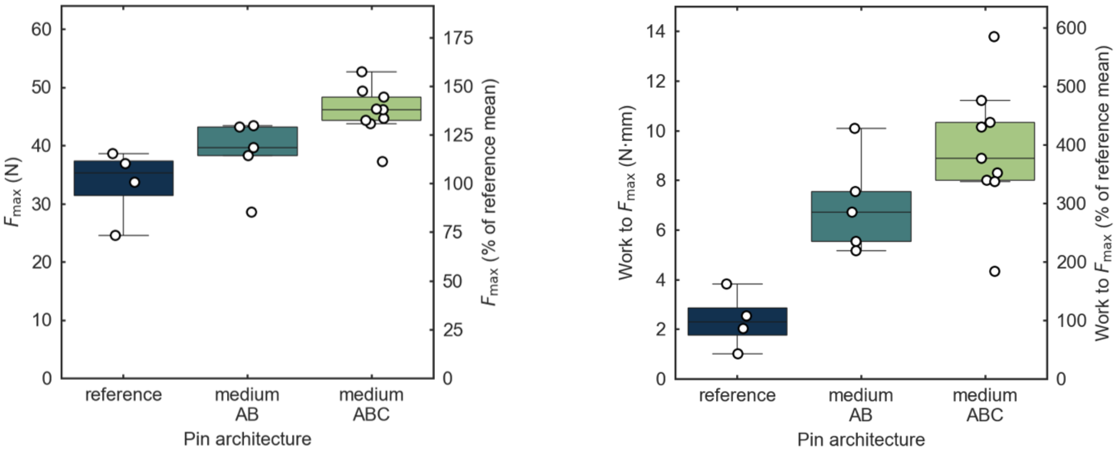

(a) Maximum load for different pin infill

(b) Work executed till maximum load for different pin infill

Figure 5.9: Mechanical performance for different pin infills. (a) shows the maximum tensile load sustained by each specimen type. (b) presents the work done on the specimen up to F_{max}, used here as a proxy for toughness before failure.

5.2.2. Improvement of pin configuration

To identify the optimal pin configuration, six combinations of pin geometry and column staggering were tested. These configurations involved three pin lengths (short, medium, tall) and two staggering patterns (ABA and ABC), with an equal number of pins in each. Figure 5.10 shows the maximum tensile load (F_{max}) for these six configurations, separated by staggering pattern: ABA in Figure 5.10a, and ABC in Figure 5.10b. Similarly, Figure 5.11 presents the corresponding work done up to F_{max} (W to F_{max}), again divided between ABA and ABC layouts (Figure 5.11a and Figure 5.11b, respectively). Both figures contain an indication of the interval of the reference batch from Figure 5.9 for comparison.

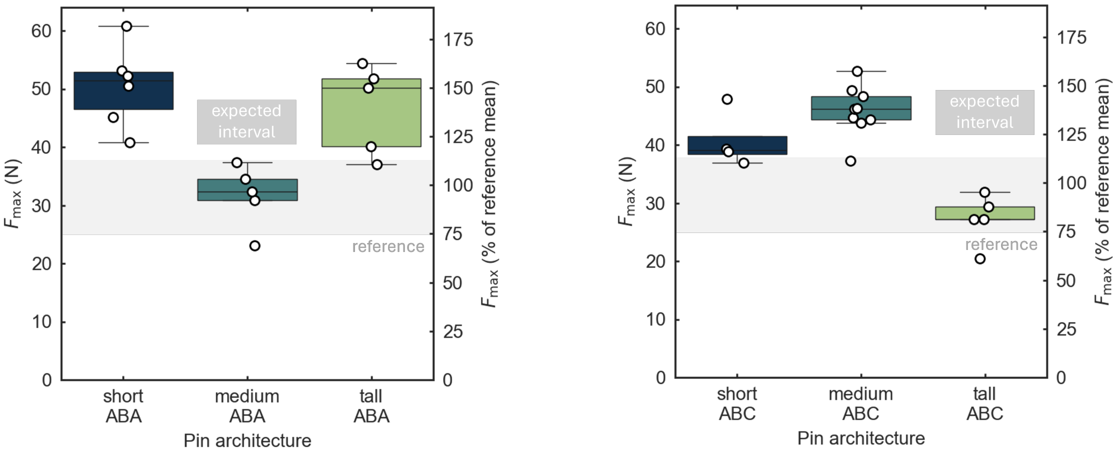

(a) ABA pin architectures

(b) ABC pin architectures

Figure 5.10: Comparison of tensile load for different pin geometries and staggering orders. (a) Reports the maximum tensile load (F_{max}) for specimens with ABA staggering, while (b) presents the same data for the ABC configurations. The performance range of the reference specimens is depicted in light gray.

The F_{max} results do not reveal a consistent trend concerning either pin geometry or staggering pattern. Both the short ABA and tall ABA configurations show an increase in maximum load of approximately 50% compared to the reference specimen, while the medium ABA configuration exhibits a slightly lower average. Inspection of the force-displacement curves for the medium ABA and tall ABC specimens reveals unexpected behavior, likely due to insufficient pin engagement. These irregularities suggest that the observed performance may not reflect the true potential of these configurations. Accordingly, their validity is examined in more detail in Section E.3, and the plots contain an indication of the expected performance range inferred from the remaining data. A more pronounced trend emerges in the work-related results (Figure 5.11). Specimens with the ABA staggering pattern consistently display greater W to F_{max} values than their ABC counterparts. Similarly, taller pins tend to absorb more energy. The tall ABA configuration, in particular, shows a dramatic improvement, with work values ranging from 5 to 20 times that of the reference. Such improvement is also connected to a larger spread. The larger spread is due to the failure sequence associated with this pin architecture, which differs from the others and is intrinsically more irregular. The differences between fracture patterns are shown in Appendix D.

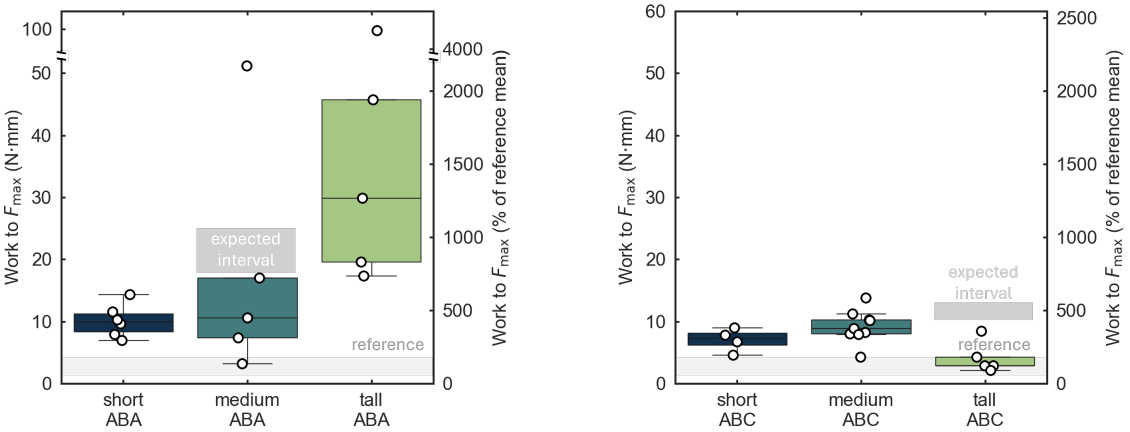

(a) ABA pin architectures

(b) ABC pin architectures

Figure 5.11: Work to F_{max} for different pin geometries and staggering orders. (a) presents the energy absorbed by specimens with ABA pin layouts. (b) shows the same for specimens with ABC staggering. The performance range of the reference specimens is depicted in light gray.

5.2.3. Damage tolerance and strength recovery

Analyzing the whole force-displacement curve offers insights into the strengthening mechanisms introduced by z-pins. Figure 5.12 examines a representative short ABA specimen. In Figure 5.12, four numbered points are marked along the force-displacement curve, each corresponding to a specific stage of deformation. These are linked to frames of footage recorded during testing. Starting from $\Delta L = 0$, the curve progresses linearly, indicating elastic behavior. Up to point 1, no damage is visible. Between points 1 and 2, the load drops in two steps as cracks begin to form, with point 1 identified as the crack onset load (F_{crack}). After point 2, the load recovers and surpasses its previous maximum, reaching point 3. The region between points 2 and 3 is thus referred to as the strength recovery phase. This segment has a lower and decreasing slope, suggesting progressive damage but continued load transfer. Visual data confirm that central pins remain engaged, bridging the crack, while edge pins lose contact due to crack propagation along discontinuities. Beyond point 3, the load sharply decreases. At point 4, the specimen has fractured, though the load does not drop to zero. Instead, it levels off due to residual strength from bridging layer lines, which slowly delaminate with increasing strain. In summary, the specimen exhibits a linear elastic region up to F_{crack}, followed by a partial drop in load due to crack formation, and then a load recovery enabled by the pins. The presence of a load recovery demonstrates that the pins not only arrest cracks but also restore load-bearing capacity.

The presence of the strength recovery phase before F_{max}, as described above, is typical of most pinned configurations, with exceptions discussed in Section E.3. Notably, tests using the Instron setup differ significantly: they exhibit no F_{crack}, instead reaching F_{max} pseudo-linearly. While this might appear preferable for applications operating in the elastic regime, the Zwick setup results demonstrate the pins' ability to both arrest cracks and restore load-bearing capacity. Future work should focus on improving crack initiation resistance without compromising post-peak performance.

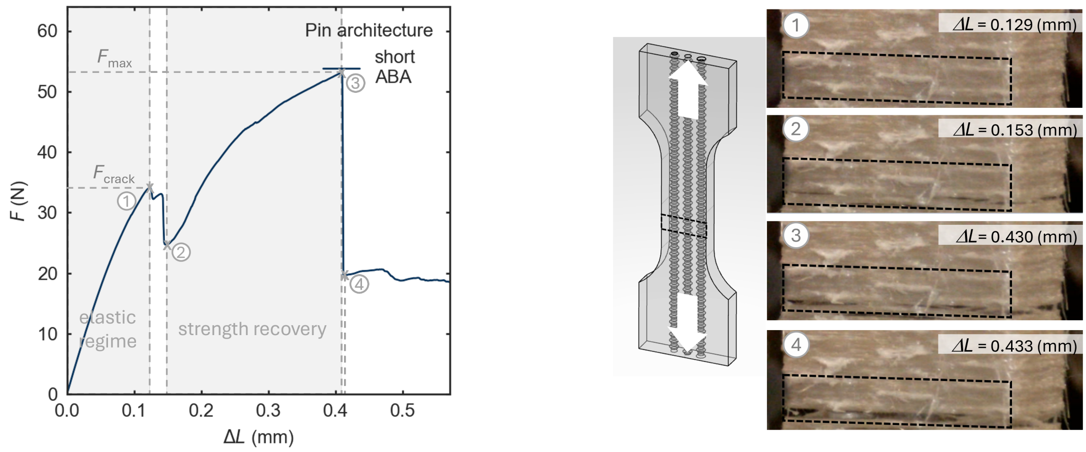

Figure 5.12: Analysis of the force-displacement curve of a short ABA specimen. (a) shows key stages in the force-displacement response, numbered 1 to 4. (b) links these stages to the specimen's visual appearance during testing.

Configurations with short pins exhibit a rapid drop in load after failure, while medium and tall pins display more gradual declines, often followed by strength recovery. To quantify post-peak strength recovery, a new metric is introduced in Figure 5.13: F_{recovery}. It is defined as the first local peak following F_{max}. In many cases, F_{recovery} exceeds 80% of the initial peak, suggesting effective load redistribution. However, F_{recovery} captures only a single post-peak event. For more comprehensive insight into repeated recoveries, readers are referred to Section D.3. Overall, tall pins and ABA-staggered configurations yield the highest F_{recovery} values.

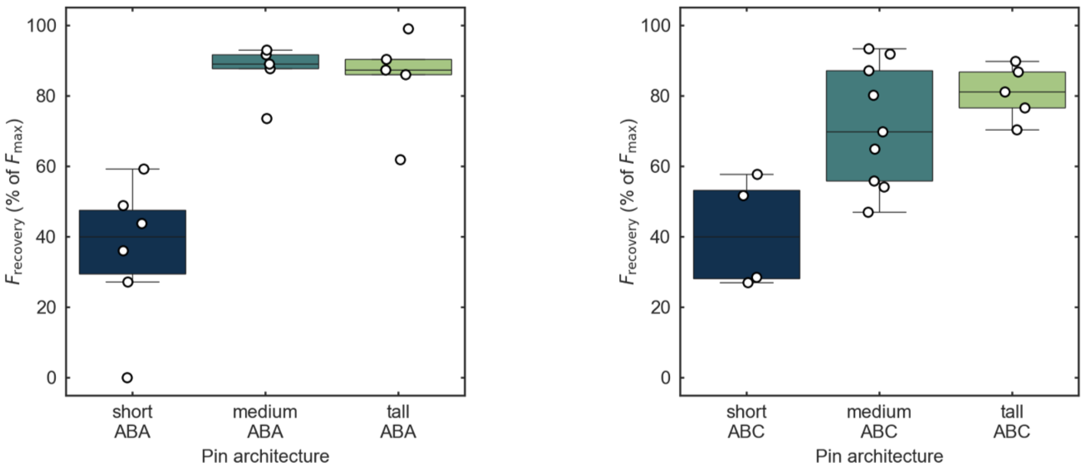

(a) ABA pin architectures

(b) ABC pin architectures

Figure 5.13: Comparison of F_{recovery} from different pin geometries and staggering orders. (a) shows the ABA configurations, while (b) displays ABC configurations.

To further investigate how cracks form and propagate, Figure 5.14 shows a series of snapshots from a test on a tall ABA specimen, from the best-performing configuration. At step 0, the specimen is undamaged. Cracks initiate at the edges and pin discontinuity locations during steps 1 and 2. Importantly, multiple cracks form without immediate catastrophic failure, suggesting an improvement over the reference fracture mode. Cracks seem to appear earlier on the edges of the specimen and in correspondence with pin over-extrusion locations. These locations coincide with the pin-column discontinuities. A central crack appears in step 3, while previously formed cracks remain stable. Step 4 shows a previously nucleated crack extending across the specimen and being halted by a pin. Steps 5 and 6 illustrate a similar propagation of cracks in other sections of the specimen. These observations lead to several conclusions. First, peak load is still constrained by the regular layer infill interlaminar strength. Enhancing the number, size, and arrangement of pins could optimize pin material distribution to prevent delamination. Second, tall pins arrest cracks as intended, and their geometry successfully ensures mechanical interlocking between the layers. Third, since cracks initiate at the discontinuity locations, longer pins not only improve the maximum mechanical performance but also delay the onset and propagation of damage.

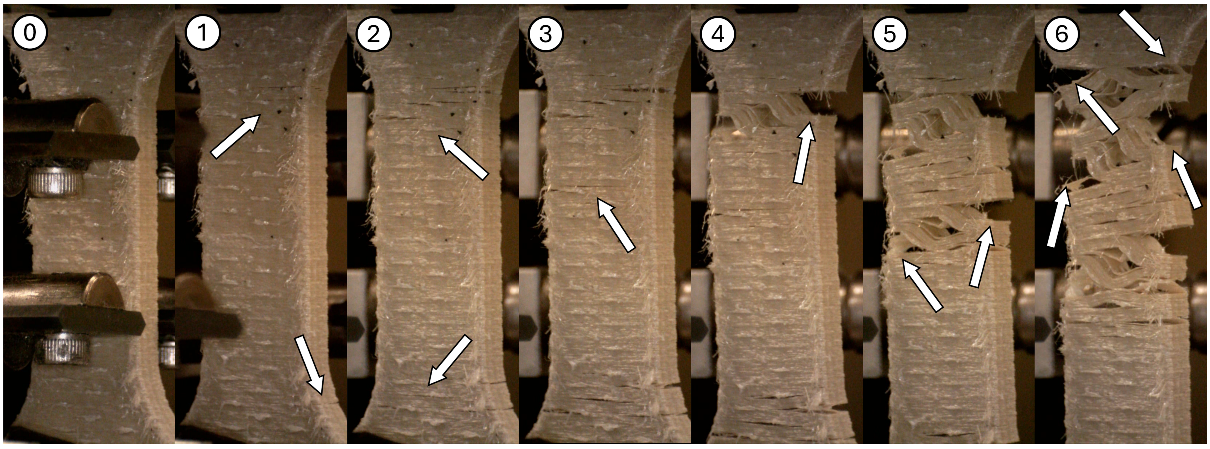

Figure 5.14: Failure sequence in a tall ABA specimen during tensile testing. White arrows indicate crack initiation and propagation. This specimen corresponds to D002-3 in Appendix D.

5.3. Chapter summary

This chapter presented the conceptual development, manufacturing process, and mechanical evaluation of z-pinned tensile specimens fabricated using Vectra® A950 filament. The work began by identifying a tensile specimen geometry that strikes a balance between mechanical relevance and printability. A previously validated design for LCPs was selected over standard ISO geometries due to its reduced slenderness ratio, which facilitates fabrication. However, as prior testing used different printers and settings, reference specimens were printed to establish a consistent baseline for comparison.

The design and manufacturing phase centered on introducing pin cavities into the gauge section, selecting feasible pin configurations, and developing a reliable production workflow. The limited cross-sectional area of the specimen constrained the number and size of pins, as discussed in the previous chapter. Based on these limitations, pin geometry and count were fixed, and attention shifted to the spatial arrangement of the pins. Two vertical staggering sequences were explored: ABA and ABC. In ABA, two columns share the same vertical position while half a pin height offsets the third; in ABC, each of the three columns is offset by a third of the pin height. Eight pin configurations were ultimately tested, combining staggering sequences and pin heights (short, medium, tall). These were supplemented with a reference (unpinned) configuration and a low-infill variant. Manufacturing these designs posed challenges, particularly in ensuring cavity fidelity and interlayer adhesion, which were overcome through iterative tuning of print parameters.

The tests confirmed that increasing pin infill resulted in higher nominal strength and work absorption within the investigated range. Among the tested configurations, the tall ABA pin layout exhibited the most significant improvement, achieving a 40% increase in peak load and a tenfold increase in work to maximum load compared to the reference. The ABA configuration enabled more effective load transfer between layers as well as taller pins. In addition to global metrics like load and work, the damage tolerance of the specimens was assessed through post-failure inspections. Cracking behavior and failure sequences demonstrate that the strengthening mechanism provided by pins involves arresting crack propagation. While damage tolerance and energy dissipation were not the primary focus of this study, the data suggest that pinned specimens offer improvements in both areas.

6

Conclusions and recommendations

Conclusions

This work aimed to investigate whether z-pinning can enhance the mechanical performance of 3D-printed LCP parts fabricated using Vectra® A950 filament. The motivation arose from a key limitation of FFF of LCPs. While the process achieves excellent in-plane strength due to flow-induced molecular alignment, the weak interlayer adhesion severely compromises properties along the build direction. Adapting and extending the concept of z-pinning, originally developed using PLA printing, to anisotropic LCPs, this research aimed to evaluate its feasibility, define a viable implementation method, and assess its mechanical impact.

The results confirm that z-pinning can measurably improve tensile performance in the Z-direction. Specimens with tall pins arranged in an ABA staggering pattern exhibited a 40% increase in peak load and approximately tenfold energy absorption compared to unpinned controls. These findings demonstrate that vertically deposited pins can serve as interlayer strengthening strategies, enhancing load-bearing capacity and modifying fracture behavior in anisotropic 3D-printed parts. These improvements were not limited to quantitative performance. Qualitative examination of fracture surfaces revealed a transition from brittle, localized delamination to more distributed damage. In the best-performing configurations, failure propagated less abruptly, with crack paths deviating and being arrested, indicating improved damage tolerance. Importantly, these enhancements were achieved without altering the base material or introducing a secondary phase.

The performance gains were made possible through the development and implementation of a bottom-up z-pinning strategy compatible with standard FFF hardware. The work required extensive process adaptation, including the design of pin cavities, compensation for extrusion delay, and optimization of a custom G-code deposition routine. The resulting pin geometry, a tapered wedge shape spanning multiple layers, was designed to promote mechanical interlocking and allow for flexible placement. Variations in pin height and column staggering were explored, with the tall ABA configuration yielding the most consistent and pronounced improvements. Despite the inherent limitations of off-the-shelf hardware and the sensitivity of LCP printing, the process proved sufficiently robust to produce repeatable, testable specimens.

The findings presented here are significant, but the development effort was equally impactful. Much of this thesis was devoted to developing the process architecture that enabled z-pinning, including conceptual development, print head tuning, G-code optimization, and compensating for delays in material deposition. These aspects were essential for laying the groundwork. Still, they also revealed the process bottlenecks, particularly the need for precise control over extrusion and the limitations of standard nozzles for achieving the required pin insertion depth.

Beyond the technical success, this work reinforces a broader principle shared by both additive manufacturing and traditional fiber-reinforced composites: material performance can be enhanced not only by selecting the right material, but by controlling how and where it is placed. In this context, the deliberate introduction of z-pins becomes a powerful tool to tailor structural behavior, particularly along the weakest direction of printed parts. Moreover, this study highlights the importance of concurrent development of design and manufacturing processes, demonstrating that enabling new structural features, such as z-pins, requires not only conceptual innovation but also dedicated attention to process architecture, print parameter tuning, and hardware capabilities.

Recommendations for future work

Several clear directions emerge to build on this foundation:

Toughness characterization: While this study emphasized tensile strength and energy absorption, future work should focus on characterizing toughness more rigorously. Pins appear particularly promising for delaying crack propagation and distributing stress, suggesting strong potential in enhancing damage tolerance. Controlled crack initiation experiments, fracture toughness testing, and digital image correlation during loading would offer deeper insight into these mechanisms.

Extrusion control and hardware development: The print quality and mechanical benefits of pinning are limited by current hardware capabilities. Custom nozzles with narrower tips and longer tapers could enable the use of deeper or thinner pins, thereby expanding the design space for reinforcement strategies. Furthermore, precise management of the extrusion delay is essential for achieving an improvement in overall print quality and becomes even more critical when dealing with intricate deposition patterns.

Digital workflow integration: One of the barriers to widespread adoption is the manual and experimental nature of z-pinning today. The next step should be the integration of pinning into slicing software. A practical model would mirror how support structures are handled: users could activate z-pinning globally, allowing the software to suggest pin locations based on geometry, stress profiles, or user-defined zones. These auto-generated pins should then be manually adjusted to fine-tune coverage or accommodate specific functional features. Such a semi-automated workflow would enable pinning to be designable, customizable, and compatible with industrial manufacturing workflows.

Adoption pathways and use cases: Given the manufacturing complexity, z-pinning is unlikely to be adopted widely in hobbyist printing. However, for small to medium-scale production (e.g., 100–1,000 units), particularly in the aerospace industry, performance gains from z-pinning can justify the additional development cost. In such environments, pins may become a standard design element introduced during the early design phase, much like rivets or inserts today. In this scenario, design engineers and 3D printing specialists would collaborate to embed reinforcement features directly into part geometries where delamination or damage risk is expected.

Part types and design strategies: Initially, z-pinning is likely to be adopted in complex, customized geometries—those parts where layer orientation and aspect ratio demand highly tailored reinforcement. However, with maturity, it could scale to more standardized elements such as brackets, interconnects, and ribs. A parameterized approach where pin placement follows predefined design rules would be key to scaling up.

Material generalization: Although this thesis focused on Vectra® A950, the insights gained are broadly applicable to other shear-aligning thermotropic LCPs. The nature of LCPs makes them especially well-suited to z-pinning, as their anisotropy and low interlayer adhesion leave room for cross-layer enhancements. Other shear-aligning materials, such as carbon fiber-filled filaments, are strong candidates as well. In contrast, unfilled, isotropic materials are less likely to benefit, both due to their lower performance ceiling and lack of flow-driven alignment.

Combination with other Strategies: Future studies could explore combining z-pinning with other reinforcement strategies. Spin printing, co-extrusion, and thermal annealing could be co-optimized to improve performance across multiple axes. Hybrid strategies may help overcome the limitations of any single method, particularly where load cases are complex or anisotropy is not aligned with stress paths.

Bibliography

[1] N. van de Werken, M. Tehrani *et al.*, "Additively manufactured carbon fiber-reinforced composites: State of the art and perspective," *Additive Manufacturing*, vol. 31, p. 100962, 2019. [Online]. Available: https://doi.org/10.1016/j.addma.2019.100962

[2] T. J. Coogan and D. O. Kazmer, "In-line rheological monitoring of fused deposition modeling," *Journal of Rheology*, vol. 63, no. 1, pp. 141–155, 2019. [Online]. Available: https://doi.org/10.1122/1.5054648

[3] S. Gantenbein, K. Masania, W. Woigk, J. P. W. Sesseg, T. A. Tervoort, and A. R. Studart, "Three-dimensional printing of hierarchical liquid-crystal-polymer structures," *Nature*, vol. 561, no. 7724, pp. 226–230, 2018. [Online]. Available: https://doi.org/10.1038/s41586-018-0474-7

[4] C. C. M. C. A. G. Houriet, "Shaping anisotropy: 3D-printing of liquid crystal polymers," Ph.D. dissertation, Delft University of Technology, 2024. [Online]. Available: https://doi.org/10.4233/uuid:d59312f1-7ae2-4eb2-914c-ec830a065dc7

[5] W. A. MacDonald, "Thermotropic main chain liquid crystal polymers," in *Liquid Crystal Polymers: From Structures to Applications*, A. A. Collyer, Ed. Dordrecht: Springer, 1992, pp. 407–446.

[6] C. Houriet, V. Damodaran, C. Mascolo, S. Gantenbein, D. Peeters, and K. Masania, "3D printing of flow-inspired anisotropic patterns with liquid crystalline polymers," *Advanced Materials*, vol. 36, no. 11, p. 2307444, 2024. [Online]. Available: https://doi.org/10.1002/adma.202307444

[7] W. Xu, H. Xu, X. Zhai, and J. Jiang, "Weavex: Nature-inspired non-planar strategies for extrusion additive manufacturing," *Additive Manufacturing*, 2023, in review or preprint. [Online]. Available: https://www.researchgate.net/publication/382058951

[8] T. J. Coogan and D. O. Kazmer, "Modeling of interlayer contact and contact pressure during fused filament fabrication," *Journal of Rheology*, vol. 63, no. 4, pp. 655–672, 2019. [Online]. Available: https://doi.org/10.1122/1.5093033

[9] C. Houriet, "Additive manufacturing of liquid crystal polymers interlayer features: Formation & impact on interlaminar shear strength," Master's thesis, Delft University of Technology, Faculty of Aerospace Engineering, Department of Structures and Materials, December 2019, Available: https://resolver.tudelft.nl/uuid:1104f824-a4a7-4cf6-bdae-fac9441b5b24.

[10] C. Duty, J. Failla, S. Kim, J. Lindahl, B. Post, L. Love, and V. Kunc, "Reducing mechanical anisotropy in extrusion-based printed parts," in *Proceedings of the 28th Annual International Solid Freeform Fabrication Symposium*. Society of Manufacturing Engineers, 2017, Conference paper. [Online]. Available: http://utw10945.utweb.utexas.edu/sites/default/files/2017/Manuscripts/ReducingMechanicalAnisotropyinExtrusionBased.pdf

[11] C. Duty, J. Failla, S. Kim, T. Smith, J. Lindahl, A. Roschli, B. Post, L. Love, and V. Kunc, "Z-pinning approach for reducing mechanical anisotropy of 3D printed parts," in *Proceedings of the 29th Annual International Solid Freeform Fabrication Symposium*. Society of Manufacturing Engineers, 2018, Conference paper. [Online]. Available: http://dx.doi.org/10.26153/tsw/17233

[12] C. Duty, J. Failla, S. Kim, T. Smith, J. Lindahl, and V. Kunc, "Z-pinning approach for 3D printing mechanically isotropic materials," *Additive Manufacturing*, 2019. [Online]. Available: https://doi.org/10.1016/j.addma.2019.03.007

[13] S. Kim, T. Smith, J. Condon, A. Lambert, V. Kunc, and C. Duty, "Geometric parameter analysis of vertically extruded pins for strength improvement in additive manufacturing with fiber-reinforced thermoplastic," in *SAMPE Conference Proceedings*. Seattle, WA: SAMPE, 2020, Conference paper. [Online]. Available: https://www.osti.gov/biblio/1651354

[14] B. Bales, T. Smith, S. Kim, V. Kunc, and C. Duty, “Evaluating the effect of z-pinning parameters on the mechanical strength and toughness of printed polymer composite structures,” in *Solid Freeform Fabrication 2021: Proceedings of the 32nd Annual International Solid Freeform Fabrication Symposium*. Solid Freeform Fabrication, 2021, Conference paper. [Online]. Available: http://dx.doi.org/10.26153/tsw/17572]

[15] B. C. Ulyanov, “Interlaminar toughening approaches for additively manufactured liquid crystal polymers,” Master’s thesis, Delft University of Technology, Faculty of Aerospace Engineering, Department of Structures and Materials, November 2023, Available: https://resolver.tudelft.nl/uuid:979d28f2-dddb-4fa2-84fd-7ccc76ce707e.

[16] A. Al Rashid, S. Khan, and M. Koç, “Additive manufacturing: Technology, applications, markets, and opportunities for the built environment,” *Automation in Construction*, vol. 118, p. 103268, 2020. [Online]. Available: https://doi.org/10.1016/j.autcon.2020.103268

[17] M. Q. Zafar and H. Zhao, “4D printing: Future insight in additive manufacturing,” *Metals and Materials International*, vol. 26, pp. 564–585, 2020. [Online]. Available: https://doi.org/10.1007/s12540-019-00441-w

[18] ASTM International, *Standard Terminology for Additive Manufacturing Technologies*, Std. F2792-12, 2012, ASTM Committee F42 on Additive Manufacturing Technologies. [Online]. Available: https://web.mit.edu/2.810/www/files/readings/AdditiveManufacturingTerminology.pdf

[19] H. Bikas, P. Stavropoulos, and G. Chryssolouris, “Additive manufacturing methods and modelling approaches: A critical review,” *International Journal of Advanced Manufacturing Technology*, vol. 83, pp. 389–405, 2016. [Online]. Available: https://doi.org/10.1007/s00170-015-7576-2

[20] J. Holmström, J. Partanen, J. Tuomi, and M. Walter, “Rapid manufacturing in the spare parts supply chain: Alternative approaches to capacity deployment,” *Journal of Manufacturing Technology Management*, vol. 21, pp. 687–697, 01 2010. [Online]. Available: https://doi.org/10.1108/17410381011063996

[21] K. S. Reddy and S. Dufera, “Additive manufacturing technologies,” *BEST: International Journal of Management, Information Technology and Engineering (BEST: IJMITE)*, vol. 7, no. 7, pp. 89–112, July 2019. [Online]. Available: https://www.researchgate.net/publication/334545466_ADDITIVE_MANUFACTURING_TECHNOLOGIES

[22] W. Xu, H. Xu, X. Zhai, and J. Jiang, “Nature-inspired interlaced printing strategies for additive manufacturing highly improved mechanical properties,” *Additive Manufacturing*, vol. 89, p. 104276, 2024. [Online]. Available: https://doi.org/10.1016/j.addma.2024.104276

[23] C. Mascolo, “Spin-printing of liquid crystal polymers fibres,” Master’s thesis, ETH Zurich, Department of Materials, February 2021.

[24] S. Gantenbein, “3D printing of living and synthetic fiber-based materials,” Ph.D. dissertation, ETH Zurich, 2021, doctoral dissertation, DISS. ETH No. 27663. [Online]. Available: https://doi.org/10.3929/ethz-b-000525628

[25] S. Gantenbein, C. Mascolo, C. Houriet, R. Zboray, A. Neels, K. Masania, and A. R. Studart, “Spin-printing of liquid crystal polymer into recyclable and strong all-fiber materials,” *Advanced Functional Materials*, vol. 31, no. 52, p. 2104574, 2021. [Online]. Available: https://doi.org/10.1002/adfm.202104574

[26] N. Faber, “Improving strength of 3D printed parts through stress-aligned print paths using highly anisotropic liquid crystal polymers,” Master’s thesis, Delft University of Technology, Faculty of Aerospace Engineering, Department of Structures and Materials, November 2021, Available: https://resolver.tudelft.nl/uuid:f67b562c-d94c-4b84-af8f-0682c7ea9017.

[27] B. A. van Leengoed, “5-axis additive manufacturing of hydrogen pressure vessels with liquid crystal polymers,” Master’s thesis, Delft University of Technology, Faculty of Aerospace Engineering, Department of Structures and Materials, July 2022, Available: https://resolver.tudelft.nl/uuid:4c2756a9-022c-4054-842f-6d746f15384c.

[28] X. Guidetti, E. C. Balta, Y. Nagel, H. Yin, A. Rupenyan, and J. Lygeros, “Stress flow guided non-planar print trajectory optimization for additive manufacturing of anisotropic polymers,” *Additive Manufacturing*, vol. 72, p. 103628, 2023. [Online]. Available: https://doi.org/10.1016/j.addma.2023.103628

[29] B. Bales, R. Walker, D. Pokkalla, S. Kim, V. Kunc, and C. Duty, “Design and use of a penetrating deposition nozzle for z-pinning additive manufacturing,” in *Proceedings of the 33rd Annual International Solid Freeform Fabrication Symposium*. Solid Freeform Fabrication, 2022, Conference paper. [Online]. Available: https://www.osti.gov/servlets/purl/1887657]

[30] S. Kim, T. Smith, J. Failla, J. Lindahl, V. Kunc, and C. Duty, “Parametric analysis on vertical pins for strengthening extrusion-based printed parts,” in *SAMPE Conference Proceedings*. Long Beach, CA: SAMPE, 2018, Conference paper. [Online]. Available: https://www.ornl.gov/publication/parametric-analysis-vertical-pins-strengthening-extrusion-based-printed-parts

[31] A. Nasirov, D. K. Pokkalla, B. Bales, T. Smith, C. Duty, V. Kunc, and S. Kim, “Modeling the interfacial failure and resulting mechanical properties of z-pinned additively manufactured composites,” *Materials Today Communications*, vol. 35, p. 105735, 2023. [Online]. Available: https://doi.org/10.1016/j.mtcomm.2023.105735

[32] C. E. Duty, S. Kim, V. Kunc, L. J. Love, B. K. Post, J. A. Failla, and J. M. Lindahl, “Z-axis improvement in additive manufacturing,” US Patent US20 180 311 891A1, November, 2018, patent. [Online]. Available: https://patents.google.com/patent/US20180311891A1/en

[33] V. Kunc, S. Kim, J. M. Lindahl, J. A. Failla, and C. E. Duty, “Penetrating and actuating nozzle for extrusion-based 3D printing,” US Patent US11 623 395B2, April, 2023, patent. [Online]. Available: https://www.osti.gov/biblio/1998272

[34] H. Rutten, “Flow parameters and their effect on extrusion printing,” Master’s thesis, Delft University of Technology, Faculty of Aerospace Engineering, Department of Structures and Materials, December 2024, Available: https://resolver.tudelft.nl/uuid:03a6dd34-4345-49fd-9b23-fb2bb11ed8f6.

[35] E. L. Claassen, “Assessing the space-worthiness of additively manufactured liquid crystal polymers,” Master’s thesis, Delft University of Technology, Faculty of Aerospace Engineering, Department of Structures and Materials, October 2024, Available: https://resolver.tudelft.nl/uuid:6400b8c8-f7c9-4a28-a7ca-fe57357fefed.

[36] C. Houriet, E. Claassen, C. Mascolo, H. Jöhri, A. Brieva, S. Szmolka, S. Vincent-Bonnieu, A. Suliga, R. Heeb, S. Gantenbein, U. Lafont, T. Rohr, and K. Masania, “3D printing of liquid crystal polymers for space applications,” *Advanced Materials Technologies*, vol. 10, no. 4, p. 2400571, 2025. [Online]. Available: https://doi.org/10.1002/admt.202400571

[37] X. Guidetti, N. Mingard, R. Cruz-Oliver, Y. Nagel, M. Rueppel, A. Rupenyan, E. C. Balta, and J. Lygeros, “Force controlled printing for material extrusion additive manufacturing,” *Additive Manufacturing*, vol. 89, p. 104297, 2024. [Online]. Available: https://doi.org/10.1016/j.addma.2024.104297

[38] D. O. Kazmer and A. Colon, “Injection printing: Additive molding via shell material extrusion and filling,” *Additive Manufacturing*, vol. 36, p. 101469, 2020. [Online]. Available: https://doi.org/10.1016/j.addma.2020.101469

[39] N. M. Ceriani and B. Schenk, “Method for Creating a 3D-Part, Involving 3D-Printing, 3D-Part with 3D-Printed Layers and 3D-Printing Device,” Patent EP3 656 535A1, May 27, 2020, patent. [Online]. Available: https://patents.google.com/patent/EP3656535A1/en

[40] V. Oliveira, S. P. Sharma, M. F. S. F. de Moura, R. D. F. Moreira, and R. Vilar, “Surface treatment of CFRP composites using femtosecond laser radiation,” *Optics and Lasers in Engineering*, vol. 94, pp. 37–43, 2017. [Online]. Available: https://doi.org/10.1016/j.optlaseng.2017.02.011

[41] T. J. Gordelier, P. R. Thies, L. Turner, and L. Johanning, “Optimising the FDM additive manufacturing process to achieve maximum tensile strength: a state-of-the-art review,” *Rapid Prototyping Journal*, vol. 25, no. 6, pp. 953–971, 2019. [Online]. Available: https://doi.org/10.1108/RPJ-07-2018-0183

[42] J. Kajimoto, J. Koyanagi, Y. Maruyama, H. Kajita, and R. Matsuzaki, “Automated interlaminar reinforcement with thickness directional fiber arrangement for 3D printing,” *Composite Structures*, vol. 286, p. 115321, 2022. [Online]. Available: https://doi.org/10.1016/j.compstruct.2022.115321

[43] J. Son, S. Yun, K. Park, S. Ryu, and S. Kim, “Isotropic 3D printing using material extrusion of thin shell and post-casting of reinforcement core,” *Additive Manufacturing*, vol. 58, p. 102974, 2022. [Online]. Available: https://doi.org/10.1016/j.addma.2022.102974

[44] J. Chen, X. Liu, Y. Tian, W. Zhu, C. Yan, Y. Shi, L. B. Kong, H. J. Qi, and K. Zhou, "3D-printed anisotropic polymer materials for functional applications," *Advanced Materials*, vol. 34, no. 3, p. 2102877, 2022. [Online]. Available: https://doi.org/10.1002/adma.202102877

[45] *Plastics — Determination of tensile properties — Part 1: General principles*, International Organization for Standardization Std. ISO 527-1:2012, 2012, second edition, February 15, 2012. [Online]. Available: https://www.iso.org/standard/56046.html

A

Tuning of NematX Slicer XY hole compensation parameter

This appendix details the empirical calibration of the "XY hole compensation parameter" in the NematX Slicer, aimed at enhancing the dimensional accuracy of printed holes.

The tuning process involved fabricating stencils with known hole dimensions and iteratively adjusting the XY hole compensation parameter based on measured deviations. Dimensional measurements were performed using a Keyence VR-5000 microscope. Figure A.1 shows microscope images of printed stencils, where deviations in hole diameter are visible despite the models being sliced from the same .stl file. Errors were particularly pronounced for holes with diameters near the line width, underscoring the necessity of compensation tuning. This study complements the discussion in **??**, where the impact of tuning is illustrated by comparing stencil scheme A (Figure 3.11b) with scheme F (Figure 3.11c).

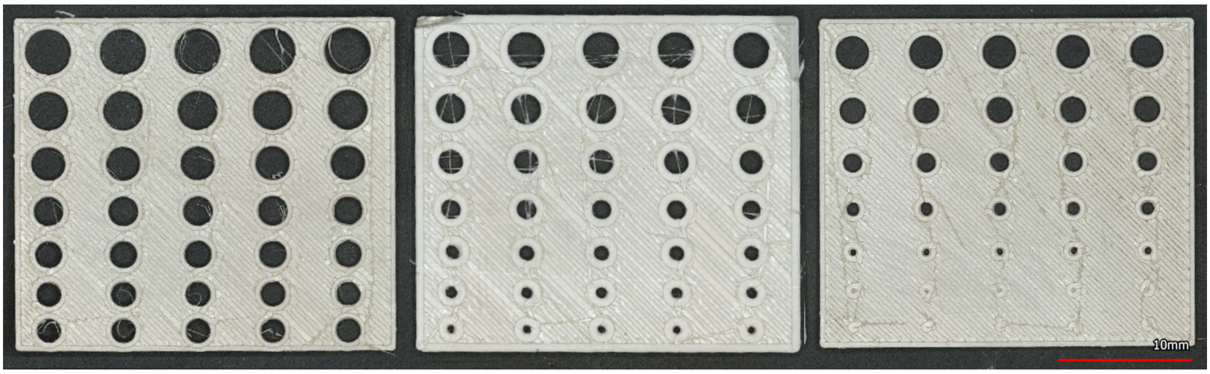

Figure A.1: Microscope images of printed stencils used to quantify hole radius accuracy. Although all samples were sliced from the same STL file, the differences in hole diameters reflect varying XY hole compensation settings. Achieving acceptable tolerances required iterative refinement of the parameters. Performance is also influenced by factors such as extrusion flow, nozzle diameter, and layer height.

The XY hole compensation parameter combinations across various radii were organised into parameter schemes. The sequence and justification for the adjustments in these schemes are detailed in Table A.1. A series of parameter schemes, labeled A through H, were evaluated, and progressive improvement was achieved. For example, scheme A (Table A.2) shows an average error of up to 45%, whereas scheme H demonstrates significant enhancement with deviations reduced to just 1.57% (Table A.9). The scheme used for the rest of the study is scheme F, where the XY hole compensation parameter value for a 0.5 mm diameter is the same as that of scheme H. The evolution of the increased dimensional accuracy is outlined in Figure A.2, depicting a decrease in error as the schemes advance from A to H, reaching a 2.5% threshold, indicative of diminishing returns. Figure A.2a displays the absolute difference, while Figure A.2b presents the percentage difference between the desired and measured hole diameter.

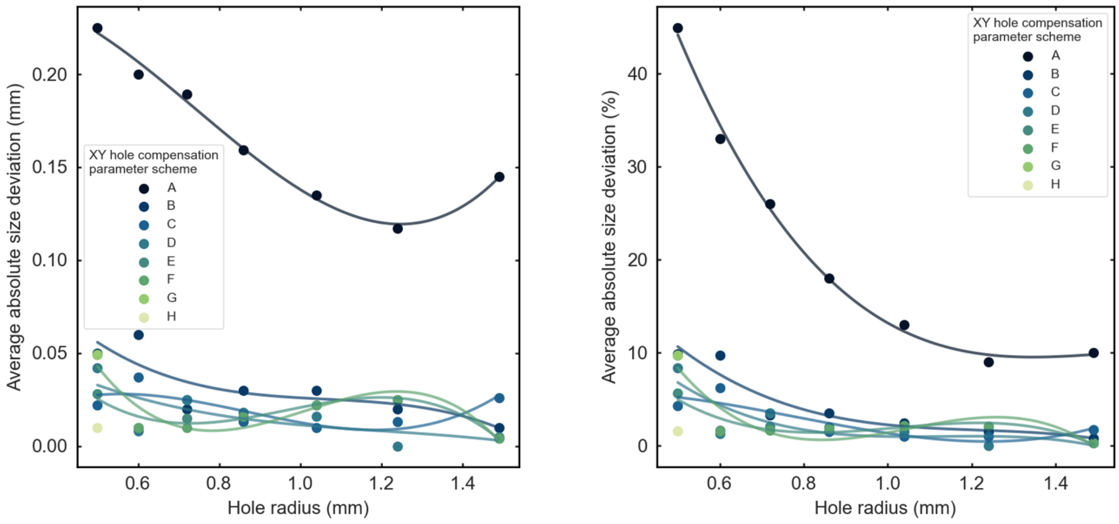

(a) Absolute deviation from target hole radius

(b) Percentage deviation from target hole radius

Figure A.2: Reduction of error in hole radius through empirical tuning of the XY hole compensation parameter. Figure A.2a shows the absolute deviation in millimeters, while Figure A.2b reports the percentage deviation. Larger holes show smaller initial errors and reach high accuracy earlier. By the final tuning iteration (scheme H), the mean error across all radii falls below 2.5%. Polynomial spline curves (order 3) are included to highlight trends and local variations.

Achieving precise dimensional accuracy required iterative adjustments to the parameter scheme. Factors such as extrusion flow, nozzle diameter, and layer height significantly influenced the outcome, limiting the direct applicability of any one scheme across different printers or print settings. The printing parameters used in this study are listed in Appendix C, except the layer height, which was set to 0.1 mm specifically for this parameter investigation. Table A.1 provides a reference framework for interpreting the tables throughout this appendix. Detailed data for each parameter scheme (from Table A.2 to Table A.9) are accompanied by corresponding stencil images (from Figure A.3a to **??**) that illustrate print quality. Each table reports deviation metrics, including standard deviation, average absolute deviation in millimeters, and average percentage deviation from the nominal value. This detailed documentation highlights the level of refinement required to achieve reliable dimensional accuracy and lays the groundwork for a robust z-pinning implementation.

Table A.1: Overview of empirical parameter study for NematX Slicer XY hole compensation parameter

Compensation scheme	**Stencil radii [mm]**	**Measurements per radius**	**Rationale for parameter selection**	**Table ref.**
A	0.5–1.49	5	No compensation (baseline)	Table A.2
B	0.5–1.49	5	Prior tests with 0.25 mm nozzle	Table A.3
C	0.5–1.49	5	Linear regression (A, B)	Table A.4
D	0.5–1.49	5	Difference (A, C)	Table A.5
E	0.5–1.49	15	Linear regression (C, D)	Table A.6
F	0.5–1.49	15	Linear regression (C, E)	Table A.7
G	0.5	35	Same as F	Table A.8
H	0.5	35	Educated guess	Table A.9

Table A.2: Summary of deviation between theoretical and printed hole radii using XY hole compensation parameter scheme A.

Theoretical	**Measured**			
radius [mm]	**STD** [-]	**avg dev [mm]**	**avg dev** [%]	**compensation parameter [mm]**
0.50	0.05	-0.225	**45.0%**	0
0.60	0.04	-0.200	**33.3%**	0
0.72	0.08	-0.189	**26.3%**	0
0.86	0.07	-0.159	**18.4%**	0
1.04	0.03	-0.135	**13.1%**	0
1.24	0.07	-0.117	**9.4%**	0
1.49	0.05	-0.145	**9.7%**	0

Table A.3: Summary of deviation between theoretical and printed hole radii using XY hole compensation parameter scheme B.

Theoretical	**Measured**			
radius [mm]	**STD** [-]	**avg dev [mm]**	**avg dev** [%]	**compensation parameter [mm]**
0.50	0.04	-0.05	**9.9%**	0.153
0.60	0.04	-0.06	**9.7%**	0.145
0.72	0.03	-0.02	**3.3%**	0.130
0.86	0.03	-0.03	**3.5%**	0.113
1.04	0.02	-0.03	**2.4%**	0.101
1.24	0.03	-0.02	**1.5%**	0.091
1.49	0.05	-0.01	**0.8%**	0.089

Table A.4: Summary of deviation between theoretical and printed hole radii using XY hole compensation parameter scheme C.

Theoretical	**Measured**			
radius [mm]	**STD** [-]	**avg dev [mm]**	**avg dev** [%]	**compensation parameter [mm]**
0.50	0.09	-0.022	**4.3%**	0.196
0.60	0.07	-0.037	**6.2%**	0.156
0.72	0.07	-0.025	**3.5%**	0.154
0.86	0.02	-0.013	**1.5%**	0.140
1.04	0.03	-0.010	**1.0%**	0.124
1.24	0.02	-0.013	**1.0%**	0.108
1.49	0.07	-0.026	**1.7%**	0.097

Table A.5: Summary of deviation between theoretical and printed hole radii using XY hole compensation parameter scheme D.

Theoretical	**Measured**			
radius [mm]	**STD [-]**	**avg dev [mm]**	**avg dev [%]**	**compensation parameter [mm]**
0.50	0.08	0.03	**6.3%**	0.234
0.60	0.16	0.04	**7.3%**	0.234
0.72	0.08	0.03	**3.9%**	0.204
0.86	0.05	0.05	**6.2%**	0.192
1.04	0.04	0.04	**4.1%**	0.175
1.24	0.10	0.02	**1.9%**	0.172
1.49	0.05	0.02	**1.6%**	0.133

Table A.6: Summary of deviation between theoretical and printed hole radii using XY hole compensation parameter scheme E.

Theoretical	**Measured**			
radius [mm]	**STD [-]**	**avg dev [mm]**	**avg dev [%]**	**compensation parameter [mm]**
0.50	0.03	0.042	**8.35%**	0.212
0.60	0.10	0.008	**1.26%**	0.192
0.72	0.06	0.025	**3.52%**	0.177
0.86	0.03	0.018	**2.03%**	0.150
1.04	0.03	0.016	**1.50%**	0.134
1.24	0.08	0.000	**0.00%**	0.126
1.49	0.08	-0.005	**0.31%**	0.116

Table A.7: Summary of deviation between theoretical and printed hole radii using XY hole compensation parameter scheme F.

Theoretical	**Measured**			
radius [mm]	**STD [-]**	**avg dev [mm]**	**avg dev [%]**	**compensation parameter [mm]**
0.50	0.07	-0.028	**5.62%**	0.201
0.60	0.12	-0.010	**1.62%**	0.184
0.72	0.05	0.015	**2.08%**	0.166
0.86	0.02	0.016	**1.84%**	0.145
1.04	0.03	0.022	**2.14%**	0.129
1.24	0.04	0.025	**2.04%**	0.125
1.49	0.09	-0.004	**0.26%**	0.114

Table A.8: Summary of deviation between theoretical and printed hole radii using XY hole compensation parameter scheme G.

Theoretical	**Measured**			
radius [mm]	**STD [-]**	**avg dev [mm]**	**avg dev [%]**	**compensation parameter [mm]**
0.50	0.09	-0.049	**9.75%**	0.2

Table A.9: Summary of deviation between theoretical and printed hole radii using XY hole compensation parameter scheme H.

Theoretical	**Measured**			
radius [mm]	**STD [-]**	**avg dev [mm]**	**avg dev [%]**	**compensation parameter [mm]**
0.50	0.05	0.01	**1.57%**	0.219

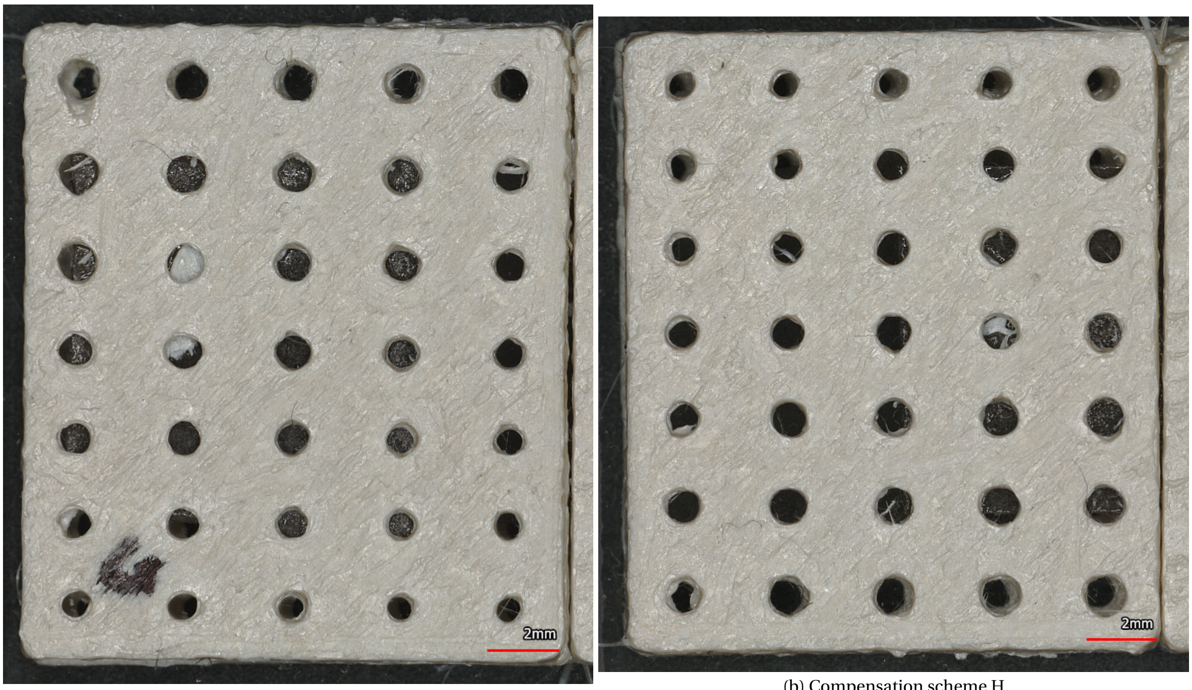

(a) Compensation scheme G

(b) Compensation scheme H

Figure A.4: Final refinement of XY hole compensation tuning for small holes (0.5 mm diameter). Schemes G and H focus on this critical radius, with scheme H representing the final adopted correction. Improved roundness and dimensional accuracy can be visually observed compared to earlier schemes.

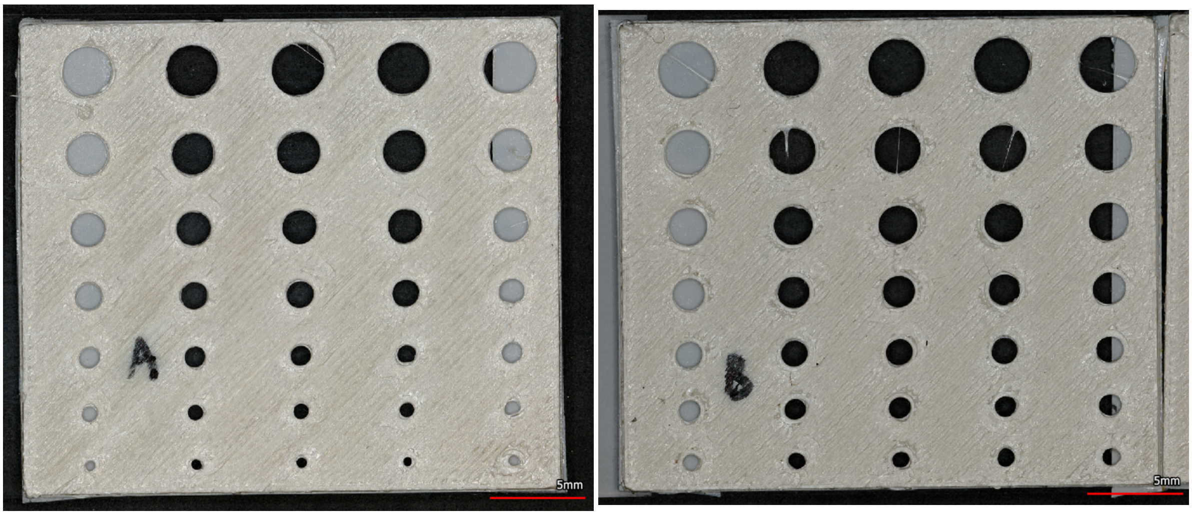

(a) Compensation scheme A

(b) Compensation scheme B

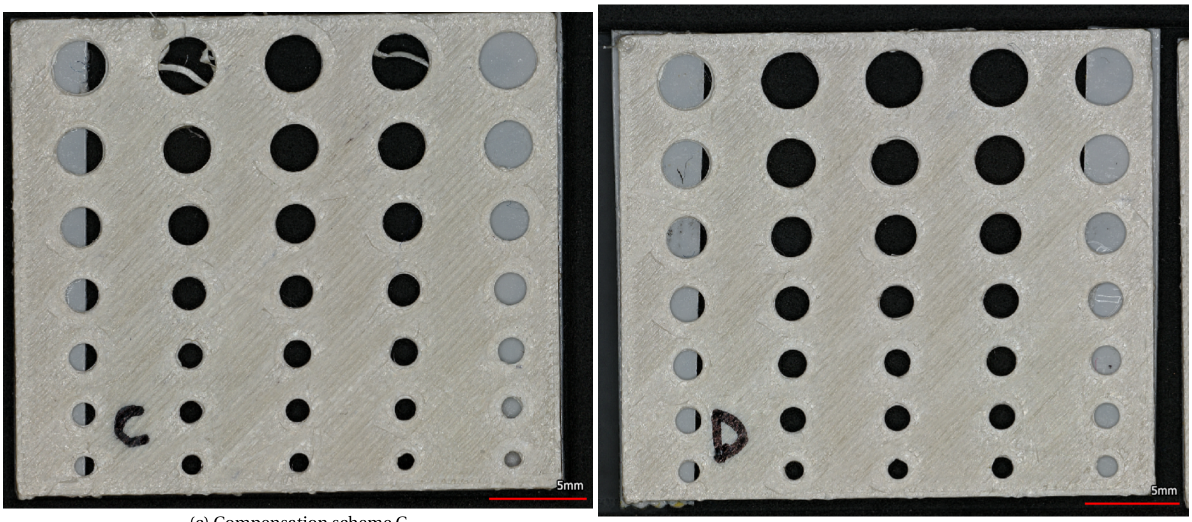

(c) Compensation scheme C

(d) Compensation scheme D

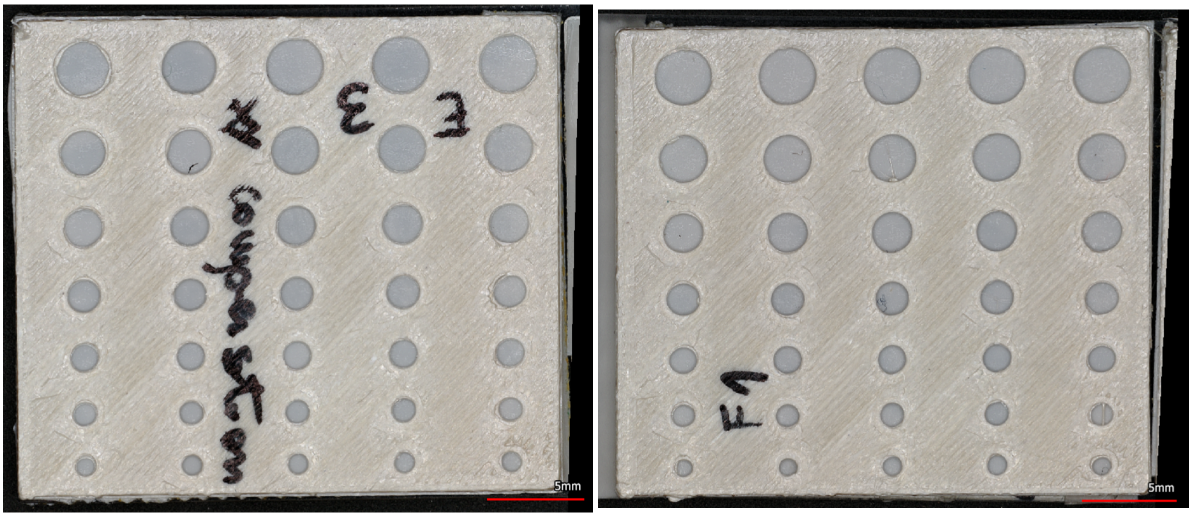

(e) Compensation scheme E

(f) Compensation scheme F

Figure A.3: Visual comparison of stencil prints resulting from different XY hole compensation parameter schemes. Each subfigure (A–F) corresponds to one compensation scheme, showing how iterative tuning affects the fidelity of circular hole reproduction. The progression from scheme A to F demonstrates improved dimensional accuracy, particularly for smaller hole diameters where deviations are most pronounced. All stencils were printed using identical geometry; only the compensation parameter was varied.

B

Pin extrusion G-code modifiers

This appendix provides additional detail on the extrusion modifiers introduced in Subsection 4.2.2. Subsection 4.2.2 presented how the progressive addition of modifiers led to the final extrusion routine. The settings of the final extrusion routine are summarized in Table B.1, along with practical notes regarding their implementation in the Python-based post-processing script. The convergence toward these final settings was the result of an iterative process involving test printing and visual evaluation of the extruded pins.

The focus of this appendix is to isolate and visualize the effect of each modifier on the extrusion progression. For each case, a range of modifier intensities is shown to highlight their influence, from minimal to aggressive settings.

Table B.1: Summary of G-code extrusion modifier parameters adopted for printing. Each modifier influences how material is distributed during pin extrusion. The settings used in this study are shown, along with implementation notes.

Extrusion modifier	**Setting**	**Notes**
Volume-normalized extrusion	enabled	The geometrical parameters describing the three pin sections need to be provided
Extrusion front-loading	200%	Each gcode line from the geometrical distribution is multiplied by 2 or divided by 2, depending on whether they are in the bottom or top half of the pin
Extrusion multiplier	1.8	The extrusion volume setting from the slicer is multiplied by this factor
Nozzle pre-depression	0.1 mm	The nozzle is sunk into the bottom of the cavity by 0.10 mm (2 layer heights) amount, and all of the following commands are shifted by this amount
Localized speeding	enabled	The extrusion commands of the bottom cone are collected in a unique g-code command with a feedrate of 100 mm/s
Pre-extrusion	disabled	Fixed extrusion length extruded at the beginning and retracted at the end of the movement

Figure B.1 illustrates how the extrusion profile changes when combining volume-normalized extrusion with various extrusion multipliers. The final strategy adopted an extrusion multiplier of 1.8, corresponding to an intermediate profile among those shown. In subsequent figures, volume-normalized extrusion with a multiplier of 1.0 is used as a baseline, as it represents the minimally altered profile. In contrast, the constant extrusion profile produced without volume normalization, also included in the plot, is suboptimal, even assuming ideal (fully elastic) material behavior.

Figure B.2 depicts the effect of nozzle pre-depression, with the adopted value of 0.10 mm (two layer heights) producing a corresponding vertical shift in the extrusion depth.

Figure B.3 and Figure B.4 show the influence of extrusion front-loading. The first example excludes retraction, while the second permits it. In the no-retraction case, extrusion halts once the forward volume is complete. Interestingly, better results were observed in this study when retraction was avoided. However, a conclusion would require a deeper understanding of the material's viscoelastic response, as the underlying mechanisms are not yet fully understood. The adopted front-loading factor was 200%, which in this case did not require retraction.

Figure B.5 shows the combined effects of localized speeding and pre-extrusion, as well as their interaction with pre-depression. Localized speeding was enabled with a feedrate of 100 mm/s. Pre-extrusion, however, was ultimately excluded from the adopted strategy. Although it ensured the complete filling of the lower pin cone, it required retraction and degraded the quality of the upper cone. The horizontal shift observed between the pre-extrusion and pre-extrusion + front-loading profiles demonstrates the compounded timing effects when multiple modifiers are used together.

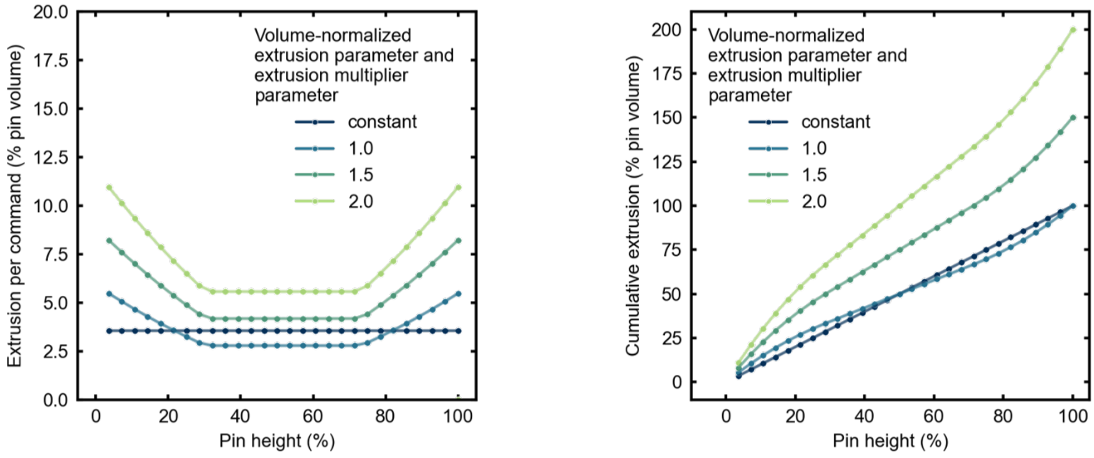

(a) Individual extrusion commands

(b) Cumulative extrusion

Figure B.1: Effect of volume-normalized extrusion parameter and extrusion multiplier on the extrusion profile. The left plot shows the individual extrusion commands as a function of pin height, while the right plot displays cumulative extrusion volume.

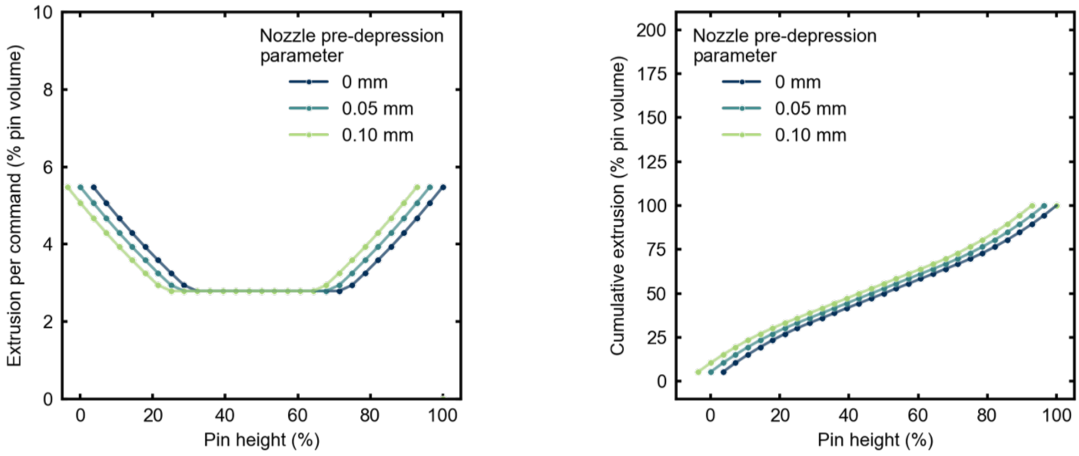

(a) Individual extrusion commands

(b) Cumulative extrusion

Figure B.2: Effect of pre-depression on the extrusion profile. The left plot shows the individual extrusion commands as a function of pin height, while the right plot displays cumulative extrusion volume.

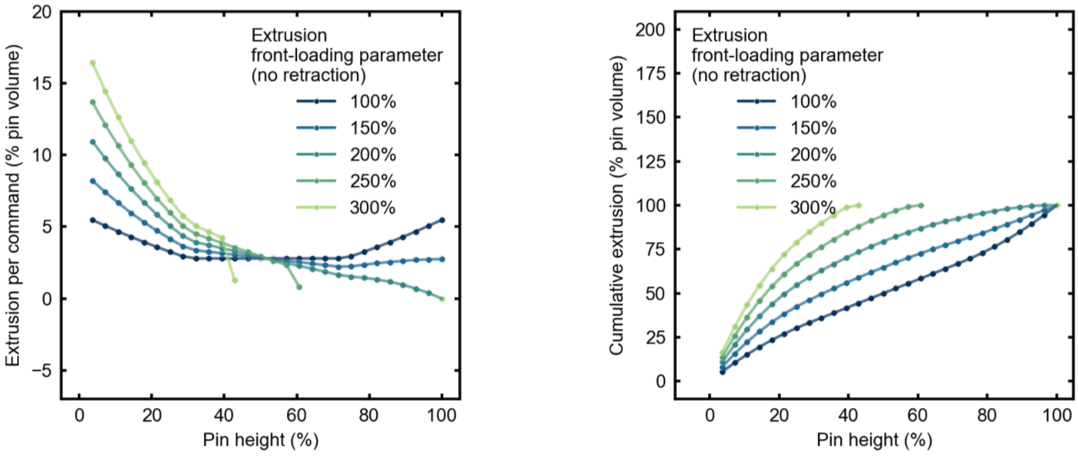

(a) Individual extrusion commands

(b) Cumulative extrusion

Figure B.3: Effect of extrusion front-loading (no retraction) on the extrusion profile. The left plot shows the individual extrusion commands as a function of pin height, while the right plot displays cumulative extrusion volume.

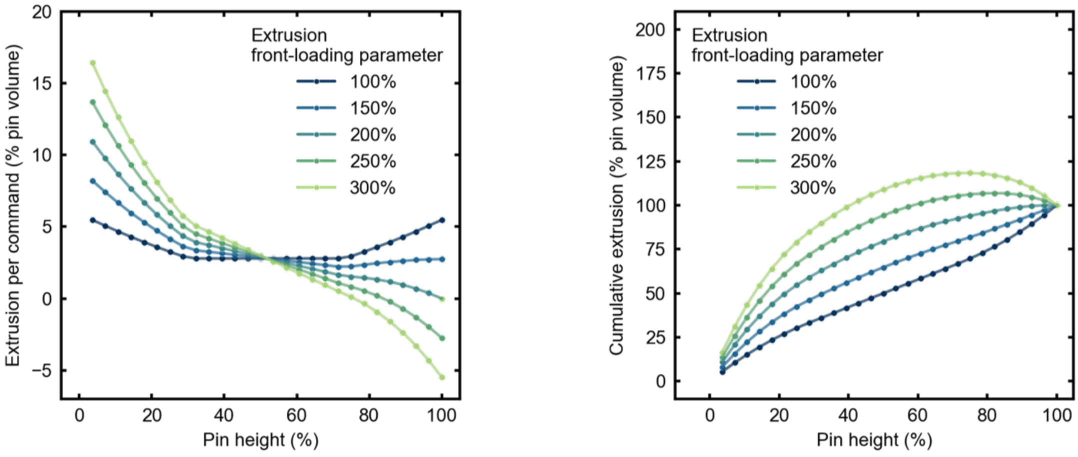

(a) Individual extrusion commands

(b) Cumulative extrusion

Figure B.4: Effect of extrusion front-loading on the extrusion profile. The left plot shows the individual extrusion commands as a function of pin height, while the right plot displays cumulative extrusion volume.

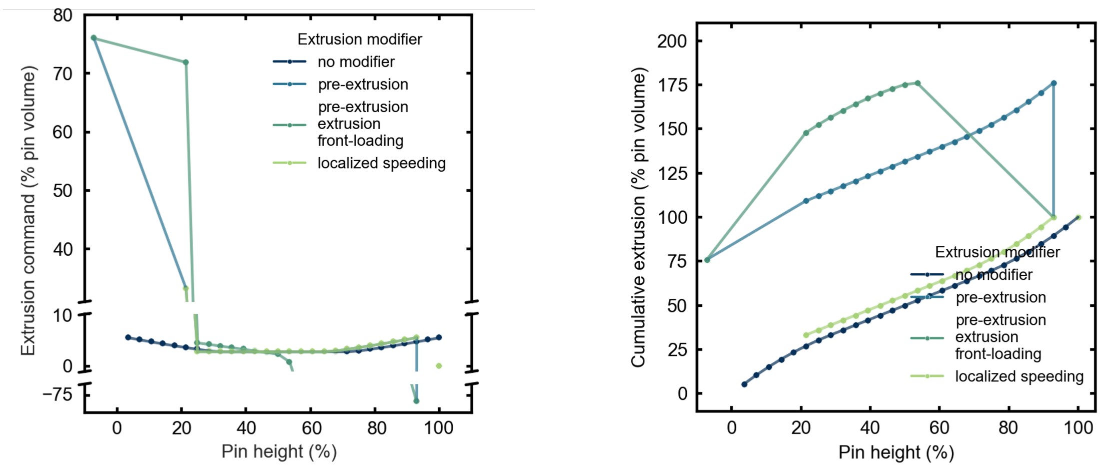

(a) Individual extrusion commands

(b) Cumulative extrusion

Figure B.5: Effect of various extrusion modifier combinations on the extrusion profile. The left plot shows the individual extrusion commands as a function of pin height, while the right plot displays cumulative extrusion volume.

This page has been intentionally left blank.

C

Complete overview of slicer settings adopted

This appendix provides all of the non-default slicer settings used on the NematX Slicer for the printing of all the LCP tensile specimens tested. These parameters were modified iteratively during the research. This overview presents the parameters selected through the tuning process conducted during the various research steps. These parameters are provided to enable the reader to understand and contextualize the decisions made, as well as to ensure the reproducibility of the results. Each parameter is discussed with its corresponding value and any relevant comments to aid in understanding and applying these settings effectively. Some of these configurations are determined by utilizing Klipper for the printing hardware. Key slicer settings are covered in **??**, specifically in the section regarding the slicer. For a more comprehensive discussion on the reasoning behind these selections, the reader is frequently directed to that section.

The settings are divided into three tables based on the NematX slicer partition of the settings. Table C.4 contains the *Printer Settings*, Table C.4 contains the *Filament Settings*, Table C.2 contains the *Print Settings*

Table C.1: Relevant parameter values for the *Filament Settings* slicer section

Category	**Parameter**	**Value**	**Comments**
Filament	Diameter	1.75 mm	-
	Density	1.4 g/cm^3	From NematX R&D
	Cost	1000 euros/kg	Current market price of NematX A950 filament
	Spool weight	239.5 g	Empty spool weight
Flow	Extrusion multiplier	0.91794	Own calibration
Temperature	Extruder (First layer)	350 °C	Constant for all layers
	Extruder (Other layers)	350 °C	See Subsection 5.1.4, paragraph on definition of printing parameters
	Bed (First layer)	110 °C	Constant for all layers
	Bed (Other layers)	110 °C	See Subsection 5.1.4, paragraph on definition of printing parameters
	Chamber	0 °C	No chamber available in the setup used
Filament properties	Filament type	LCP	-

Table C.2: Relevant parameter values for the *Filament Settings* slicer section

Category	**Parameter**	**Value**	**Comments**
Vertical shells	Contour perimeters	1	This parameter was changed for 10 when printing "reference specimens"
	Holes perimeters	1	-
Avoid crossing perimeters	Avoid crossing perimeters	Enabled	Necessary to avoid pin occlusion. See Subsection 3.3.3, paragraph on slicer
	Max detour length	2000 mm or %	High value to always enforce option
Gap Fill	Gap Fill	Enabled	-
Layer height	Base layer height	0.05 mm	Value recommended by NematX R&D
	First layer height	0.05 mm	Constant for all layers
Filtering	Slice resolution	0.0125 mm	-
	Internal resolution	0.1 mm	-
	Model rounding precision	0.0001 mm	-
	Slice gap closing radius	0.049 mm	-
XY holes curve compensation	Compensation value	Compensation curve	Find the curve parameters in Appendix A. For more info see Subsection 3.3.3
Infill	Solid infill	Rectilinear (filled), Connected	Only solid infills were used
Infill angle	Fill angle	45°	Printing common setting
Brim	Brim width	8 mm	Subjective preference
	Brim inside holes	Disabled	To visually judge pin quality from the bottom
	Brim ears max angle	125°	Subjective preference
Support material	Generate support material	Disabled	Supports were superfluous
Speed (Print moves)	Default speed	45 mm/s	See Subsection 5.1.4, paragraph on definition of printing parameters
	Perimeter speed (Internal)	100%	Same as default
	Perimeter speed (External)	100%	Same as default
	Infill speed (Solid)	100%	Same as default
Speed (Non-print moves)	Travel speed (XY/Z)	150 mm/s (XY), default (Z)	High travel speed was chosen to reduce print time but may cause part detaching when over-extrusion takes place
Modifiers	First layer speed	10 mm/s	First layer needed slower speed to attain sufficient quality
	Small perimeter speed	100%	Hole perimeters were printed slower to improve extrusion consistency
Extrusion width	Default width	0.2 mm	Default equal to nozzle diameter
	Perimeter width	100%	Same as default
	External perimeter width	100%	Same as default
	Solid infill width	100%	Same as default
Overlap	Perimeter overlap	100%	-

Category	Parameter	Value	Comments
Output file	Label objects	Firmware-specific	Necessary for Klipper's feature of interrupting the printing of a specific part on the print plate
Sequential printing	Extruder clearance radius/height	x:60 mm, y:95 mm	Related to the specific setup with Hemera and nozzle camera mount

Table C.4: Relevant parameter values for the *Printer Settings* slicer section

Category	Parameter	Value	Comments
Size and Coordinates	Max print height	210 mm	Reduced maximum height due to positioning of hemera extruder
	Bed shape	x:173mm; y:186mm	Reduced bed size due to positioning of hemera extruder
Firmware	G-code flavor	Klipper	-
Custom G-code commands	Only custom Start G-code	Enabled	Custom g-code is used to interact with Klipper
	Emit temperature commands automatically	Disabled	Temperature commands handled through the START_PRINT Klipper macro
	Start G-code	"SET_PRINT_STATS_INFO TOTAL_LAYER=[total_layer_count]" "START_PRINT EXTRUDER=[first_layer_temperature] BED=[first_layer_bed_temperature]" "M117 Print"	Executes the START_PRINT Klipper macro. See **??**
	End G-code	"END_PRINT" "M117 Print completed"	Executes the END_PRNIT Klipper macro. See **??**
	Before layer change	";BEFORE_LAYER_CHANGE" "M117 layer_num of [total_layer_count]"	Displays layer number on the UI
	After layer change	"SET_PRINT_STATS_INFO CURRENT_LAYER=layer_num + 1"	Updates print stats displayed on theUI

D

Tensile test data

This appendix provides a comprehensive overview of the most valuable results obtained from tensile testing. These results are provided to ensure transparency in their interpretation and to facilitate their reproducibility. In this appendix, the data is reported and not discussed as the interpretation of the test data belongs to Chapter 5 and Appendix E. Zwick-setup test results are reported extensively, while the Instron-setup test results are reported in less detail due to the quality of the data collection .

Figure D.1 is provided as a guide to navigate the appendix and understand the specimen codes used, connecting them to pin architecture denominations used in Chapter 5. Pin architectures distinguish themselves by pin size and pin staggering order. For more detailed information on how these geometries were chosen, manufactured, and tested, the reader is referred to Chapter 5.

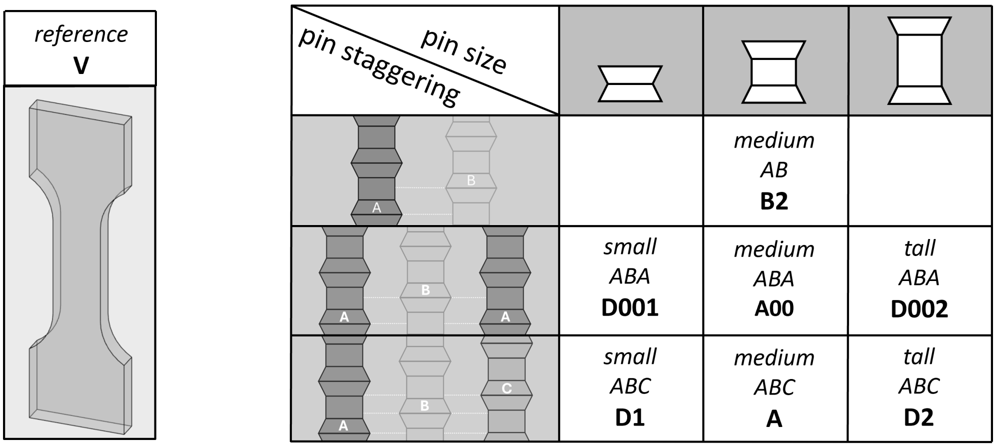

(a) Reference specimen

(b) Pinned specimens

Figure D.1: Overview of design and testing denominations for the tensile specimens. (a) identifies the reference specimen, printed with regular solid infill. (b) explains the pin configuration obtained with combinations of pin staggering orders and pin sizes.

The appendix is divided into five subsections. The initial three sections focus on the specimens examined using the Zwick setup. Section D.4 focuses on the results acquired with the Instron setup, whereas Section D.5 showcases images of the fracture patterns observed during the tests. Section D.1 is dedicated to the reference specimen, Section D.2 to the single specimen design with two pin columns and Section D.3 to the six specimen designs with three pin columns. Each specimen design test data is reported in two forms: load-displacement graphs and a table with the numbers of certain testing analytics. These analytics are: maximum load ($F_{\max}$), nominal displacement (ΔL) at $\mathbf{F}_{\max}$, rigidity, work done on the specimen (W) before and after maximum load. Furthermore, the batch mean and standard deviation (STD) are calculated at the bottom of each table. The results from testing with the Instron setup are reported with fewer analytics, as they were not used for the analysis.

D.1. Reference specimen

This section contains testing data relative to the V specimen configuration (reference). Figure D.3 illustrates the relative load-displacement curves while the exact values of the relevant testing analytics are found in Table D.2.

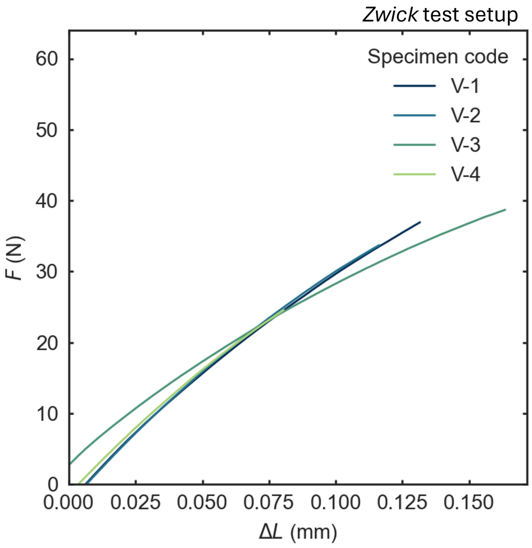

Figure D.2: Load-displacement curve of the tensile tests of V specimens (reference) tested with the Zwick test setup.

Table D.1: Mechanical response of V specimens (reference, unpinned) under tensile loading on the Zwick setup. The table includes fracture and peak loads, displacements, rigidity, and energy-related quantities.

Specimen code	**F_{max} (N)**	**ΔL at F_{max} (10^{-3} mm)**	**Rigidity (N/mm)**	**W before F_{max} (N·mm)**	**W after F_{max} (N·mm)**	**$\Delta L_{end\ of\ test}$ (10^{-3} mm)**
V-1	36.93	131.6	400.8	2.547	0.000	131.6
V-2	33.70	116.4	395.5	2.034	0.000	116.4
V-3	38.68	163.5	332.4	3.820	0.000	163.5
V-4	24.55	80.45	383.9	1.010	0.000	80.45
Batch mean	33.47	122.9	378.2	2.353	0.000	122.9
STD	6.292	35.23	31.29	1.168	0.000	35.23

D.2. Two-pin columns specimen configuration

This section contains testing data relative to the B2 specimen configuration (medium AB). Figure D.3 illustrates the relative load-displacement curves while the exact values of the relevant testing analytics are found in Table D.2.

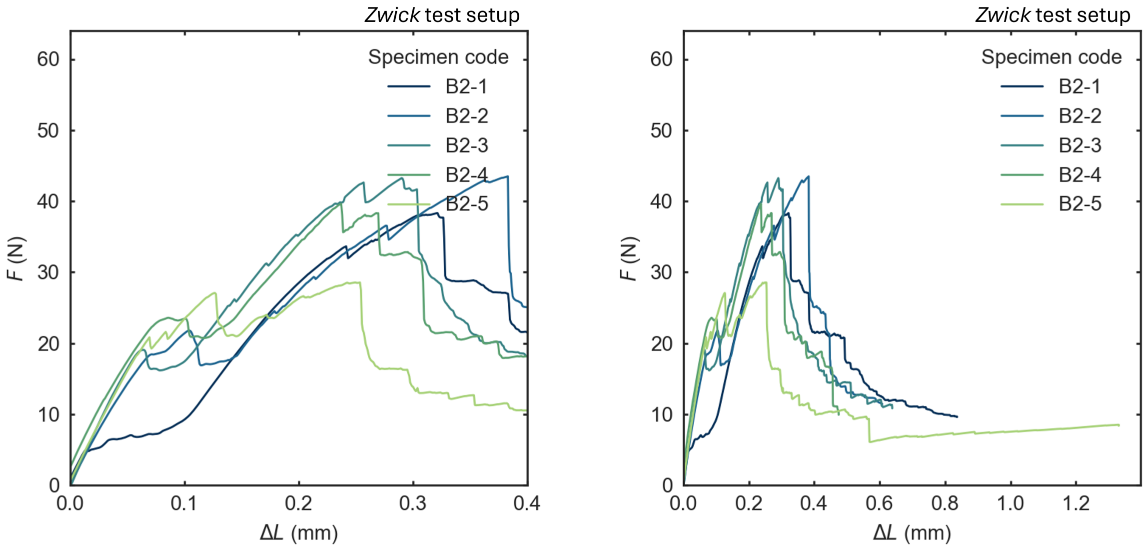

(a) Narrowed displacement axis

(b) Complete displacement axis

Figure D.3: Load-displacement curves of the tensile tests of B2 specimens (medium AB) tested with the Zwick test setup. (a) shows a limited portion of the ΔL axis to better portray the data around the F_{max}, while (a) shows the entire span of the displacement data.

Table D.2: Mechanical response of B2 specimens (medium AB) under tensile loading on the Zwick setup. The table includes fracture and peak loads, displacements, rigidity, and energy-related quantities.

Specimen code	F_{fracture} **(N)**	**ΔL at** F_{fracture} **(10^{-3} mm)**	$\mathbf{F_{max}}$ **(N)**	**ΔL at** $\mathbf{F_{max}}$ **(10^{-3} mm)**	**Rigidity (N/mm)**	**W before** $\mathbf{F_{max}}$ **(N·mm)**	**W after** $\mathbf{F_{max}}$ **(N·mm)**	$\mathbf{\Delta L_{end\ of\ test}}$ **(10^{-3} mm)**
B2-1	6.476	38.19	38.30	321.5	239.1	6.712	8.358	836.8
B2-2	18.41	71.59	43.48	382.9	313.1	10.09	3.705	608.0
B2-3	19.04	63.65	43.24	289.9	359.0	7.567	6.016	638.4
B2-4	23.56	86.18	39.60	237.2	334.5	5.557	5.522	474.6
B2-5	20.82	69.39	28.54	249.4	322.4	5.176	9.597	1331
Batch mean	17.66	64.83	38.63	296.2	313.6	7.020	6.640	779.0
STD	6.564	18.91	6.076	56.85	45.06	1.960	2.343	334.4

D.3. Three-pin columns specimens

This section contains testing data related to the specimen configurations with three-pin columns.

D.3.1. Double staggering order pin architectures (ABA)

This subsection contains testing data related to the specimen configuration subset with three-pin columns featuring a double-pin staggered order.

Short pin ABA

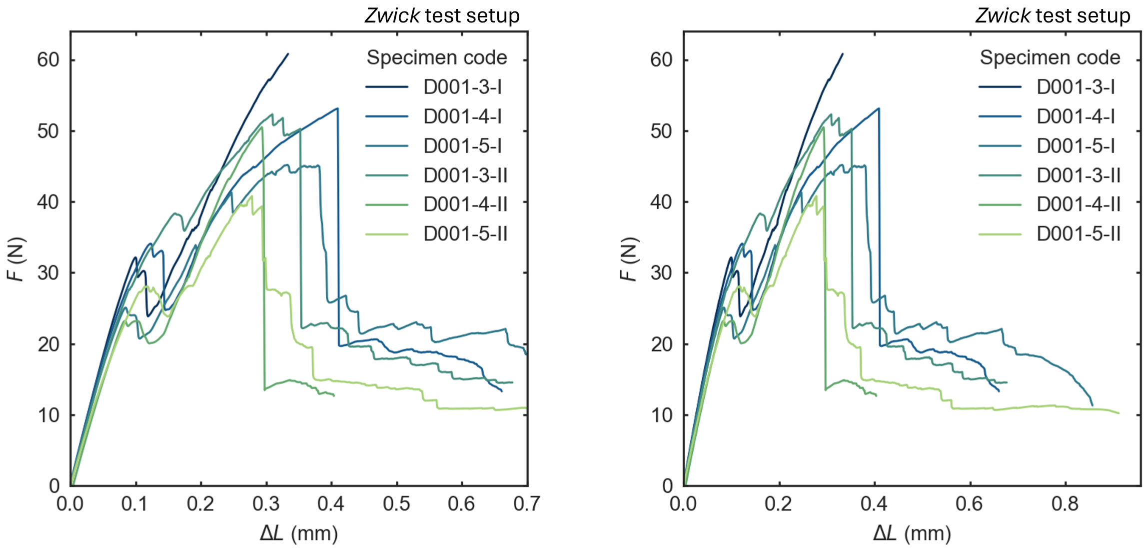

(a) Narrowed displacement axis

(b) Complete displacement axis

Figure D.4: Load-displacement curves of the tensile tests of D001 specimens (short ABA) tested with the Zwick test setup. (a) shows a limited portion of the ΔL axis to better portray the data around the $F_{\max}$, while (a) shows the entire span of the displacement data.

Table D.3: Mechanical response of D001 specimens (short ABA) under tensile loading on the Zwick setup. The table includes fracture and peak loads, displacements, rigidity, and energy-related quantities.

Specimen code	**F_{fracture} (N)**	**ΔL at F_{fracture} (10^{-3} mm)**	**F_{max} (N)**	**ΔL at F_{max} (10^{-3} mm)**	**Rigidity (N/mm)**	**W before F_{max} (N·mm)**	**W after F_{max} (N·mm)**	**$\Delta L_{\text{end of test}}$ (10^{-3} mm)**
D001-3-I	32.12	99.67	60.80	333.6	373.7	11.56	0.000	333.6
D001-4-I	34.08	123.4	53.12	409.6	362.2	14.35	4.654	659.4
D001-5-I	25.07	84.70	45.17	332.6	354.3	9.623	11.97	856.9
D001-3-II	27.64	90.33	52.28	309.7	345.2	10.31	8.020	676.8
D001-4-II	23.19	83.90	50.47	293.6	341.4	7.897	1.650	403.9
D001-5-II	27.28	106.6	40.78	278.4	313.9	6.963	8.967	911.2
Batch mean	26.04	93.59	47.85	294.0	333.5	8.389	6.212	664.2
STD	2.472	11.68	6.183	15.66	17.09	1.726	3.980	253.9

Medium pin ABA

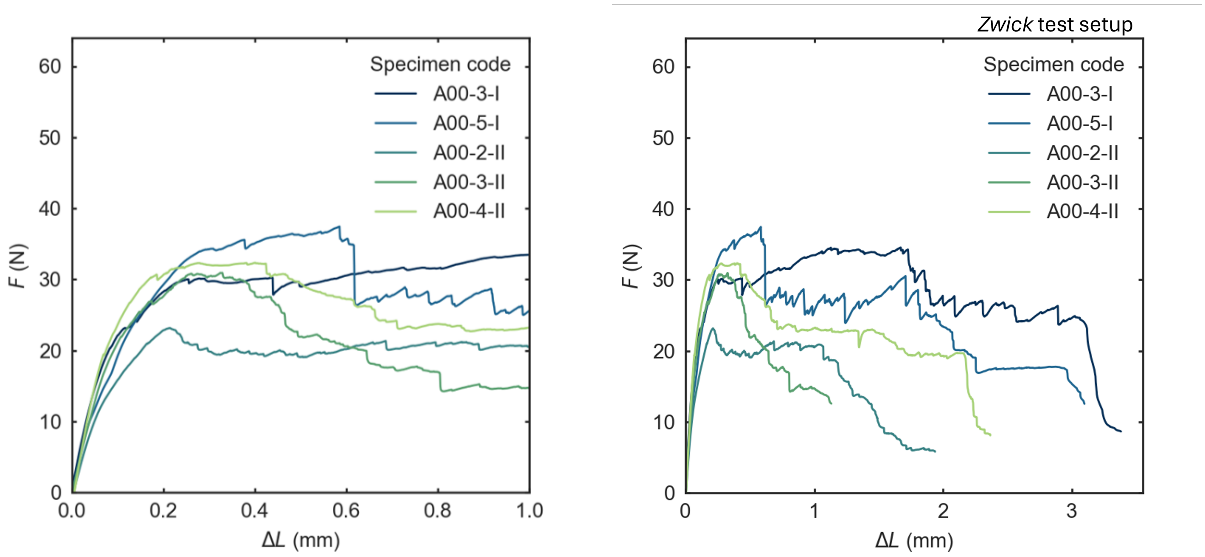

(a) Narrowed displacement axis

(b) Complete displacement axis

Figure D.5: Load-displacement curves of the tensile tests of A00 specimens (medium AB) tested with the Zwick test setup. (a) shows a limited portion of the ΔL axis to better portray the data around the F_{max}, while (a) shows the entire span of the displacement data.

Table D.4: Mechanical response of A00 specimens (medium ABA) under tensile loading on the Zwick setup. The table includes fracture and peak loads, displacements, rigidity, and energy-related quantities.

Specimen code	**F_{fracture} (N)**	**ΔL at F_{fracture} (10^{-3} mm)**	**F_{max} (N)**	**ΔL at F_{max} (10^{-3} mm)**	**Rigidity (N/mm)**	**W before F_{max} (N·mm)**	**W after F_{max} (N·mm)**	**$\Delta L_{\text{end of test}}$ (10^{-3} mm)**
A00-3-I	20.31	83.03	34.52	1670	322.4	51.24	41.66	3380
A00-5-I	33.93	279.9	37.43	585.2	309.0	17.00	57.99	3097
A00-2-II	20.94	164.0	23.14	212.8	260.9	3.177	27.04	1937
A00-3-II	21.91	106.9	30.91	324.4	305.1	7.436	15.36	1132
A00-4-II	19.44	69.12	32.33	400.9	382.1	10.58	42.28	2366
Batch mean	23.31	140.8	31.66	638.8	315.9	17.89	36.87	2383
STD	6.004	86.44	5.360	592.9	43.64	19.31	16.26	904.4

Tall pin ABA

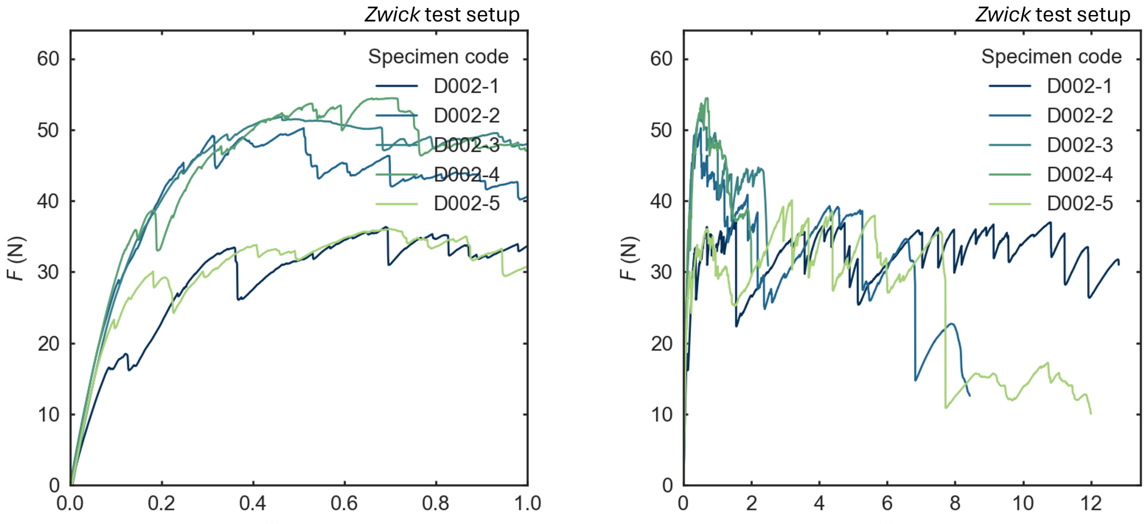

(a) Narrow displacement axis till 1 mm

(b) Narrow displacement axis till 13 mm

Figure D.6: Partial Load-displacement curves of the tensile tests of D002 specimens (tall ABA) tested with the Zwick test setup. (a) and (b) show a limited portion of the ΔL axis to better portray the data around the F_{max} of the different test specimens, while Figure D.7 shows the entire span of the displacement data.

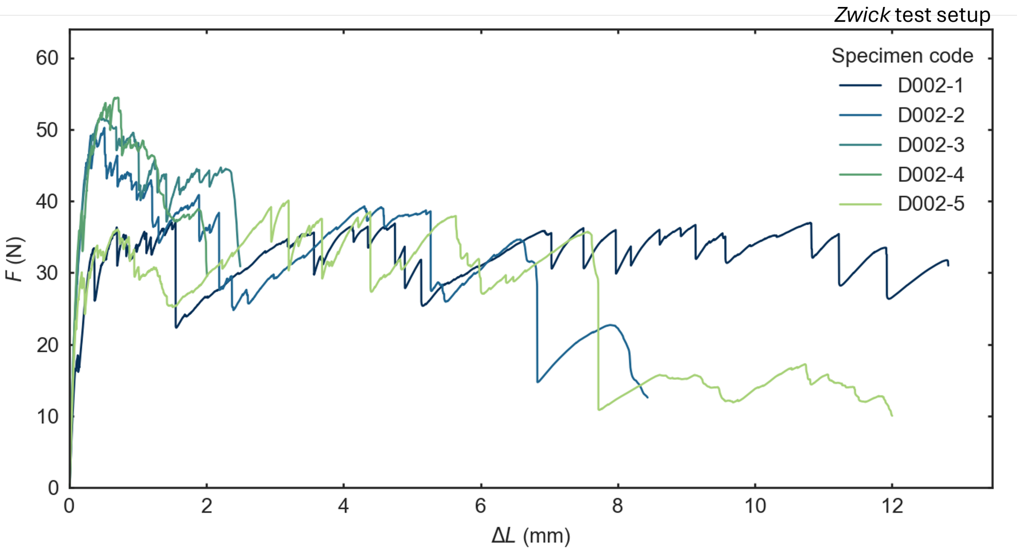

Figure D.7: Complete Load-displacement curve of the tensile tests of D002 specimens (tall ABA) tested with the Zwick test setup.

Table D.5: Mechanical response of D002 specimens (tall ABA) under tensile loading on the Zwick setup. The table includes fracture and peak loads, displacements, rigidity, and energy-related quantities.

Specimen code	F_{fracture} **(N)**	**ΔL at** F_{fracture} **(10^{-3} mm)**	$\mathbf{F_{max}}$ **(N)**	**ΔL at** $\mathbf{F_{max}}$ **(10^{-3} mm)**	**Rigidity (N/mm)**	**W before** $\mathbf{F_{max}}$ **(N·mm)**	**W after** $\mathbf{F_{max}}$ **(N·mm)**	$\mathbf{\Delta L_{end\ of\ test}}$ **(10^{-3} mm)**
D002-1	16.54	85.54	37.00	1495	240.2	45.77	366.5	12 820
D002-2	28.85	106.0	50.24	510.7	332.1	19.60	248.3	8436
D002-3	34.77	147.9	51.81	462.5	343.7	17.31	89.91	2492
D002-4	33.82	125.8	54.43	704.1	338.7	29.91	55.29	2009
D002-5	23.28	95.87	40.07	3195	336.6	99.59	208.5	11 990
Batch mean	27.45	114.1	46.71	1273	318.3	42.43	193.7	7549
STD	7.625	25.45	7.690	1149	43.82	33.86	125.5	5115

D.3.2. Triple staggering order pin architectures (ABC)

This subsection contains testing data relative to the subset of specimen configurations with three-pin columns that have a triple-pin staggering order.

Short pin ABC

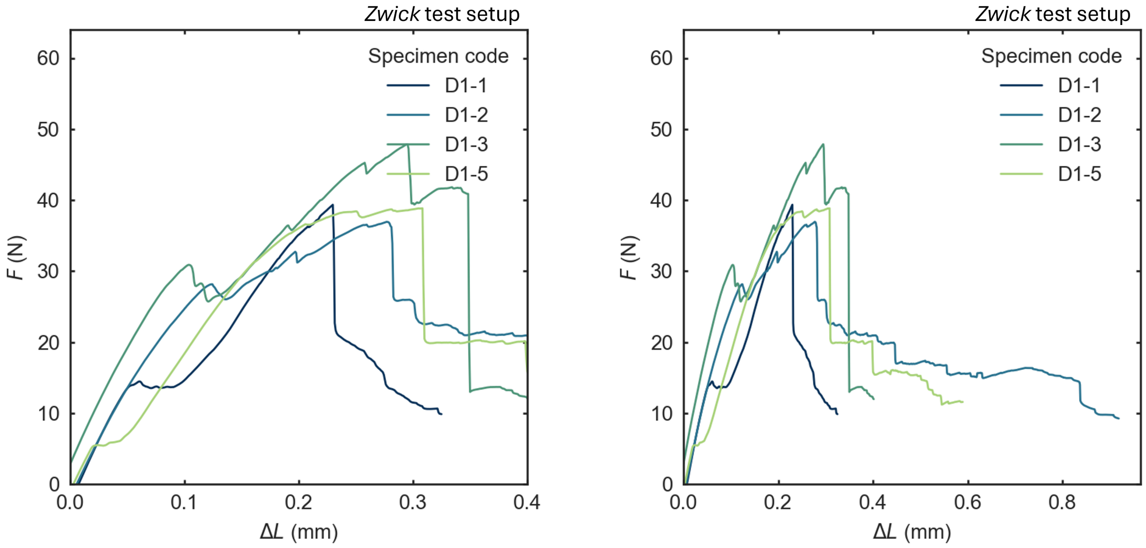

(a) Narrowed displacement axis

(b) Complete displacement axis

Figure D.8: Load-displacement curves of the tensile tests of D1 specimens (short ABC) tested with the Zwick test setup. (a) shows a limited portion of the ΔL axis to better portray the data around the F_{max}, while (a) shows the entire span of the displacement data.

Table D.6: Mechanical response of D1 specimens (short ABC) under tensile loading on the Zwick setup. The table includes fracture and peak loads, displacements, rigidity, and energy-related quantities.

Specimen code	**F_{fracture} (N)**	**ΔL at F_{fracture} (10^{-3} mm)**	**F_{max} (N)**	**ΔL at F_{max} (10^{-3} mm)**	**Rigidity (N/mm)**	**W before F_{max} (N·mm)**	**W after F_{max} (N·mm)**	**$\Delta L_{\text{end of test}}$ (10^{-3} mm)**
D1-1	14.46	60.65	39.34	229.8	353.7	4.558	1.458	324.9
D1-2	28.14	123.7	36.94	276.0	329.9	6.798	10.81	917.0
D1-3	30.87	103.5	47.85	295.3	356.6	9.025	2.904	401.7
D1-5	5.496	24.09	38.84	308.3	317.7	7.811	4.520	589.4
Batch mean	19.74	77.98	40.74	277.6	339.5	7.048	4.922	558.6
STD	11.90	44.83	4.848	33.08	18.78	1.893	4.118	266.0

Medium pin ABC

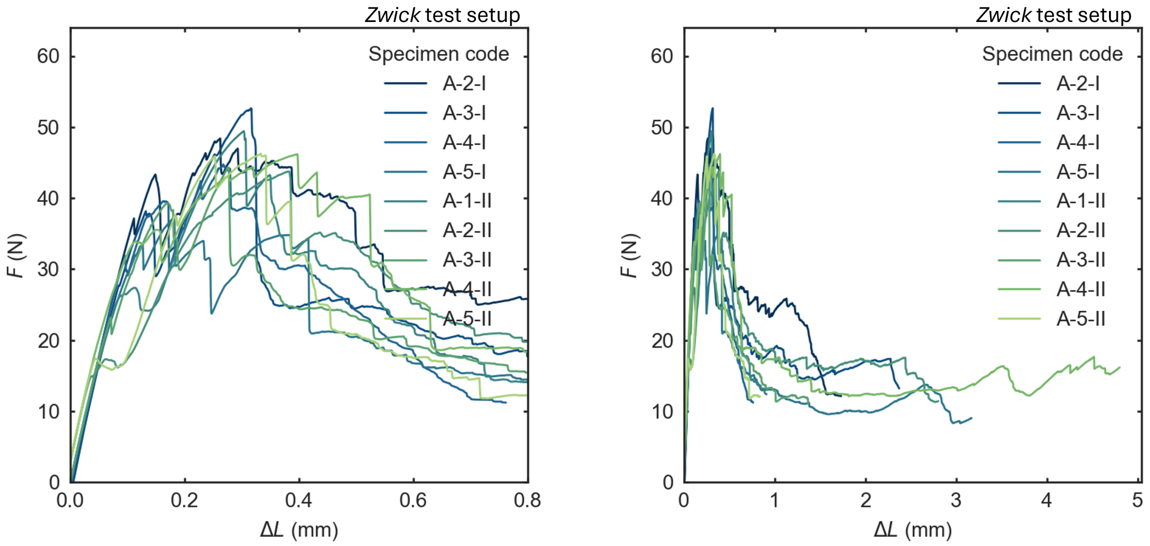

(a) Narrowed displacement axis

(b) Complete displacement axis

Figure D.9: Load-displacement curves of the tensile tests of A specimens (medium ABC) tested with the Zwick test setup. (a) shows a limited portion of the ΔL axis to better portray the data around the F_{max}, while (a) shows the entire span of the displacement data.

Table D.7: Mechanical response of A specimens (medium ABC) under tensile loading on the Zwick setup. The table includes fracture and peak loads, displacements, rigidity, and energy-related quantities.

Specimen code	**F_{fracture} (N)**	**ΔL at F_{fracture} (10^{-3} mm)**	**F_{max} (N)**	**ΔL at F_{max} (10^{-3} mm)**	**Rigidity (N/mm)**	**W before F_{max} (N·mm)**	**W after F_{max} (N·mm)**	**$\Delta L_{\text{end of test}}$ (10^{-3} mm)**
A-2-I	37.13	111.4	48.39	262.3	405.1	8.291	37.42	1.7317
A-3-I	27.66	84.44	52.64	316.2	394.4	10.33	36.93	2.3716
A-4-I	31.84	95.99	44.73	267.6	405.4	8.020	11.63	0.7619
A-5-I	29.23	99.45	37.30	181.6	358.8	4.329	38.22	2.9357
A-1-II	26.53	94.43	49.42	303.4	356.7	8.903	14.11	0.9105
A-2-II	14.90	37.70	43.73	382.3	368.0	11.21	44.25	2.8025
A-3-II	23.16	70.45	44.30	277.2	366.8	7.966	18.60	1.3665
A-4-II	33.88	114.5	46.17	397.5	379.9	13.81	67.76	4.8032
A-5-II	17.39	44.54	46.24	333.1	370.5	10.14	10.20	0.8356
Batches mean	26.86	83.53	45.88	302.3	366.3	9.445	31.01	2.0558
STD	7.352	25.55	4.284	68.13	43.27	2.622	19.05	1.3228

Tall pin ABC

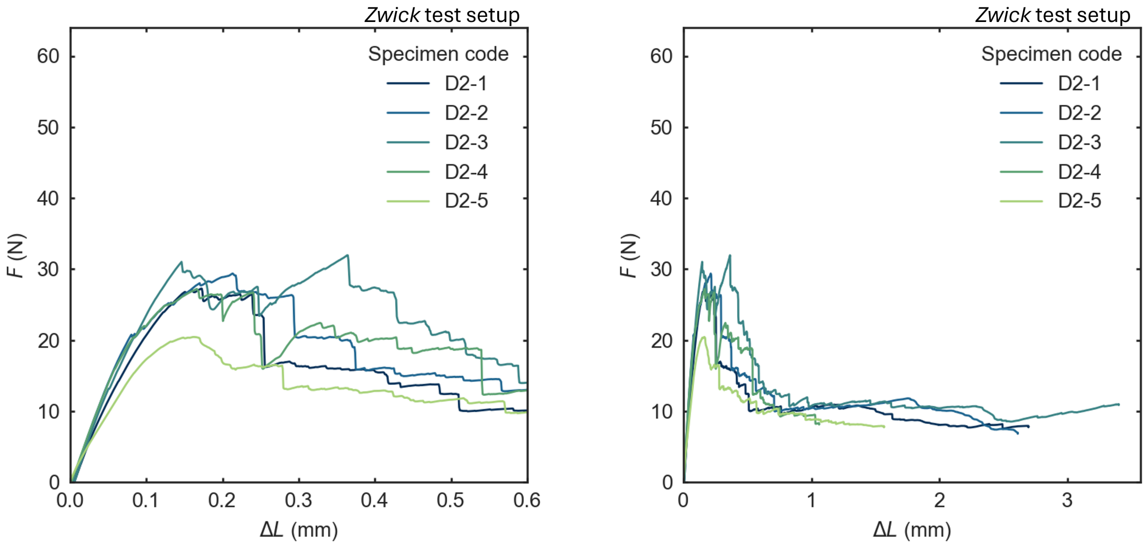

(a) Narrowed displacement axis

(b) Complete displacement axis

Figure D.10: Load-displacement curves of the tensile tests of D2 specimens (tall ABC) tested with the Zwick test setup. (a) shows a limited portion of the ΔL axis to better portray the data around the $F_{\max}$, while (a) shows the entire span of the displacement data.

Table D.8: Mechanical response of D2 specimens (short ABC) under tensile loading on the Zwick setup. The table includes fracture and peak loads, displacements, rigidity, and energy-related quantities.

Specimen code	F_{fracture} **(N)**	**ΔL at** F_{fracture} **(10^{-3} mm)**	**$\mathrm{F_{max}}$ (N)**	**ΔL at $\mathrm{F_{max}}$ (10^{-3} mm)**	**Rigidity (N/mm)**	**W before $\mathrm{F_{max}}$ (N·mm)**	**W after $\mathrm{F_{max}}$ (N·mm)**	**$\Delta\mathrm{L_{end\ of\ test}}$ (10^{-3} mm)**
D2-1	26.77	150.4	27.26	171.9	299.8	2.878	26.21	2696
D2-2	20.76	80.41	29.37	213.1	329.9	4.291	27.38	2582
D2-3	13.16	50.35	31.94	363.6	330.3	8.508	34.57	3402
D2-4	20.39	83.60	27.20	166.1	321.3	2.940	13.11	1060
D2-5	19.78	131.9	20.43	161.8	227.9	2.153	14.42	1568
Batch mean	20.97	99.33	27.24	215.3	301.8	4.154	23.14	2261
STD	4.832	40.93	4.272	85.65	43.16	2.554	9.148	938.6

D.4. Specimens tested with the Instron test setup.

This section contains testing data relative to V (reference), unpinned A (unpinned medium ABC) and A (medium ABC) specimen configurations tested with the Instron setup.

D.4.1. Reference and Unpinned specimens

Figure D.11 and Figure D.12 each show load-displacement curves for the V (reference) and the unpinned A (unpinned medium ABC) specimens. The $\mathbf{F}_{\max}$ and $\Delta\mathbf{L}$ are found in Table D.9 and Table D.10.

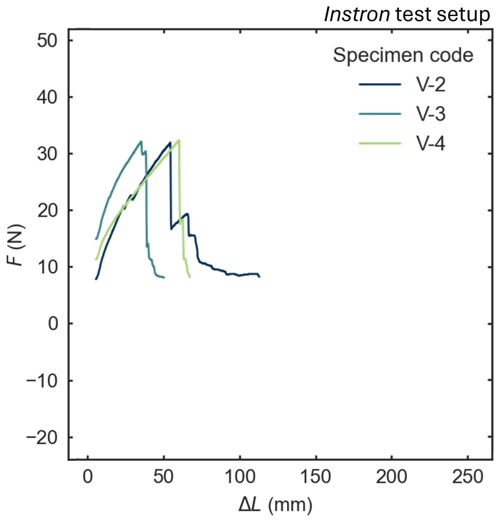

Figure D.11: Load-displacement curves of the tensile test results of V specimens (reference) tested with the Instron test setup.

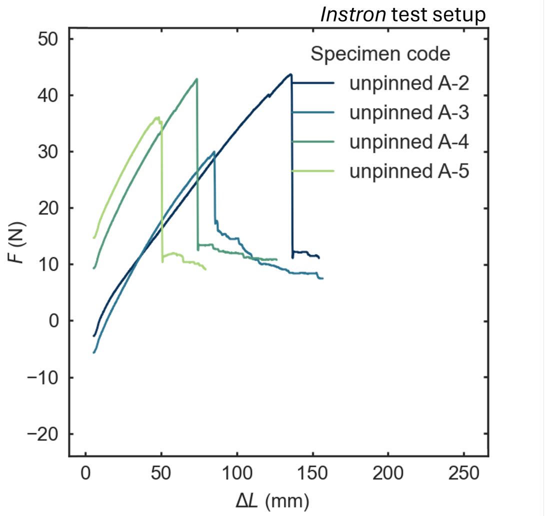

Figure D.12: Load-displacement curves of the tensile test results of unpinned A specimens (unpinned medium ABC) tested with the Instron test setup.

Table D.9: [Mechanical response of V specimens (reference, unpinned) under tensile loading on the Instron setup, showing peak load and corresponding displacement.

Specimen code	$\mathbf{F}_{\max}$ **(N)**	$\Delta\mathbf{L}$ **at** $\mathbf{F}_{\max}$ **(mm)**
V-2	31.90	50.05
V-3	32.10	3.027
V-4	32.30	55.78
Batch mean	32.10	36.29
STD	0.2000	28.94

Table D.10: Mechanical response of unpinned A specimens (medium ABC) under tensile loading on the Instron setup, listing maximum load and displacement at failure.

Specimen code	$\mathbf{F}_{\max}$ **(N)**	$\Delta\mathbf{L}$ **at** $\mathbf{F}_{\max}$ **(mm)**
Unpinned A-2	43.68	132.7
Unpinned A-3	30.00	81.40
Unpinned A-4	42.88	69.62
Unpinned A-5	36.10	43.89
Batch mean	38.16	81.90
STD	6.420	37.31

D.4.2. Medium pin ABC

Figure D.13 illustrates the relative load-displacement curves while the exact values of the relevant testing analytics are found in Table D.11.

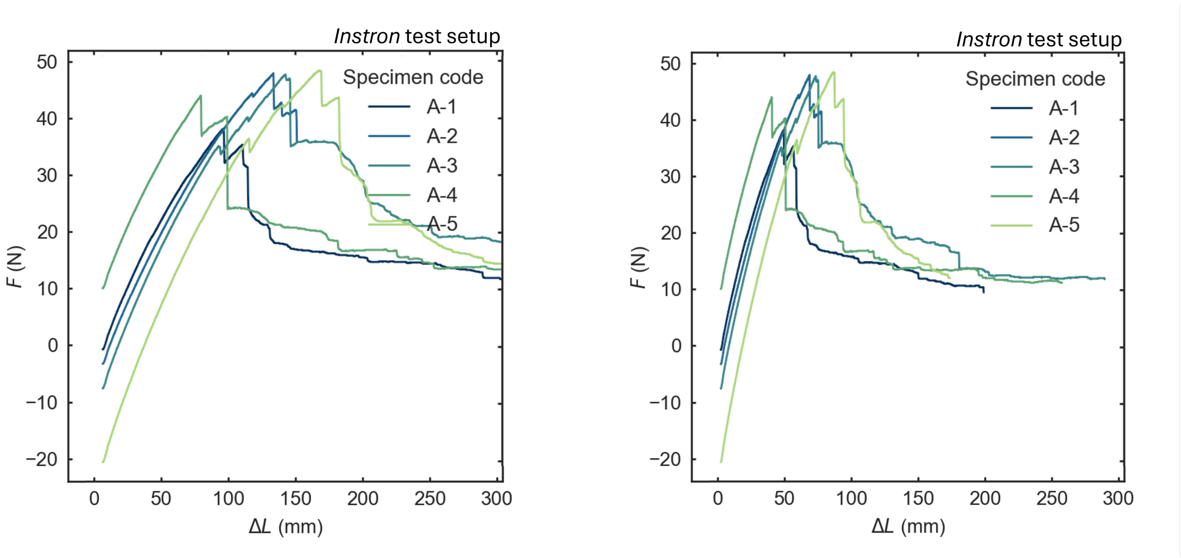

(a) Narrowed displacement axis

(b) Complete displacement axis

Figure D.13: Load-displacement curves of the tensile tests of A specimens (medium ABC) tested with the Instron test setup. (a) shows a limited portion of the ΔL axis to better portray the data around the F_{max}, while (a) shows the entire span of the displacement data.

Table D.11: Mechanical response of A specimens (medium ABC) under tensile loading on the Instron setup, reporting peak force and displacement.

Specimen code	**F_{max} (N)**	**ΔL at F_{max} (mm)**
A-1	38.10	91.77
A-2	47.80	129.9
A-3	47.60	139.2
A-4	43.92	74.78
A-5	48.32	163.4
Batch mean	45.15	119.8
STD	4.308	36.02

D.5. Specimen fractures patterns

This section presents an image depicting the fracture pattern for each specimen configuration tested using the Zwick setup. These fractures are termed patterns due to their repetitive nature within the same batch, suggesting a causation between the design and the fracture pattern.

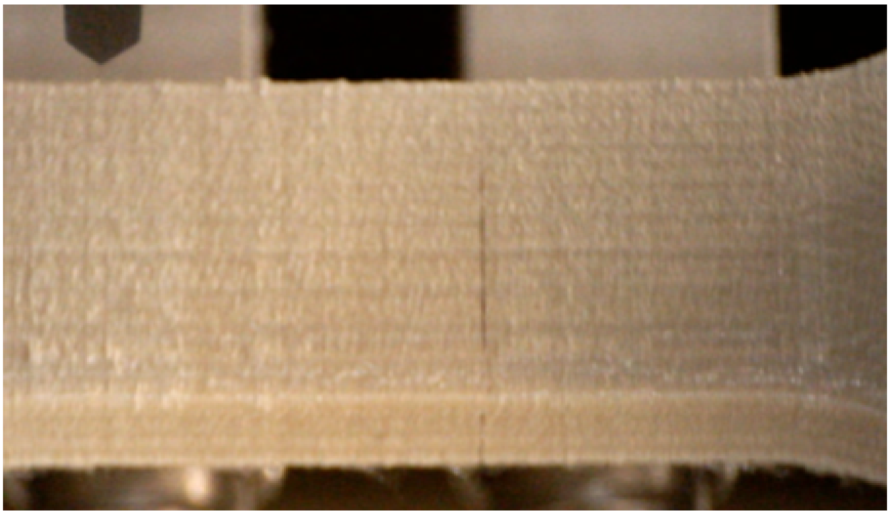

Figure D.14: Example of fracture in a V specimen (reference) tested with the Zwick setup.

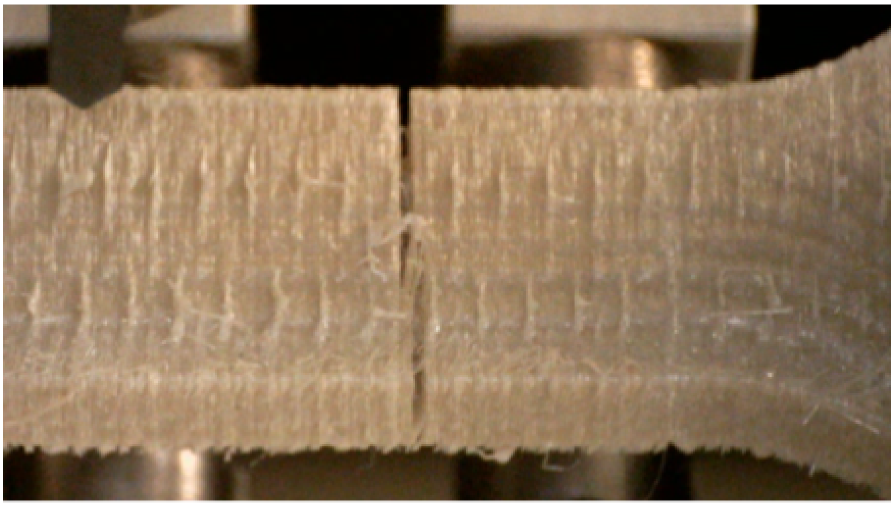

Figure D.15: Example of fracture in a B2 specimen (medium AB) tested with the Zwick setup.

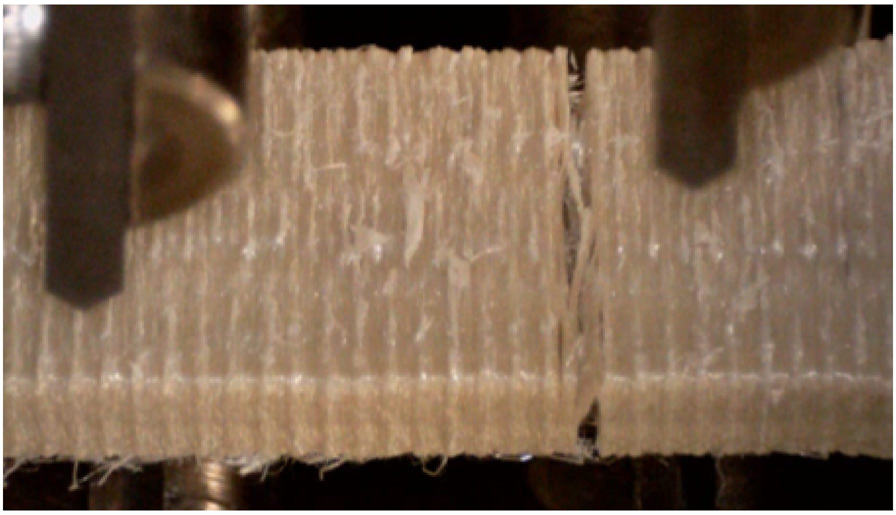

Figure D.16: Example of fracture in a D001 specimen (short ABA) tested with the Zwick setup.

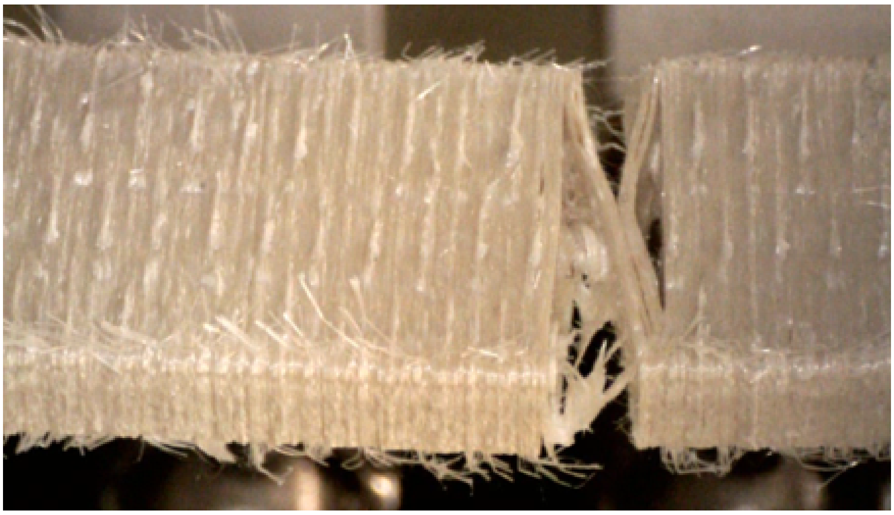

Figure D.17: Example of fracture in an A00 specimen (medium ABA) tested with the Zwick setup.

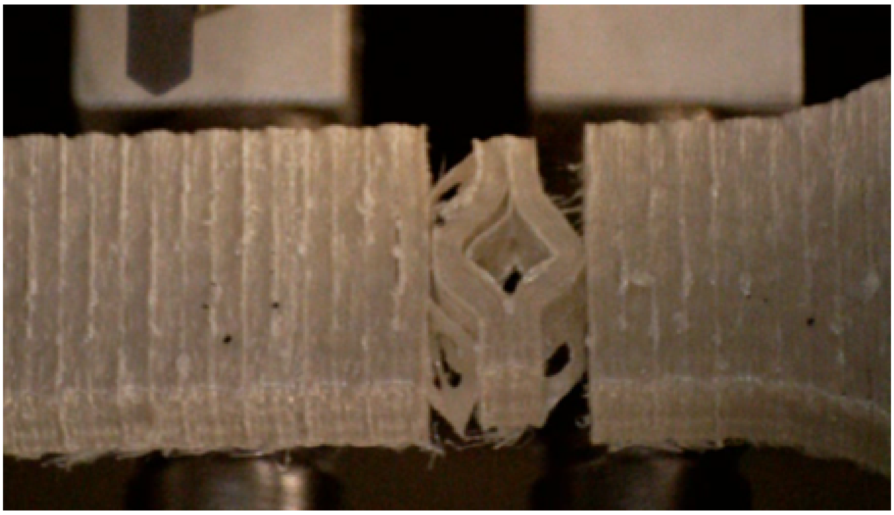

Figure D.18: Example of fracture in a D002 specimen (tall ABA) tested with the Zwick setup.

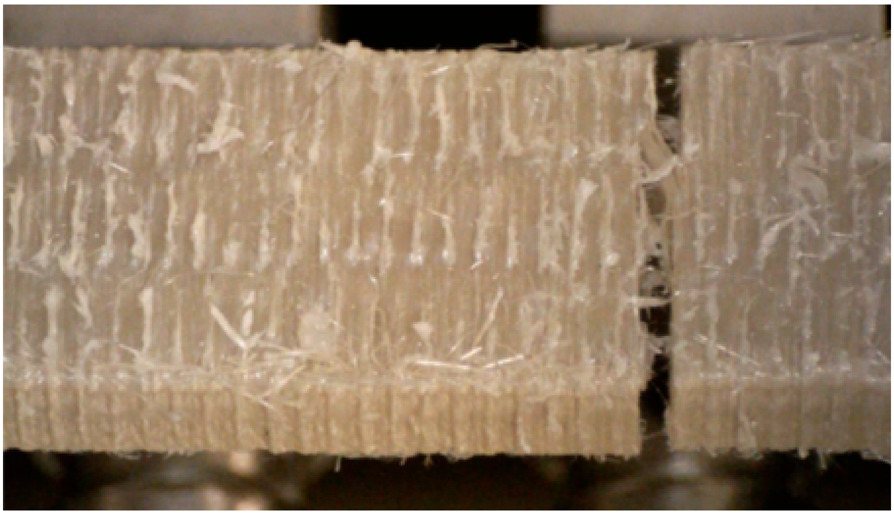

Figure D.19: Example of fracture in a D1 specimen (short ABC) tested with the Zwick setup.

Figure D.20: Example of fracture in a A specimen (medium ABC) tested with the Zwick setup.

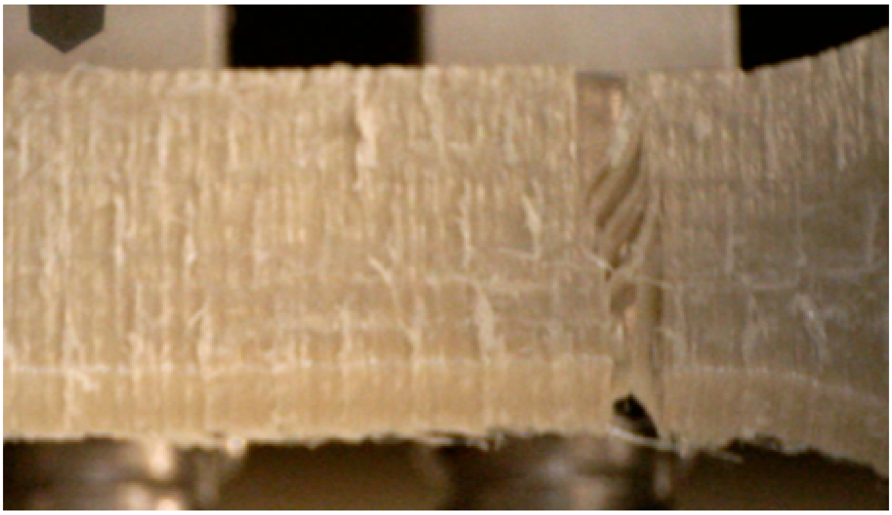

Figure D.21: Example of fracture in a D2 specimen (tall ABC) tested with the Zwick setup.

E

Further analysis of tensile testing procedures and result

This appendix expands on Section 5.2 by providing deeper insight into the testing conditions and setup variations that influenced the results presented in Appendix D. While the findings here support the interpretations discussed in the main chapter, they do not introduce new conclusions regarding the z-pinning methodology. The appendix is structured as follows: Section E.1 describes the different testing setups used; Section E.2 compares the resulting data across these setups; Section E.4 assesses the reliability of the selected reference configuration; Section E.3 addresses unexpected results in some pinned specimens; and Section E.5 evaluates supplementary work- and toughness-related metrics.

E.1. Test Setup Differences

Tensile testing for this study was conducted using two distinct test setups. Testing began with one configuration and was later completed with another due to evolving methodology and practical considerations. Each setup consisted of a universal testing machine, mechanical clamps, and a load cell. Because the load cells did not differ meaningfully in behavior or influence test results, they are not considered in this comparison.

The first setup used an Instron 5 kN Universal Test Machine, while the second employed a Zwick 20 kN Universal Test Machine. The loading rate applied was 0.05 mm/min. Though manufacturer and capacity were not critical to performance, they provide a convenient shorthand: the setups will be referred to as the "Instron" and "Zwick" test setups, respectively. The main distinctions between them were the clamp types, software interfaces, and specific post-processing procedures associated with the specimens.

Post-Processing Differences

Post-processing differences arose not from the machines themselves but from changes in research practices over time. In the initial phase (Instron setup), pinned specimens were not only cleaned to remove pin over-extrusion (as described in Subsection 5.1.4) but also sanded using 200-grit sandpaper to reduce surface roughness. This step was believed to limit crack initiation by minimizing stress concentrations between printed layers. In contrast, sanding was omitted in the final Zwick-based tests. The reasons were threefold: the increased number of specimens, a desire to avoid pre-test cracking, and an effort to better reflect industrial practices that minimize post-processing.

Clamping Mechanisms

Figure E.1 and Figure E.2 show the clamping mechanisms used in each setup. The Instron clamp was fully fixed and required an adapter (see Figure E.1b), while the Zwick clamp allowed the lower portion to rotate (see Figure E.2a). However, due to the specimen geometry, the Zwick configuration did not allow perfect alignment of the specimen's symmetry axis with the machine's loading axis (visible in Figure E.2b). The rationale for moving to a rotating clamp was to reduce torsional stresses and damage from imperfect clamping, both of which could exacerbate the cracking caused by surface roughness. The Zwick clamps had also been used successfully in prior research [36].

In retrospect, the rotation feature of the Zwick clamps may have made specimen mounting more difficult and less consistent. Audible cracking during clamping persisted despite the change. Nevertheless, the main benefit of using the Zwick configuration was its advanced software and testing workflow.

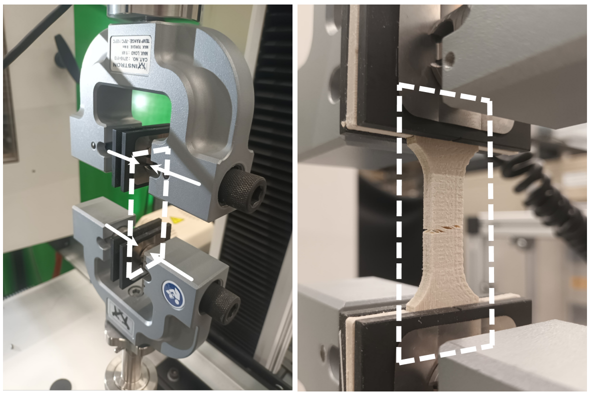

(a) Instron clamp jaws (b) Specimen placement

Figure E.1: Instron tensile test setup. (a) shows the rigid clamping jaws; (b) highlights the specimen placed using an adapter. The white dashed rectangle outlines the specimen area. Arrows indicate the clamping force direction.

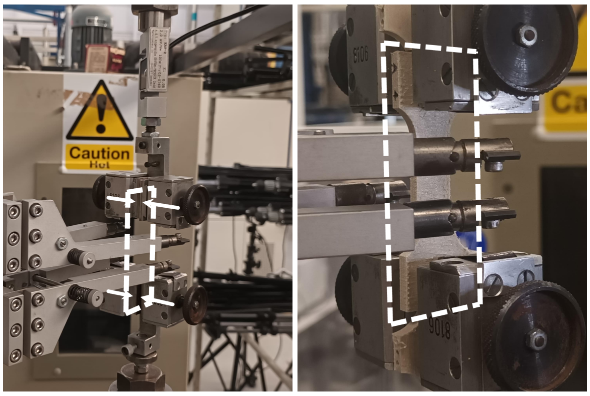

(a) Zwick clamp jaws (b) Specimen placement

Figure E.2: Zwick tensile test setup. (a) shows the rotating clamp assembly; (b) shows the specimen placed within the clamp. The dashed rectangle marks the specimen area. Arrows indicate the applied clamping force.

Software and Preload Control

A key motivation for adopting the Zwick system was its superior software handling. In the Instron setup, initial clamping often introduced significant preloads, sometimes reaching one-third of the specimen's failure load. These preloads were irreversible and introduced uncertainty in stress-strain analysis. The Zwick system enabled the controlled removal of preload before testing, thereby eliminating this ambiguity and allowing for more consistent test conditions. Moreover, the Zwick machine was equipped with an extensometer. Although it was intended for stiffness evaluation, hardware limitations prevented the extensometer from collecting effective data. Despite this, the consistency and clarity of the Zwick data ultimately justified its use in the primary analysis.

Confounding Factors

Beyond hardware and software differences, other confounding variables existed. The specimens tested in the two setups were printed using different filament spools and slightly adjusted slicer settings. As a result, it is difficult to isolate the source of variations observed between test rounds, as they may stem from hardware, clamping, filament batch, or processing changes.

E.2. Consistency of results across test setups

The shift from one testing setup to another, described in Section E.1, offered a unique opportunity to assess how sensitive the results are to differences in test setup, post-processing, and printing batch. Figure E.3 presents two comparative boxplots: Figure E.3a shows the maximum load of the reference specimens, while Figure E.3b shows the results for the medium ABC pin architecture. The agreement in $F_{\max}$ between the two testing setups enhances confidence in the validity and robustness of the findings.

However, two important caveats must be noted. First, the number of tested specimens is limited, especially for the Instron setup, reducing the statistical relevance of any conclusions drawn. Second, the reported data for the reference batch represent a subset of the printed specimens. Several samples were excluded due to failure during removal from the bed, post-processing, handling, or clamping. This introduces a survivorship bias favoring more robust specimens. Nonetheless, the close similarity in $F_{\max}$ distributions across setups provides reassurance.

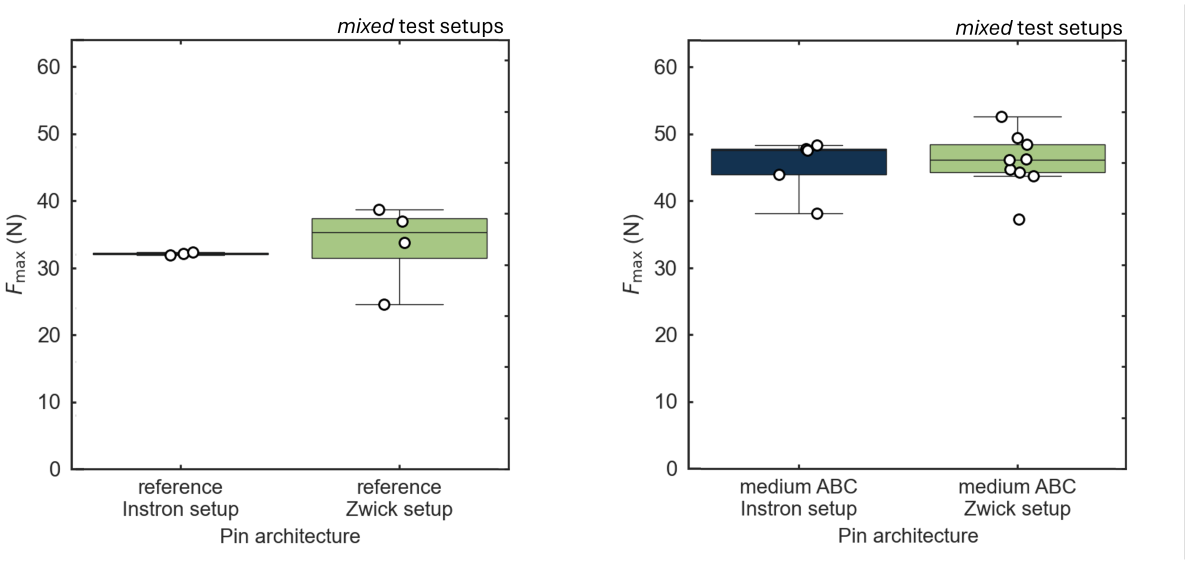

(a) Reference configuration

(b) Medium ABC configuration

Figure E.3: Comparison of maximum load results for (a) reference and (b) medium ABC specimens tested with the Instron and Zwick setups. Despite differing hardware and sample batches, the values align closely.

Closer inspection of the load-displacement curves in Figure E.4 reveals clear differences in fracture behavior between the two datasets. Figure E.4a shows curves from the Instron setup, while Figure E.4b presents data from the Zwick setup. The phases labeled 1 to 3 correspond to distinct stages of loading: (1) a pseudo-linear elastic regime, (2) the load increase leading to maximum force, and (3) the post-peak region following $F_{\max}$. The most notable difference occurs in phase 2: specimens tested on the Instron exhibit a smooth, monotonic increase in load up to failure, whereas those tested on the Zwick machine frequently show one or more local maxima prior to reaching peak load. These local peaks are indicative of crack initiation events that are arrested by the pins, bridging the crack and restoring load transfer capacity, as discussed in Subsection 5.2.3.

Differences also appear in phase 3: specimens tested on the Zwick setup exhibit partial strength recovery through repeated peaks, while the Instron-tested specimens tend to display a more rapid strength loss post-peak. These trends are consistent across all pin configurations. Figure E.5 compares selected curves from both setups and demonstrates that the fracture behavior is repeatable within all batches tested with the same test setup, regardless of pin architecture. The Zwick-tested specimens consistently exhibit pre-peak crack arrest, while the Instron specimens fail without intermediate load recoveries. Further analysis and discussion on the fracture mechanisms observed with the Zwick configuration continue in the following section.

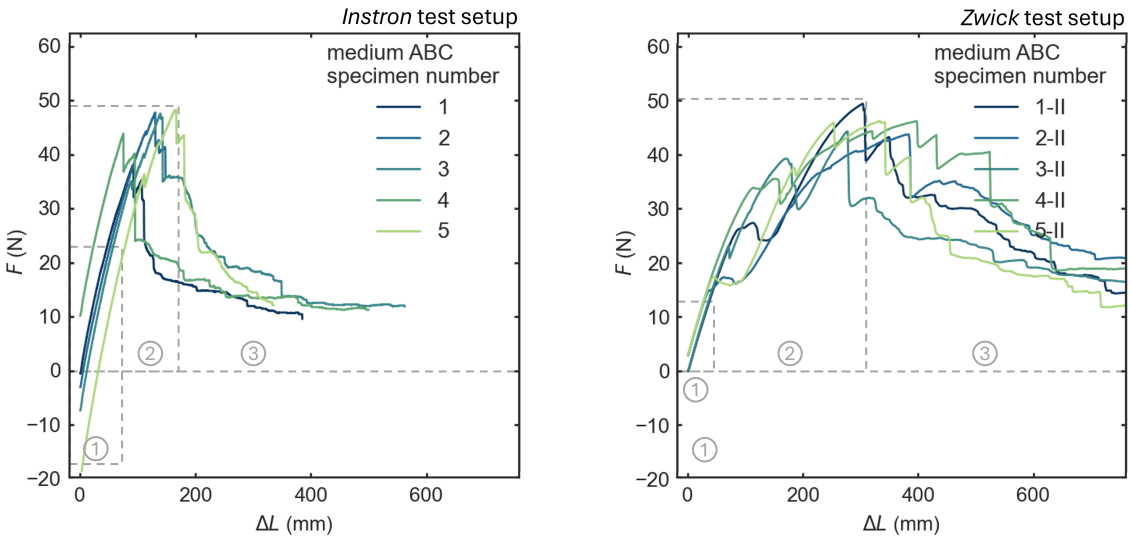

(a) Instron test setup (b) Zwick test setup

Figure E.4: Representative load-displacement curves for the medium ABC configuration tested with (a) Instron and (b) Zwick setups. Numbers 1–3 indicate distinct fracture phases: (1) pseudo-linear elastic, (2) pre-peak load increase, and (3) post-peak strength loss. Zwick data shows multiple pre-peak events attributed to crack arrest.

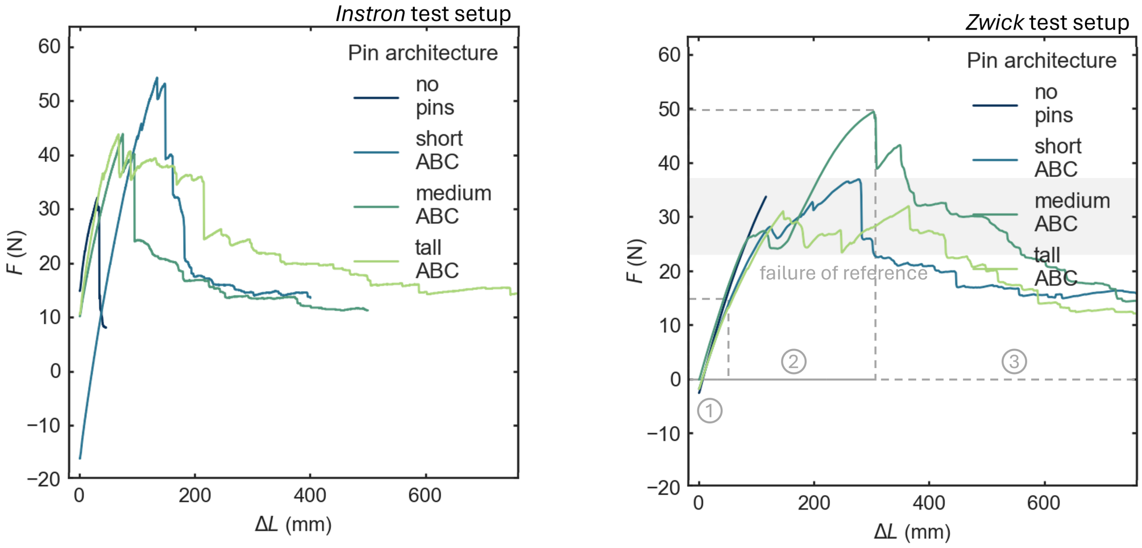

(a) Instron test setup (b) Zwick test setup

Figure E.5: Examples of load-displacement curves across all pin configurations and reference specimens. Each subplot contains specimens tested with the same setup. The Zwick curves (b) consistently show pre-peak cracking and load recovery, while Instron specimens (a) exhibit linear elastic failure without significant crack arrest. In (b), numbers 1–3 indicate distinct fracture phases: (1) pseudo-linear elastic, (2) pre-peak load increase, and (3) post-peak strength loss.

E.3. Unexpected mechanical performance of specific test batches

As introduced in Section E.2 and discussed further in Subsection 5.2.3, several specimens tested using the Zwick setup exhibited local maxima in their load-displacement curves, followed by strength recovery. Figure E.6 presents example load-displacement curves for each pin configuration, with reference specimens included to highlight the failure load interval. These examples show that the initial peak load corresponding to crack nucleation typically occurs within the same range as the failure loads of the reference specimens.

To quantify this behavior, Figure E.7 plots the crack initiation load F_{crack} for all pin configurations. Together, the two figures demonstrate that under the Zwick setup, cracks consistently initiate within the $F_{\max}$ range of unreinforced reference specimens. However, unlike the brittle, catastrophic propagation observed in reference specimens, the pinned specimens often arrest the crack and recover load-carrying capacity due to the presence of z-pins. This suggests that while the layer infill remains the primary crack initiation site, the pins effectively prevent propagation. Despite the benefit of crack arrest, the fact that pins do not avoid the initiation of cracks is suboptimal, especially when contrasted with the Instron tests, in which such early cracking completely largely absent. Since crack nucleation is often linked to surface imperfections, it is plausible that the lack of sanding in the Zwick batches (see Section E.1) led to consistent early cracking. This supports the notion that post-processing to reduce surface roughness could enable extended elastic behavior.

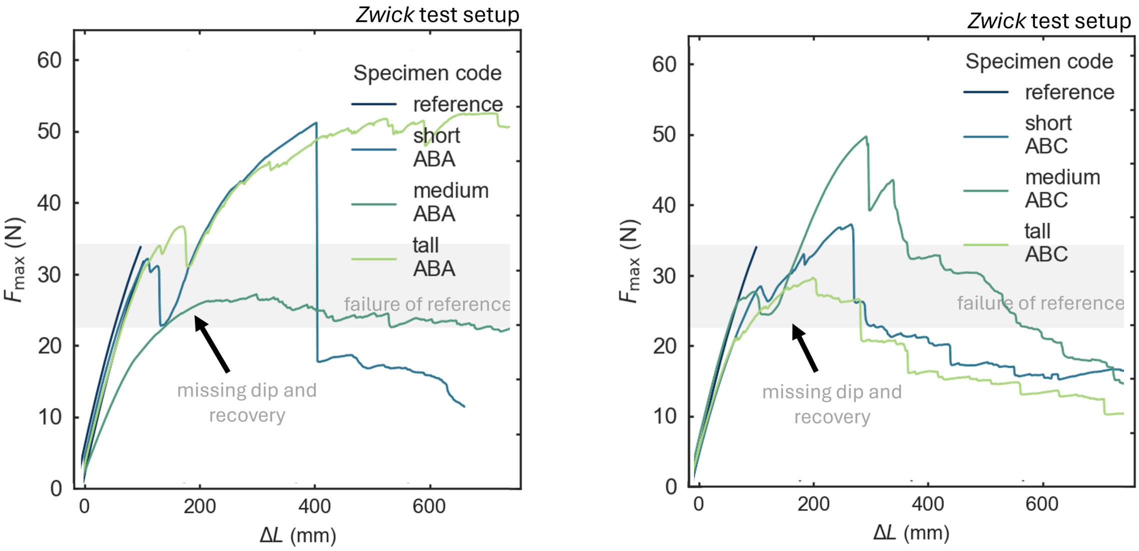

(a) ABA pin architectures

(b) ABC pin architectures

Figure E.6: Load-displacement curve examples for each tested pin architecture and the reference configuration. The highlighted intervals indicate the range of failure loads for reference specimens. Initial crack nucleation in pinned specimens consistently falls within this range, suggesting that pins do not prevent initiation, but rather limit crack growth.

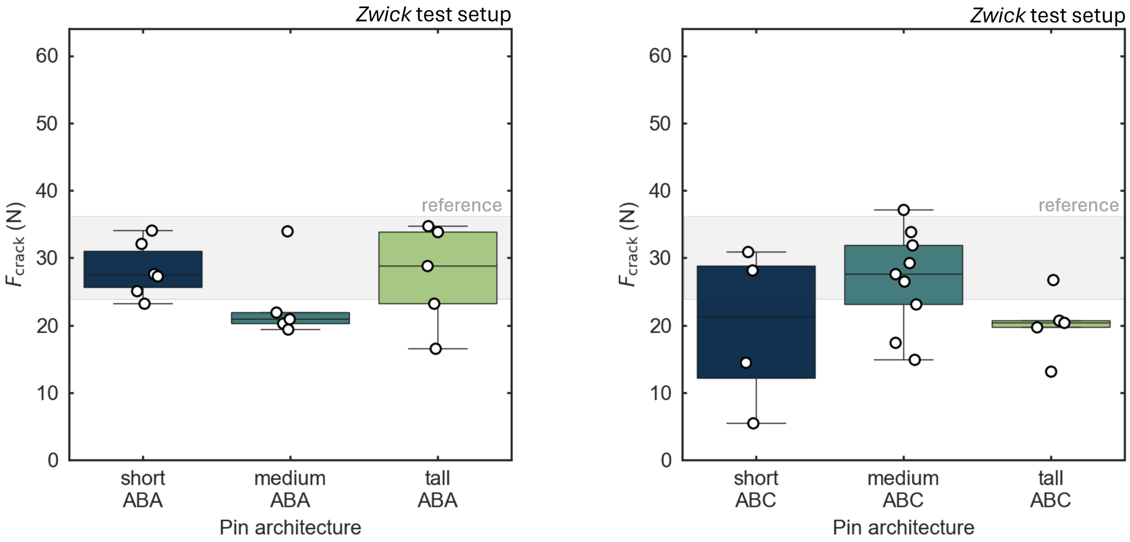

(a) ABA pin architectures

(b) ABC pin architectures

Figure E.7: Comparison of crack initiation loads F_{crack} for different pin geometries and staggering patterns. (a) reports the data for ABA architectures, (b) for ABC. The shaded region represents the failure interval of the reference specimens. Two configurations, medium ABA and tall ABC, exhibit premature cracking.

Two pin configurations stand out as outliers: medium ABA and tall ABC. These do not follow the trends seen in other configurations. As shown in Figure E.6, they do not exhibit evident strength recovery after the initial crack. Figure E.7 further shows that crack initiation in these batches occurs below the reference failure interval. Finally, as seen in Figure 5.10 (reproduced below), their maximum load falls within the range of the unreinforced specimens, showing no significant improvement. Taken together, these observations strongly suggest that pinning in these batches was defective; either the pins failed to bridge layers, or they did not bond effectively with the surrounding material. Consequently, these configurations are marked in the mechanical performance summary figures in Subsection 5.2.3 and Section E.5 with shaded regions in to indicate the expected performance range based on the results of other, successfully reinforced batches. Notably, although medium ABA and tall ABC specimens performed poorly in terms of peak strength, they still avoided brittle failure and absorbed more energy than reference specimens, suggesting partial benefit from the presence of pins, even if the bridging function was compromised.

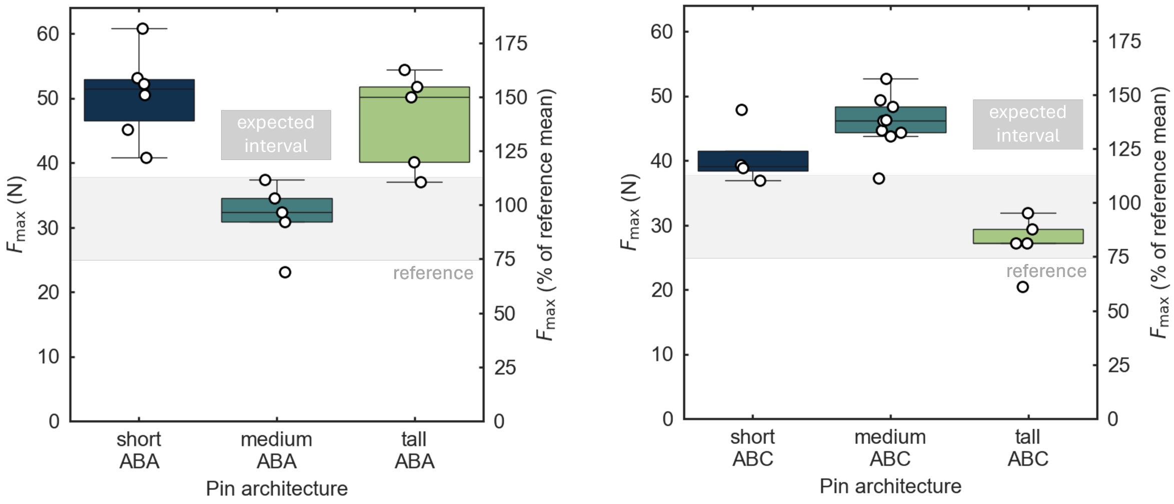

(a) ABA pin architectures

(b) ABC pin architectures

Figure 5.10 (reproduced): Maximum tensile load (F_{max}) for all pin configurations. The shaded gray band represents the failure range of the reference specimens. The medium ABA and tall ABC configurations fail to show improvement, confirming the compromised pin function.

E.4. Reference and unpinned void specimens test data

During the preliminary testing phase, tensile tests were attempted on specimens featuring pin cavities that were not filled with pin material. The aim was to isolate the mechanical impact of the cavities themselves, i.e., the geometric and deposition-related disruptions to the layer infill, separate from the contribution of the pins. However, this strategy was ultimately abandoned due to the extreme fragility of such specimens: the vast majority failed before testing could commence, often during post-processing or handling. The remarkable improvement in handling, although qualitative, itself underscores the significant improvement in mechanical integrity introduced by the pins. Notably, pinned specimens (in which pins comprise only 15% of the gauge volume for the medium pin configuration) showed no such pre-test failures. By contrast, unfilled-cavity and even reference specimens (without cavities or pins) frequently failed before testing.

A limited number of unpinned specimens did survive testing, and the corresponding data, albeit strongly biased by survivorship, is shown in Figure E.10a. Surprisingly, these void specimens exhibited slightly higher maximum loads than the reference specimens, despite having a reduced cross-sectional area (15% smaller on average, and down to 80% in certain staggered regions). This counterintuitive result must be treated cautiously due to the small sample size and biased selection. However, a consistent difference in fracture pattern was observed. As shown in Figure E.10b, void specimens exhibited limited post-peak load bridging, even though both groups failed in a brittle manner.

A closer inspection of the manufacturing process suggests reasons for this anomaly. First, the presence of cavities lengthens the print time per layer, which is known in literature and practice to reduce interlayer strength due to cooling effects. Second, the volumetric flow ratio (i.e., filament extruded per designed volume) was lower in the cavity-containing specimens, which would also typically reduce interlaminar bonding. Both of these reasons should lead to the opposite mechanical performance from the one recorded. However, the most consequential distinction in manufacturing between reference and unpinned void specimens may lie in the infill strategy. While reference specimens were printed with a concentric infill, specimens with cavities used a rectilinear pattern. More importantly, the presence of cavities disrupted the infill continuity, creating numerous travel moves and print path interruptions. These interruptions led to excess filament deposition and raised ridges around the cavity walls. Such ridges likely enhanced interlayer adhesion by increasing surface roughness and contact area, akin to the concept of “brick-layer" printing in FFF, which promotes mechanical interlocking across layers. This hypothesis is supported by visual inspection of the fracture surfaces, which appeared rougher in void specimens, and by the distinct fracture path observed in Figure E.10b. While not conclusive, these results suggest that the altered deposition dynamics caused by cavities alone may inadvertently enhance interlayer bonding in some cases, even in the absence of pins.

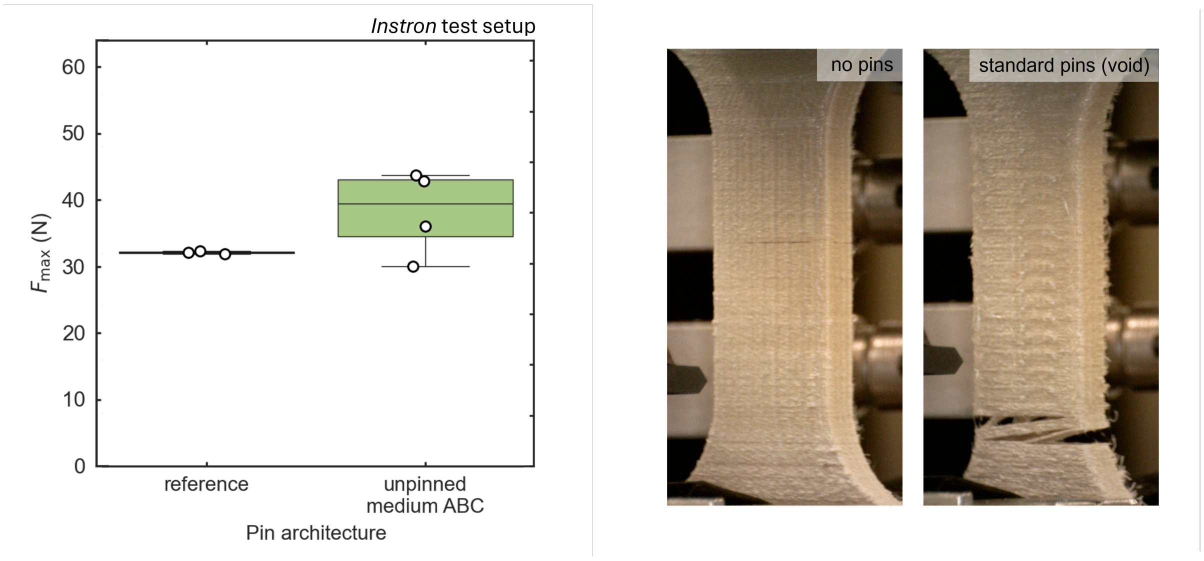

(a) Maximum load comparison

(b) Fracture surface morphology

Figure E.10: Survivor-biased comparison of maximum load performance between reference specimens and unpinned specimens featuring pin cavities, tested with the Instron setup. Subfigure (a) shows slightly higher peak loads for void specimens despite lower cross-sectional area, while (b) illustrates rougher fracture patterns, indicative of increased interlayer friction or mechanical interlocking.

E.5. Additional considerations on work-based metrics

As introduced in Subsection 5.2.3, work (W) was used as a metric to evaluate the damage tolerance provided by the pins. While the main focus in that section was on W before $F_{\max}$, this appendix complements the analysis by presenting two additional work-based metrics: work after $F_{\max}$ and total work. These are shown in Figure E.11 and Figure E.12, respectively, for the six pin configurations assessed in the parametric study. No new trends emerge from these graphs beyond those already observed in Subsection 5.2.3. However, they provide important confirmation: the W after $F_{\max}$ is consistently about an order of magnitude larger than W before $F_{\max}$ across all pin heights and staggering patterns. This reinforces the conclusion that pinned specimens retain substantial energy dissipation capacity even after surpassing their maximum load.

Due to the dominance of post-peak work, the total W values closely follow the same trends as W after $F_{\max}$, and are nearly identical in scale. Once again, the tall ABA configuration shows the highest performance, far exceeding that of the ABC layout. While the improvement in W before $F_{\max}$ for tall ABA was already approximately 10-fold relative to the reference, the total work absorbed is increased by nearly two orders of magnitude, demonstrating the profound impact of effective pinning on post-peak mechanical behavior.

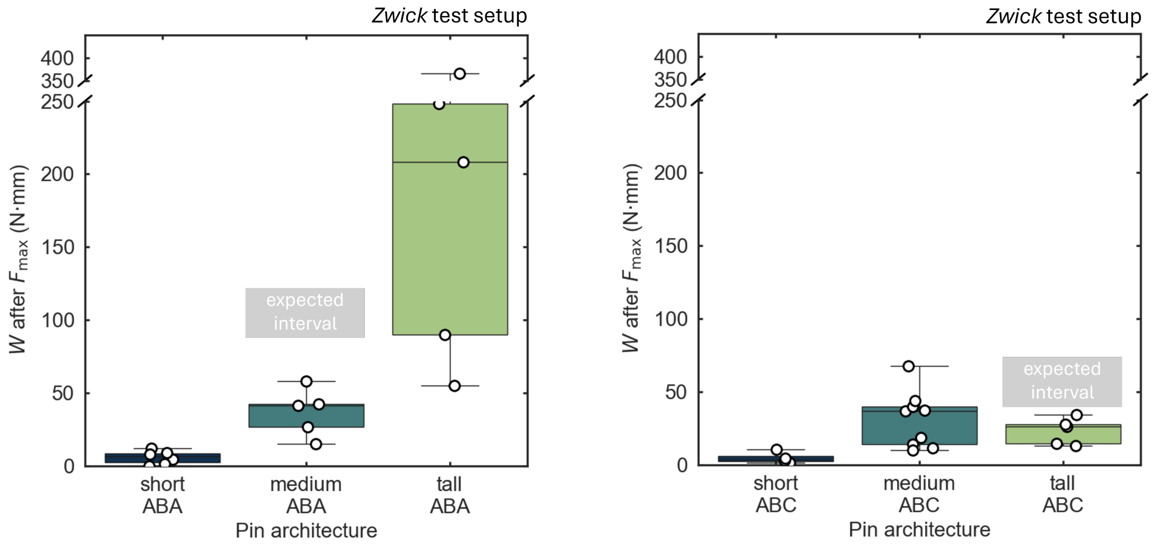

(a) ABA pin architectures

(b) ABC pin architectures

Figure E.11: Work absorbed after reaching F_{max} for different pin geometries and staggering orders. (a) shows results for ABA pin configurations. (b) shows results for ABC configurations. The shaded region indicates the performance range of unpinned reference specimens.

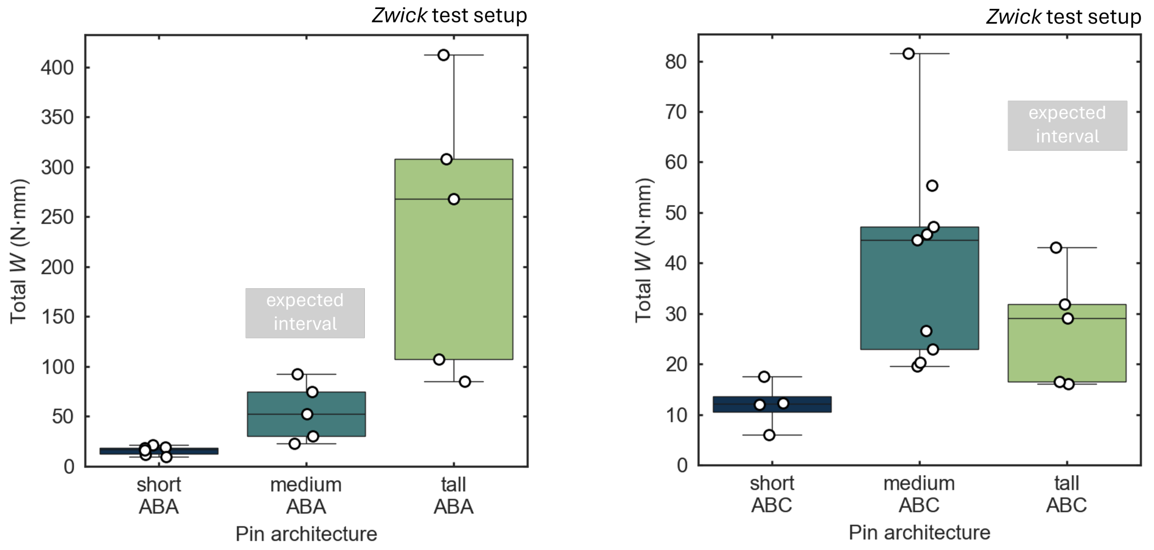

(a) ABA pin architectures

(b) ABC pin architectures

Figure E.12: Total work absorbed during tensile testing for different pin geometries and staggering orders. (a) presents results for ABA configurations. (b) presents results for ABC configurations. The shaded region indicates the performance range of unpinned reference specimens.